CONTROL OF SLURRY FLOW, TEMPERATURE AND AGGRESSIVE DIAMONDS IN CHEMICAL MECHANICAL PLANARIZATION

by

Changhong Wu

Copyright © Changhong Wu 2015

A Dissertation Submitted to the Faculty of the

DEPARTMENT OF CHEMICAL AND ENVIRONMENTAL ENGINEERING

In Partial Fulfillment of the Requirements

For the Degree of

DOCTOR OF PHILOSOPHY

WITH A MAJOR IN CHEMICAL ENGINEERING

In the Graduate College

THE UNIVERSITY OF ARIZONA

2015

UMI Number: 3701786

All rights reserved

INFORMATION TO ALL USERS
The quality of this reproduction is dependent upon the quality of the copy submitted.

In the unlikely event that the author did not send a complete manuscript
and there are missing pages, these will be noted. Also, if material had to be removed,
a note will indicate the deletion.

UMI 3701786

Published by ProQuest LLC (2015). Copyright in the Dissertation held by the Au

Microform Edition © ProQuest LLC.
All rights reserved. This work is protected against
unauthorized copying under Title 17, United States Code

ProQuest LLC.
789 East Eisenhower
Parkway
P.O. Box 1346

THE UNIVERSITY OF ARIZONA
GRADUATE COLLEGE

As members of the Dissertation Committee, we certify that we have read the dissertation prepared by Changhong Wu, titled Control of Slurry Flow, Temperature and Aggressive Diamonds in Chemical Mechanical Planarization and recommend that it be accepted as fulfilling the dissertation requirement for the Degree of Doctor of Philosophy.

____ Date: (April 14th, 2015)
Ara Philipossian

____ Date: (April 14th, 2015)
Farhang Shadman

____ Date: (April 14th, 2015)
Kimberly Ogden

____ Date: (April 14th, 2015)
Supapan Seraphin

Final approval and acceptance of this dissertation is contingent upon the candidate's submission of the final copies of the dissertation to the Graduate College.

I hereby certify that I have read this dissertation prepared under my direction and recommend that it be accepted as fulfilling the dissertation requirement.

____ Date: (April 14th, 2015)
Dissertation Director: Ara Philipossian

STATEMENT BY AUTHOR

This dissertation has been submitted in partial fulfillment of the requirements for an advanced degree at the University of Arizona and is deposited in the University Library to be made available to borrowers under rules of the Library.

Brief quotations from this dissertation are allowable without special permission, provided that an accurate acknowledgement of the source is made. Requests for permission for extended quotation from or reproduction of this manuscript in whole or in part may be granted by the copyright holder.

SIGNED: Changhong Wu

ACKNOWLEDGMENTS

First of all, I would like to give my deepest gratitude to my advisor, Prof. Ara Philipossian, for his great mentorship throughout my Ph. D. degree study. His continuous support, challenges and the opportunities that he has provided me have become invaluable experiences. I would like to especially thank him for his patience and encouragement in the first two years of my Ph. D. study when I had to overcome language and cultural barriers. I am really proud of having him as my advisor!

My gratitude also extends to my dissertation committee members Prof. Farhang Shadman, Prof. Kimberly Ogden and Prof. Supapan Seraphin for their continuous guidance and support. I also wish to express my appreciation to Dr. Len Borucki of Araca Incorporated for his excellent mentorship. His expertise was crucial for the completion of this dissertation. Many thanks go to Prof. Eduardo Saez, Prof. Roberto Guzman, Prof. Paul Blowers, Prof. James Farrell, Prof. Anthony Muscat, Prof. James Field and Prof. Srini Raghavan for their excellent teaching. Thanks also go to all of the department staff members including Arla Allen, Debra Romero, Alicia Foley and Karen McClure for their kind assistance.

I would like to thank my past and present team members Yun Zhuang, Yasa Adi Sampurno, Sian Theng, Xiaomin Wei, Anand Meled, Yubo Jiao, Xiaoyan Liao, Yan Mu, Ruochen Han and Xiangyu Niu for very nice discussions, collaborations and friendship.

I also would like to give special thanks to SRC/SEMATECH Engineering Research Center for Environmental Benign Semiconductor Manufacturing for their partial financial support.

I want to thank my leaders and mentors during my internship at Cabot Microelectronics Corporation. Thanks go to Drs. Ananth Naman, Jay Nair, Fred Sun and Jakub Nalaskowski. The knowledge that I gained there perfectly complemented my graduate studies. I also want to thank my manager Connie Truong, and Dr. Wei-tsu Tseng from IBM for giving me a full-time job. This provides me with a great opportunity to further explore the semiconductor field and apply what I have learned to the industry after I graduate.

Thanks go to my friends and classmates Hanh Duong, Binh Duong, Zhen Wang, Chieh-Chun Chiang, Bing Wu, Long Chen, Xinhai Xu, Hua Jiang, Binod Chaudhary, Alberto Cuevas, Pablo Mancheno and others for their kindness and friendship.

The immeasurable thanks go to my father, Yuli Wu, and my mother Youlan Tan, for their greatest sacrifice and the most unconditional love. They set an example of being great parents. Thanks also go to my wonderful sisters, brothers and parents-in-law for their support and understanding.

Finally, I would like to express my deepest love and thanks to Xiaoyan Liao, my beloved wife, for her endless love and support. She always demonstrates a positive attitude towards life and backs me up whenever I need help. Also, thanks for her unconditional sacrifice to our family. She is definitely a great wife and mother. I love you! My love and thanks also extend to my two lovely daughters, Sophia and Isabella. Thank

you very much for bringing me so many happiest moments. You help me realize that my life does matter. I love you!

Dedicated to Xiaoyan, Sophia and Isabella

TABLE OF CONTENTS

LIST OF FIGURES …… 12

LIST OF TABLES …… 18

NOMENCLATURE …… 19

ABSTRACT …… 21

CHAPTER 1 INTRODUCTION …… 24

1.1 Integrated Circuit Technology …… 24

1.2 Why CMP? …… 28

1.3 Applications of CMP in IC Manufacturing …… 31

1.3.1 ILD CMP …… 33

1.3.2 STI CMP …… 35

1.3.3 Cu CMP …… 35

1.3.4 W CMP …… 36

1.4 Consumables in CMP …… 37

1.4.1 Polishing Pad …… 37

1.4.2 CMP Slurry …… 43

1.4.3 Pad Conditioner …… 46

1.5 Challenges in CMP …… 50

1.5.1 CMP Film Thickness Control …… 51

1.5.2 Surface Defect Reduction …… 53

1.5.3 CoO and Environmental Considerations …… 54

1.6 Research Motivation and Goals …… 56

TABLE OF CONTENTS – Continued

CHAPTER 2 EXPERIMENTAL APPARATI ……………………………..… 59

2.1 The Araca APD-800 Polisher and Tribometer ……………………..… 59

2.1.1 Switches and Control Panels ………………………………… 61

2.1.2 Wafer Carrier System ……………………………………..…. 65

2.1.3 Polishing Platen System …………………….……….……. 69

2.1.4 Pad Conditioning System ……………………………..…... 69

2.1.5 Slurry/DI Water Distribution ……………………………..…. 71

2.1.6 Pad Surface Temperature Measurement System …..………. 71

2.1.7 Force Measurement System …………………………………. 72

2.1.8 Data Acquisition Program …………………………………... 74

2.1.9 Data Analysis Program …………………………….………… 76

2.1.10 Tool Specifications ……………………….……..………... 78

2.2 Analytical Tools …………………………………..…………..… 79

2.2.1 Four-point Probe …………………………………………….. 79

2.2.2 Reflectometer …………………………………………….….. 80

2.2.3 IR Camera ……………………………………….………… 81

CHAPTER 3 GENERAL THEORY …………………………………..……… 84

3.1 Tribology in CMP ………………………………………………… 84

3.1.1 Friction …………………………………………………….. 84

3.1.2 Lubrication Mechanism in CMP ………………..………… 89

3.1.3 Wear in CMP ………………………………………………… 93

TABLE OF CONTENTS – Continued

3.2 Material Removal Mechanisms in CMP …………………..………… 95

3.3 Various Removal Rate Models in CMP …………………………..… 96

3.3.1 Preston's Equation …………………………………………… 96

3.3.2 Modifications of Preston's Equation ………………………… 97

3.3.3 Langmuir-Hinselwood Removal Rate Model …………….... 98

CHAPTER 4 PAD SURFACE THERMAL MANAGEMENT DURING CHEMICAL MECHANICAL PLANARIZATION …………………………… 103

4.1 Introduction …………………….……………………………… 103

4.2 The PTM System ……………………………………………….…. 105

4.3 Experimental ……………………………………………………… 108

4.4 Results and Discussion ……………………………………………… 109

4.5 Conclusions ……………………………………………………….. 122

CHAPTER 5 EFFECT OF PAD GROOVE DESIGN ON SLURRY INJECTION SCHEME DURING INTERLAYER DIELECTRIC CHEMICAL MECHANICAL PLANARIZATION …………………………….. 124

5.1 Introduction……………………………………………………….. 125

5.2 The Slurry Injector ……………………………………..….….…. 128

5.3 Experimental ……………………………………………………… 129

5.4 Results and Discussion ……………………………………………… 131

5.5 Conclusions ……………………………………………………… 138

TABLE OF CONTENTS – Continued

CHAPTER 6 AGGRESSIVE DIAMOND CHARACTERIZATION AND WEAR ANALYSIS DURING CHEMICAL MECHANICAL PLANARIZATION …………………….……………………………………….....….. 140

6.1 Introduction ……………………………………………………….. 140

6.2 Experimental ………………………………………………………. 142

6.3 Results and Discussion ….…………………………………………… 146

6.4 Conclusions ……………………………………………………….. 157

CHAPTER 7 CONCLUSIONS AND FUTURE PLANS ………….…………… 159

7.1 Conclusions …………………………..……………………….. 159

7.2 Future Plans ……………………..……………………………….. 163

REFERENCES …………………………………………………….…………….. 166

LIST OF FIGURES

Figure 1.1: Trend of MPU printed gate length ..…………………………….. 25

Figure 1.2: Trend of the maximum number wiring levels for an IC……….... 27

Figure 1.3: Schematic of an IC cross-section ………..………………….….. 28

Figure 1.4: Schematic of multilevel interconnects fabricated without (left) and with (right) planarization ………..……………………….………… 30

Figure 1.5: Generalized schematic of a rotary CMP tool …………….……... 32

Figure 1.6: Various film stacks polished using CMP in CMOS technology ... 33

Figure 1.7: Schematic of ILD (left) and STI formation processes (right) ….. 34

Figure 1.8: Schematic of Cu-damascene (left) and W-plug (right) formation processes ………..……………………………………………….. 36

Figure 1.9: Top view of pads with (a) xy, (b) concentric, (c) floral, and (d) logarithmic spiral grooves …………………………………………….…..... 39

Figure 1.10: Pad micrographs of (a) Suba™, (b) Politex™, and (c) IC1000™ (DOW; JSR) ……………………………………………………….…..... 42

Figure 1.11: TEM images of (a) fumed silica and (b) colloidal silica………… 46

Figure 1.12: SEM image of a top view of a diamond disk ………………….…... 48

Figure 1.13: SEM images of Freudenberg FX-9 pad conditioned by various sizes of diamond: (a) new pad, (b) 60-grit, (c) 100-grit and (d) 200-grit .. 49

Figure 1.14: SEM images of an aggressive diamond (a) before and (b) after the 24-hour wear test ……………………………………………………….…. 50

LIST OF FIGURES - Continued

Figure 1.15: Example removal rate profile ……………………………….……... 52

Figure 1.16: Various types of surface defects …………………………….…….. 54

Figure 1.17: Factors contributing to the total CoO of the CMP module ……... 55

Figure 2.1: The Araca APD-800 polisher and tribometer …………………… 60

Figure 2.2: The primary ON/OFF switch of the APD-800 ………………..… 62

Figure 2.3: Manual switches on the front side of the APD -800 …………..… 62

Figure 2.4: The front panel of the APD-800 …………………………..…..… 63

Figure 2.5: An example of polishing sequence defined by the control panel 65

Figure 2.6: Wafer carrier system of the APD-800 …………………………… 66

Figure 2.7: Ceramic template of the carrier head ……………………….…… 66

Figure 2.8: The front side (a) and (b) back side of the wafer template with backing film for 300 mm wafer polishing ……………………… 67

Figure 2.9: The wafer template (with wafer) attached to the ceramic template 68

Figure 2.10: The back side of the wafer template for 450 mm wafer polishing 68

Figure 2.11: The polishing platen system of the APD-800 …………………… 69

Figure 2.12: The pad conditioning system of the APD-800…………………… 70

Figure 2.13: Pressure chamber of the pad conditioning system ……………… 71

Figure 2.14: Three slurry/DI water tanks of the APD-800………………….… 71

Figure 2.15: Slurry/DI water delivery tubes and the infrared gun ……………… 72

Figure 2.16: Shear force measurement system of the APD-800………………. 73

Figure 2.17: Example of shear force and down force measured during polishing 74

LIST OF FIGURES - Continued

Figure 2.18: Data acquisition program: conditioning down force sub-program 75

Figure 2.19: Data acquisition program: polishing measurements sub-program 76

Figure 2.20: COF data analysis ……………………………………...……..… 77

Figure 2.21: Temperature data analysis ……………………………….……… 77

Figure 2.22: AIT CMT-SR5000 sheet resistance/resistivity measurement system 80

Figure 2.23: SENTECH FTP reflectometer …………………………….…….. 81

Figure 2.24: The IR camera positioned to the polishing pad ……….……….. 82

Figure 2.25: An example of the thermal image …………………...………… 83

Figure 2.26: Pad surface temperatures as a function of polishing time ……… 83

Figure 3.1: Schematic of three-body contact in CMP ……………………..… 85

Figure 3.2: The Transient shear force and down force as a function of polishing time …………………………………………………………………..… 86

Figure 3.3: Transient COF based on Figure 3.2 ……………………………… 86

Figure 3.4: Correlation between Preston's constant and average coefficient of friction for different types of pads……………………….…………………..… 87

Figure 3.5: Correlation between the oxide removal rate and COF under different pad conditioning methods …………………...………...……….… 88

Figure 3.6: Calculation for α and the actual pressure ……………………… 90

Figure 3.7: Generic Stribeck curve based on Sommerfeld number ………… 92

Figure 3.8: Prestonian removal rate model for ILD CMP…………………… 97

LIST OF FIGURES - Continued

Figure 3.9: Arrhenius relationship between the copper removal rate and mean pad surface temperature …………………………………...…………… 101

Figure 3.10: Arrhenius relationship between the oxide removal rate and mean pad surface temperature …………………………………...…………… 102

Figure 4.1: Schematic of the top view of a polisher with the PTM system. Both pad and wafer are rotating in a counter-clockwise fashion ………..…. 106

Figure 4.2: Schematic of the thermal transfer module and water circulation 107

Figure 4.3: Removal rate profile comparison with and without the single thermal transfer module …………………………………………..…… 109

Figure 4.4: Position of the single thermal transfer module on the pad surface. Both pad and wafer are rotating in a counter-clockwise fashion. ..….. 110

Figure 4.5: Thermal image of the pad surface (a) and locations of "SP01" through "SP04" (b) using the single thermal transfer module. Both pad and wafer are rotating in a counter-clockwise fashion. …………………..…… 113

Figure 4.6: Pad surface temperature comparison with (a) and without (b) the PTM system (with the single thermal transfer module)………………… 114

Figure 4.7: Schematic of wafer rotation at (a) t = t1, (b) t = t2 and (c) t = t3 with the single thermal transfer module. Both pad and wafer are rotating in a counter-clockwise fashion ……………………..……..………… 117

Figure 4.8: Dwell time analysis with the single thermal transfer module …… 118

LIST OF FIGURES - Continued

Figure 4.9: Positions of the two thermal transfer modules on the pad surface. Both pad and wafer are rotating in a counter-clockwise fashion ………..… 118

Figure 4.10: Thermal image of the pad surface with the two thermal transfer modules. Both pad and wafer are rotating in a counter-clockwise fashion … 119

Figure 4.11: Pad surface temperature with the two thermal transfer modules 120

Figure 4.12: Dwell time analysis with the two thermal transfer modules …….. 121

Figure 4.13: Removal rate profile comparison with and without the two thermal transfer modules………………………………...……..…….…. 122

Figure 5.1: Top view of a polisher with the (a) standard slurry application method and (b) novel slurry injection system. Both pad and wafer are rotating in a counter-clockwise fashion.…………………………........……… 126

Figure 5.2: Schematic of (a) the novel slurry injector and (b) its “body” bottom 129

Figure 5.3: Removal rate comparison between the one injection point scheme and standard slurry application method on the concentrically grooved pad 132

Figure 5.4: An example slurry distribution image with SIS collected via UVIZ-100 system ………………………………………………………… 132

Figure 5.5: Removal rate comparison between the one injection point scheme and the standard slurry application method on the xy-groove pad ……… 134

Figure 5.6: Schematic of slurry flow patterns on the (a) concentrically grooved pad and (b) xy-groove pad ....…..… 136

LIST OF FIGURES - Continued

Figure 5.7: Removal rate comparison among different slurry injection schemes on the xy-groove pad …………………........………………………...… 137

Figure 6.1: Experimental setup for disk dragging test ……….…………….…… 144

Figure 6.2: Profile scan of the surface of the polycarbonate sheet ………...… 144

Figure 6.3: Photograph of (a) the XL10 polycarbonate sheet and (b) chromium deposited IC1000 pad with scratches marked …............………..… 146

Figure 6.4: Changes in the furrow surface area for the original top 20 aggressive diamonds …..…...…. 147

Figure 6.5: SEM images of an original aggressive diamond (a) before and (b) after 30-hour wafer polishing …...…....… 148

Figure 6.6: Changes in the furrow surface area percentage for the original top 20 aggressive diamonds …...…....… 149

Figure 6.7: Changes in the furrow surface area for the new top 20 aggressive diamonds identified after the first 15-hour wafer polishing…...........…....… 151

Figure 6.8: Changes in the surface area percentage for the newly identified top 20 aggressive diamonds after the first 15-hour wafer polishing…....... 152

Figure 6.9: SEM image of a new “born” aggressive diamond after 30-hour wafer polishing ….. 153

Figure 6.10: Changes in the total furrow subsurface area during 30-hour wafer polishing ….. 154

Figure 6.11: SEM image of a typical aggressive diamond …............................... 157

LIST OF TABLES

Table 2.1: Parts of the APD-800 and their functions …………….………… 61

Table 2.2: Manual switches and their functions ……….……………....…... 63

Table 2.3: Parts and functions of the APD-800 front panel ………………… 64

Table 2.4: The APD-800 component specifications ……………..……….…… 78

Table 6.1: Rank, furrow surface area and percentage for 7 new "born" aggressive diamonds after the first 15-hour polishing test …….……….….… 150

Table 6.2: Rank, furrow surface area and percentage for the newly "born" aggressive diamonds after the second 15-hour polishing test …….………… 153

Table 6.3: Number of common top 20 aggressive diamonds for Orientation 1 and 7 ……………………………………………………………….……… 156

NOMENCLATURE

A	= Exponential factor
A_{flat}	= Total area including the land area and the bottom area of the groove
$A_{land-area}$	= Land area of the pad surface
a	= A dimensionless parameter used to scale the wafer pressure
β	= Fitting parameter
C	= Local molar concentration of the reactant
CD	= Critical dimension
COF	= Coefficient of friction
COF_i	= Coefficient of friction at time i
$\overline{COF}$	= Average coefficient of friction
c_p	= Empirical proportionality constant
DOF	= Depth of focus
$Down\ Force_i$	= Down force at time i
d	= Thickness of the interconnect
E	= Slurry activation energy
e	= Fitting parameter
I	= Current
k	= Preston's constant
k_1	= Chemical rate constant
k_2	= Mechanical rate constant
k_b	= Boltzmann constant
k_e	= Extinction coefficient
L	= Abraded material
$\underline{L}$	= Product layer
l	= Length of the interconnect
NA	= Numerical aperture
n	= Number of moles
n_r	= Refractive index
p	= Polishing pressure
R	= Reactant
RC	= Resistance and capacity
RR	= Removal rate
$Ra_{pad\ surface}$	= Pad surface roughness
R_S	= Sheet Resistance
S	= Wafer surface film
$Shear\ Force_i$	= Shear force at time i
S_O	= Sommerfeld number
T	= Wafer surface reaction temperature
T_p	= Mean leading edge pad surface temperature
t	= Film thickness
t_d	= Thickness of the insulator

NOMENCLATURE- Continued

U	= Relative pad-wafer velocity
V	= Voltage
V	= Pad-wafer sliding velocity
M_w	= Molecular weight
ε	= Dielectric constant
λ	= Exposure wavelength
δ_{eff}	= Effective slurry film thickness at the pad-wafer interface
δ_{groove}	= Groove or perforation depth
μ	= Viscosity of the lubricant
μ_k	= Coefficient of friction
ρ	= Density

ABSTRACT

This dissertation presents a series of studies related to the study and control of slurry flow, process temperature, and aggressive diamonds in Chemical Mechanical Planarization (CMP). The purpose of these studies is to better understand the fundamentals of CMP and to explore solutions to some of CMP's greatest challenges.

Within-wafer removal rate non-uniformity (WIWRRNU) is a critical parameter to determine film thickness planarity on a wafer-scale level and it grossly impacts yield. Resolving this issue continues to be an area of intense focus in the industry. The first study in this dissertation shows the feasibility of adopting a new method to improve WIWRRNU during copper CMP that is solely based on intentional local temperature manipulation of the pad. A pad surface thermal management system is developed to locally change pad surface temperature. This system consists of one or more thermal transfer modules contacting the pad surface. In this study, the system is employed to adjust the "center-fast" copper removal rate profile to illustrate its effect during the process. Results shows that, when two thermal transfer modules are employed, local removal rates in the wafer center region decrease significantly while maintaining the removal rates near the wafer edge thereby significantly improving WIWRRNU.

Another contribution of this dissertation is the investigation of the effect of pad groove design on slurry injection scheme during interlayer dielectric CMP. A novel slurry injector with multiple slurry outlets is designed, which provides optional slurry injection schemes (i.e. one injection point scheme and multi-injection point scheme).

These schemes are compared with the standard slurry application method on a concentrically grooved pad and an xy-groove pad, respectively. On the concentrically grooved pad, the one injection point scheme generates significantly higher oxide removal rates (ranging from 22 to 35 percent) compared to the standard slurry application method at different slurry flow rates. On the xy-groove pad, the one injection point scheme still results in higher removal rates (ranging from 3 to 9 percent), however, its removal rate enhancement is not as high as that of the concentrically grooved pad. In order to further improve slurry availability on the xy-groove pad, the multi-injection point scheme is tested. Results show that the multi-injection point scheme results in significantly higher removal rates (ranging from 17 to 20 percent) compared to the standard slurry application method. This work underscores the importance of optimum slurry injection schemes for accommodating particular groove designs.

The last contribution of this dissertation involves a study regarding aggressive diamond characterization and wear analysis during CMP. A 3M A3700 diamond disk is used to condition a Cabot Microelectronics Corporation (CMC) D100 pad for 30 hours. The top 20 aggressive diamonds for two perpendicular disk orientations are identified before the polishing, as well as after 15- and 30-hour polishing. The furrow surface area generated by these top 20 aggressive diamonds and their evolution are analyzed and compared. Results show that the original top 20 aggressive diamonds identified before polishing are subjected to wear after the first 15-hour polishing as the furrow surface area that they generate decreases dramatically (by 47%). As these original aggressive diamonds are worn, seven new aggressive diamonds are “born” and join the new top 20

list for both disk orientations. After the second 15-hour wafer polishing, the furrow surface area of these new top 20 aggressive diamonds do not change significantly. The furrow surface area created by all the active diamonds exhibits the same trend as the top 20 aggressive diamonds, confirming that most pad conditioning work is performed by these aggressive diamonds and that the disk loses its aggressiveness in the first 15 hours of polishing and then maintains its aggressiveness during the second 15 hours, albeit to a lesser extent.

CHAPTER 1

INTRODUCTION

The purpose of this dissertation is to better understand the fundamentals of the process known as Chemical Mechanical Planarization (CMP) and to explore solutions to the challenges posed by this process. This dissertation mainly focuses on the control of slurry flow, temperature, and aggressive diamonds to improve polishing performance while lowering the cost of ownership (CoO) and reducing the adverse environmental effects.

1.1 Integrated Circuit Technology

Essentially, integrated circuits (ICs, also referred to as *chips*) consist of a large number of components (transistors, resistors, capacitors, etc.), fabricated side by side on a common substrate and connected together to perform a particular circuit function (Plummer *et al.* 2000). Since John Bardeen, Walter Brattain and William Shockley of Bell Laboratories invented the transistors in the 1940s (Shockley 1984), IC technology has been growing nonstop. The circuit density and complexity keep on increasing. As predicted by Moore's Law, the number of transistors on a chip doubles every eighteen months to two years (Moore 1965). This trend has been maintained for almost half a century and is expected to continue in the foreseeable future. To date, the transistor count in a central processing unit (CPU) can reach several billions (Krishnaswamy *et al.* 2013).

The continuous increase in the transistor count on a chip can be attributed to the continuous shrinking of the minimum feature size. Figure 1.1 shows the microprocessor unit (MPU) printed gate length as a function of time from 2001 to 2028. The numbers from 2001 to 2013 are actual values while those from 2015 to 2028 are predicted ones by international technology roadmap for semiconductors (ITRS) 2013 (http://www.itrs.net/). As observed in Figure 1.1, the MPU printed gate length keeps on scaling down. Since the transistor count per unit area is determined by the surface area of a transistor, the density of the transistor increases quadratically with a linear decrease in feature size (Hennessy *et al.* 2007).

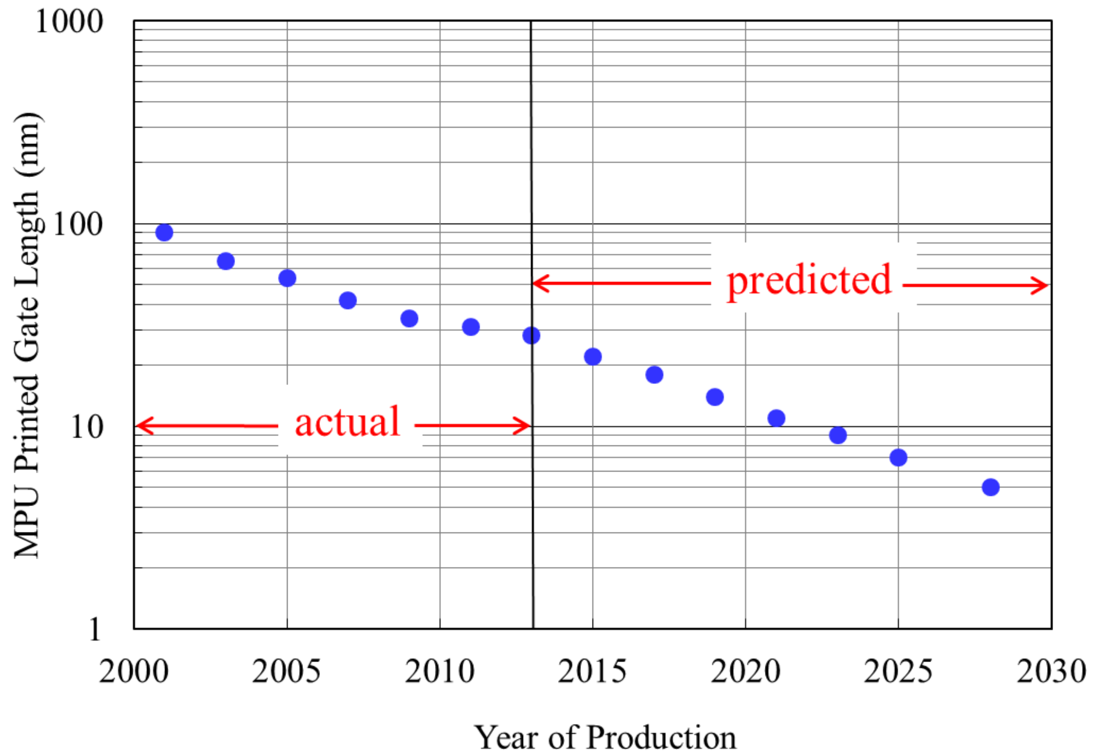

Figure 1.1: Trend of MPU printed gate length (ITRS 2013).

The decrease in minimum feature size increases the packing density and hence reduces the cost of function (Steigerwald *et al.* 1997; Kang *et al.* 2002). However, as the feature size reduces below 0.5 μm, the improvement of device performance such as speed is hindered by signal processing delay (McGuire 1988). Gate delay and interconnect delay are two major sources of signal processing delay, but the interconnect delay is dominant as the feature size scales down to below 0.5 μm (Nguyen *et al.* 1999). The interconnect delay (also referred to as *RC* delay) can be expressed as (Holloway *et al.* 1996):

$$RC = \rho \varepsilon l^2 / t_d d \qquad \text{Eq. 1.1}$$

where *R* is the resistance of the interconnect, *C* is the capacity of the dielectric, ρ is the resistivity of the interconnect, ε is the dielectric constant, *l* is the length of the interconnect, t_d and *d* is the thickness of the insulator and interconnect, respectively.

In order to reduce *RC* delay, one approach is to employ an interconnect material with a lower resistivity as indicated by Eq. 1.1. As we know, aluminum is the first generation of the interconnect material, which has a resistivity of 2.82 μΩ cm. Today, copper has been widely used as the interconnect material since it has a lower resistivity (1.68 μΩ cm) than aluminum. Another approach to reduce *RC* delay is to substitute the traditional silicon dioxide with low-k (i.e. low-ε) dielectric materials. In addition, it should be noted that *RC* delay is proportional to l^2 as indicated by Eq. 1.1. As such, an efficient interconnect system is critical to reducing *RC* delay. For example, a multilevel

interconnect scheme has been widely employed to offer more direct routing and therefore to reduce the length of connections among devices, leading to a significant reduction in signal processing delay (Li 2008). As chips become more and more complex, the number of wiring levels keeps on increasing. Figure 1.2 shows the maximum number wiring levels as a function of time from 2013 to 2028 (ITRS 2013). As evident in Figure 1.2, the maximum wiring layer is 13 now and it is predicted to be 17 in 2028.

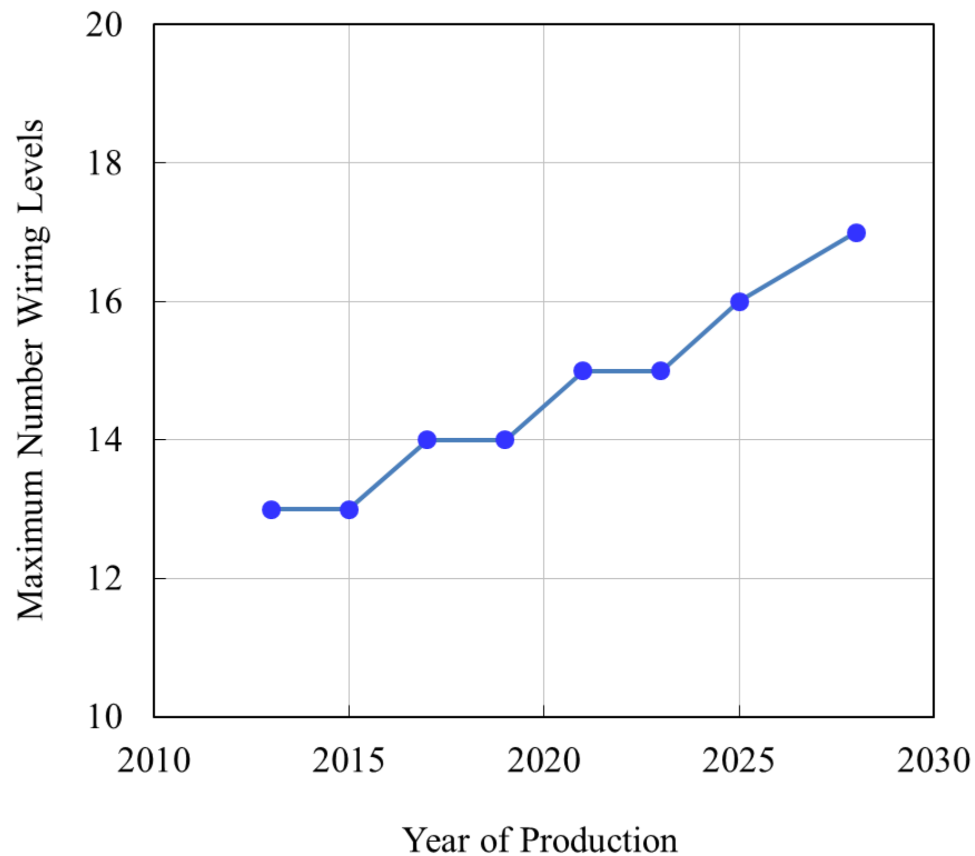

Figure 1.2: Trend of the maximum number wiring levels for an IC (ITRS 2013).

Figure 1.3 schematically shows a thin cross-section of an IC (left) and the details at the transistor level (right) (Liao 2014). As evident in Figure 1.3, there are 13 copper

layers. Basically, IC fabrication is a sequential layering process from the “bottom up” (Wolf 2004). Transistors are built at the bottom of the IC and act as ON/OFF switches. Transistor building is followed by the formation of the tungsten (W) plugs. The W plugs are built to connect the transistors and first Cu interconnects. After building the W plugs, the Cu interconnects and interlayer dielectrics are formed layer by layer. The Cu layers are connected by the vertical Cu vias. Transistors and all the above layers of metals and dielectrics are connected to create complex circuits (Wolf 2004).

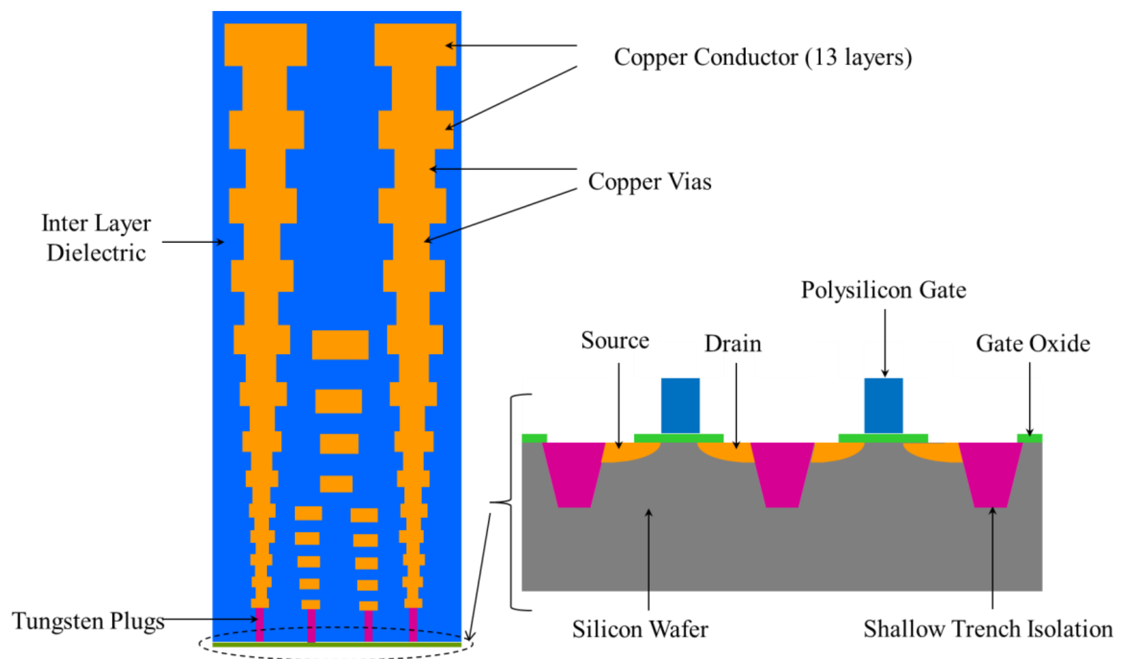

Figure 1.3: Schematic of an IC cross-section (figures are not drawn to scale) (Liao 2014).

1.2 Why CMP?

The patterns that define structures in ICs are created by photolithographic processes. A photolithographic tool must be able to focus on all points of interest in order

to image features accurately across the wafer. In other words, the surface topography or step height must be within the depth of focus. Or else, it may lead to a loss in yield. For example, if the depth of focus for a particular feature size is 500 nm, any step heights larger than 500 nm on the surface may cause improper patterning on the photoresist layer, resulting in the failure of the interconnect network (Li 2008).

As discussed in Section 1.1, one trend in IC technology is that the minimum feature size keeps on scaling down. This leads to the reduction in the depth of focus and hence creates challenges to surface planarization. Eq. 1.2 and Eq. 1.3 indicate the depth of focus is reduced as the minimum feature size scales down (May *et al.* 2004). Either reducing the exposure wavelength (λ) or enhancing the numerical aperture (NA) leads to decrease in minimum feature size or critical dimension (CD). However, both approaches to improve critical dimension reduce depth of focus (DOF). For a photolithographic process with low depth of focus, a minute surface topography or step height may lead to a loss in yield (Doering *et al.* 2000).

$$CD = k_1 \frac{\lambda}{NA} \quad \text{Eq. 1.2}$$

$$DOF = k_2 \frac{\lambda}{(NA)^2} \quad \text{Eq. 1.3}$$

where CD is the critical dimension, k_1 and k_2 are process-dependent factors, λ is the exposure wavelength, DOF is depth of focus, and NA is the numerical aperture.

Another trend in IC technology is that multilevel interconnect scheme has been commonly used. This also creates challenge to surface planarization since the rugged topography builds up as the number of wiring levels increases. Figure 1.4 has been widely used to illustrate the importance of surface planarization for the multilevel interconnect scheme (Wolters 2003; Li 2008; Jiao 2012; Liao 2014). The figure on the left represents a chip that is fabricated without planarization. Step height or surface topography builds up with increasing wiring levels, which may make the surface of the upper layers far from being optically flat. In comparison, the figure on the right represents a chip that is fabricated with planarization. The surface of each layer on the chip is optically flat.

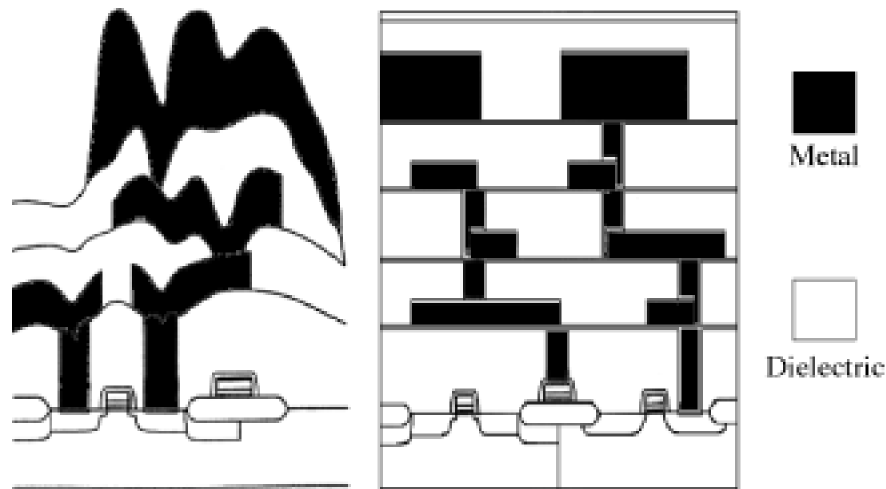

Figure 1.4: Schematic of multilevel interconnects fabricated without (left) and with (right) planarization (figures are not drawn to scale) (Wolters 2003).

To overcome the surface planarization challenge, up until now, several planarization techniques have been implemented. Traditional techniques include spin on

deposition (SOD), reflow of boron phosphorous silicate glass (BPSG), spin etch planarization (SEP), reactive ion etching and etch back (RIE + EB), spin on deposition and etch back (SOD + EB) (Gupta *et al.* 1989; Chang *et al.* 1985; Levert *et al.* 2001; Oliver 2004; Li 2008). However, when minimum feature sizes of ICs drop below 0.35 μm, or more than 3 metal layers are employed, all of the above techniques are inadequate to achieve planarity (Oliver 2004).

Driven with the planarization challenge in IC manufacturing for denser transistors and more wiring levels, CMP was invented by International Business Machines (IBM) in the mid-1980s (Moy *et al.* 1989). Presently, CMP is the only planarization technique that can offer excellent local and global planarity. Section 1.1 of this dissertation has shown that, for the most advanced ultra large scale integration (ULSI), the minimum feature size has scaled down to 20 nm and the maximum number of metal layers has now reached 13. In this case, CMP is the only choice for surface planarization and a true technology enabler.

1.3 Applications of CMP in IC Manufacturing

CMP simultaneously employs both chemical and mechanical actions to selectively remove the exposed material from elevated features, resulting in a surface with improved planarization (Steigerwald *et al.* 1997). Figure 1.5 illustrates a generalized CMP process on a rotary polisher. The wafer that is being polished is secured by a retaining ring and attached to the carrier head. The carrier head applies a certain pressure to the wafer against a polishing pad. During polishing, both wafer and pad rotate in

counter clockwise. Slurry containing chemicals and abrasive nanoparticles is injected onto the pad surface (Liao 2014). Platen-wafer rotation, pad grooves and retaining ring help transport the fresh slurry to the pad-wafer interface. Reactive chemicals in the slurry react with wafer surface to form a softer porous layer, which is then removed by mechanical forces through the actions of pad asperities and slurry abrasive nanoparticles. This two-step process is then repeated until the end of the CMP process. This mechanism is called Kaufman theory (Kaufman *et al.* 1991). Because of the mechanical abrasion, the rough pad surface may be flattened gradually. A pad conditioner is typically used to regenerate pad asperities.

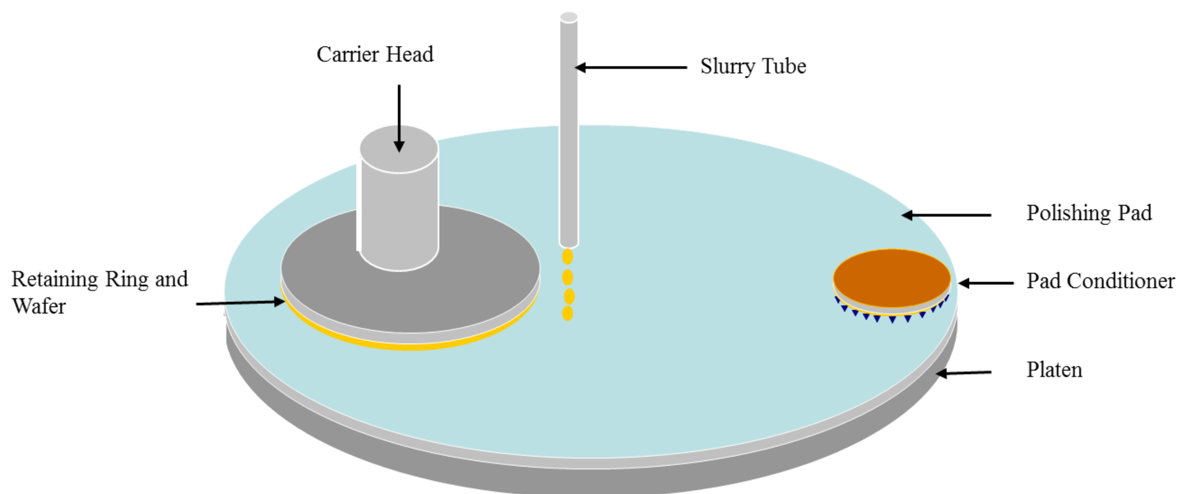

Figure 1.5: Generalized schematic of a rotary CMP tool (Liao 2014).

CMP has been widely used in IC processing to achieve local and global surface planarity. Figure 1.6 shows various film stacks polished using CMP in complementary metal-oxide-semiconductor (CMOS) technology. The first high volume processes were

oxide CMP for interlayer dielectric (ILD) CMP and tungsten CMP in 1995 (Banerjee *et al.* 2008). Since then, more and more materials have been polished using CMP. In general, CMP is primarily applied in four areas of IC fabrication: ILD, shallow trench isolation (STI), copper and tungsten damascene processes (Oliver 2004). The subsequent sections in this Chapter will briefly discuss these applications.

1995	2001	2005
Glass (Oxide)	Glass (Oxide)	Glass (Oxide)
Tungsten	Tungsten	Tungsten
	Copper	Copper
	Shallow Trench	Shallow Trench
	Polysilicon	Polysilicon
		Low k
		Cap Ultra Low k
		Metal Gates
		Gate Insulators
		High k Capacitors
		Ir & P Electrodes

Source: Cabot Microelectronics Corporation

Figure 1.6: Various film stacks polished using CMP in CMOS technology (Banerjee *et al.* 2008).

1.3.1 ILD CMP

ILD CMP aims to provide planarization between the increasing numbers of metal layers in the back end of line (BEOL). The image on the left of Figure 1.7 shows the ILD

formation process. Metal is deposited on the silicon dioxide layer to form interconnects. Interlayer dielectric is then deposited to insulate the interconnects. Since the dielectric material conforms to the topography of the underlying metal layer in the process of deposition, it produces a non-planar surface. CMP is then used for the planarization of this interlayer dielectric. In Chapter 5 of this dissertation, the effect of pad groove type on slurry injection scheme during ILD CMP will be investigated (Wu *et al.* 2015).

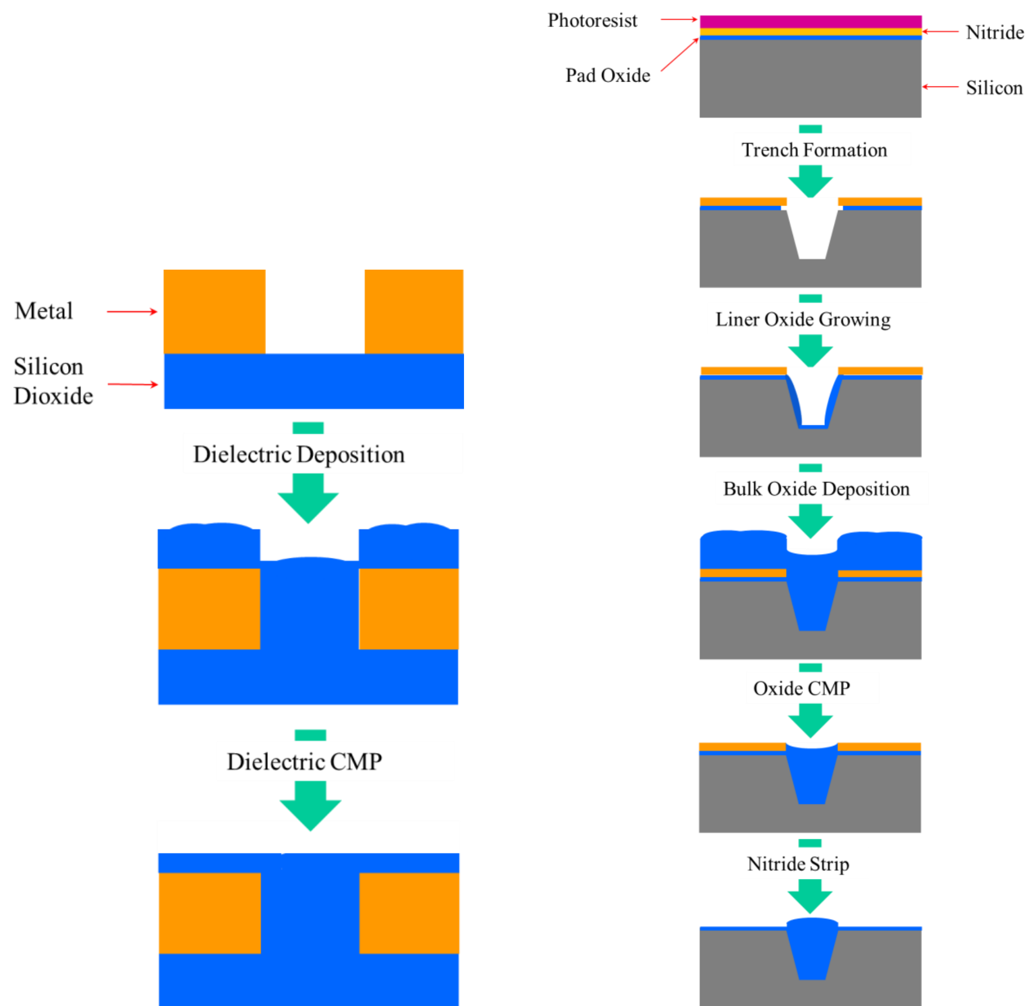

Figure 1.7: Schematic of ILD (left) and STI formation processes (right) (figures are not drawn to scale) (Liao 2014).

1.3.2 STI CMP

STI structure is used to separate active devices in the front end of line (FEOL) for IC fabrication. As feature sizes scale down to the deep sub-micron region, STI has replaced the older technology that was local oxidation of silicon (LOCOS). Compared to LOCOS, STI can deposit dielectrics at a lower temperature and prevent the so-called bird's beak issue caused by oxide growth (Plummer *et al.* 2000). The image on the right of Figure 1.7 shows the STI formation process. A thermal oxide layer and a nitride layer are sequentially formed on the silicon substrate, which are followed by the formation of a shallow trench via photolithographic and etching techniques. The trench is then filled with oxide. CMP is used to remove the excess oxide layer with the nitride layer working as the polishing stop layer. In the end, the nitride layer is stripped.

1.3.3 Cu CMP

Current technology in IC fabrication employs copper as interconnects since it has a lower resistivity than the previous metal of choice, aluminum (Wolf 2004). Copper interconnects are typically formed via a damascene process; CMP is an indispensable step in this process. The image on the left of Figure 1.8 shows the Cu damascene formation process. Trenches in the ILD layer are initially created using photolithographic and etching techniques. A thin, conformal barrier layer (usually Ta/TaN) is then deposited via physical vapor deposition (PVD) or chemical vapor deposition (CVD). Since Cu has poor adhesion to dielectric materials such as SiO_2 and tends to diffuse into SiO_2, the barrier layer is used to address the adhesion and diffusion issues. Subsequently,

Cu is filled into the trenches by electroplating. In the end, a multistep Cu CMP process is used to remove the overburden Cu and barrier layer. The overburden Cu is initially removed (i.e. bulk Cu removal), which is followed by a Cu clearing step. The last step is the barrier layer clearing (Li 2008).

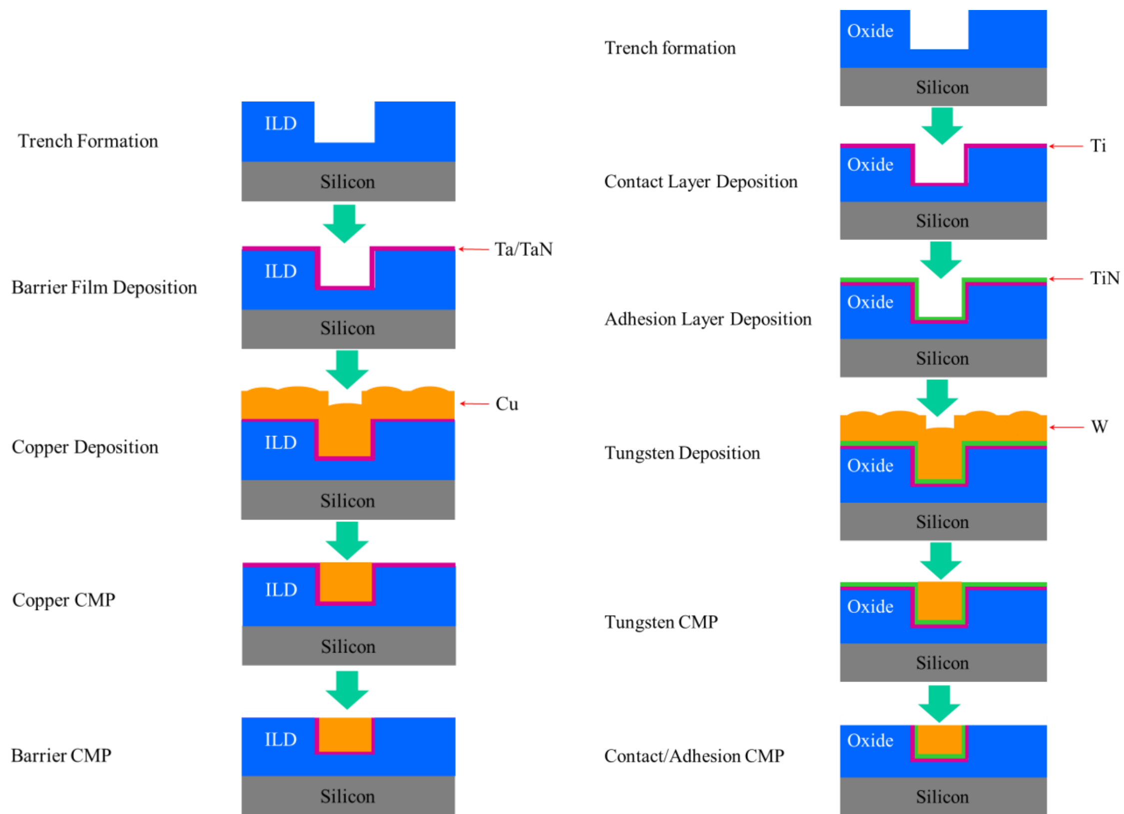

Figure 1.8: Schematic of Cu-damascene (left) and W-plug (right) formation processes (figures are not drawn to scale) (Liao 2014).

1.3.4 W CMP

W is used as the metal plug to connect the transistors and the first Cu interconnects, as shown in Figure 1.3. The image on the right of Figure 1.8 illustrates the

general steps involved for W-plug formation. Similar to Cu interconnect formation, W-plug is also built via the damascene process. Trenches in the dielectric layer are initially created using photolithographic and etching techniques. A contact layer (Ti) and an adhesion layer (TiN) are then sequentially deposited. W is then filled into the trenches by low pressure chemical vapor deposition (LPCVD). In the end, CMP is used to remove the overburden W as well as Ti and TiN.

1.4 Consumables in CMP

As shown in Figure 1.5, CMP employs many consumables such as wafer, polishing pad, slurry, retaining ring, and pad conditioner. This section will discuss polishing pad, slurry and pad conditioner in detail.

1.4.1 Polishing Pad

Polishing pad plays a significant role during CMP. Pad asperities offer mechanical action to remove the chemically modified wafer surface. Also, pad transports fresh slurry to the pad-wafer interface through its surface topography and/or grooves. In addition, pad transports used slurry and polishing byproducts away from the pad-wafer interface (Liao 2014).

The pad must have sufficient mechanical integrity and chemical resistance since it is subjected to repeated mechanical stress and constant chemical attacks during polishing. Also, the pad must be sufficiently hydrophilic to carry and deliver slurry efficiently (Li

2008). Currently, for most commercially available pads, polyurethane is selected as the material of choice.

Polyurethanes are typically synthesized from polyol, diisocryanate or isocyanate derivatives and chain extender (Oliver 2004). The polyols are mostly polyethers with terminal hydroxyl groups, and the diisocryanate or isocyanate derivatives are based on either toluene diisocyanate (TDI) or diisocyanato-diphenylmethane (MDI) and its derivatives (Li 2008). The chemical components impact pad physical properties and polish performance.

The physical properties of a polishing pad include pad macrostructures and microstructures. The macrostructures typically refer to perforations and surface grooves, which are designed for several reasons (Oliver 2004; Muldowney 2004):

1. Act as channels to transport fresh slurry to the pad-wafer interface.
2. Work as channels to remove used slurry and polishing debris from the pad surface.
3. Ensure slurry is uniformly distributed across the pad surface to improve removal rate uniformity on a wafer scale.
4. Prevent hydroplaning of the wafer across the pad surface.

Currently, commercially available pads typically have xy, concentric, floral and logarithmic grooves or a combination of these, as shown in Figure 1.9 (Sampurno 2008; Sun 2009). The groove designs impact slurry delivery. Chapter 5 of this dissertation will investigate the effect of groove design on slurry injection schemes during ILD CMP.

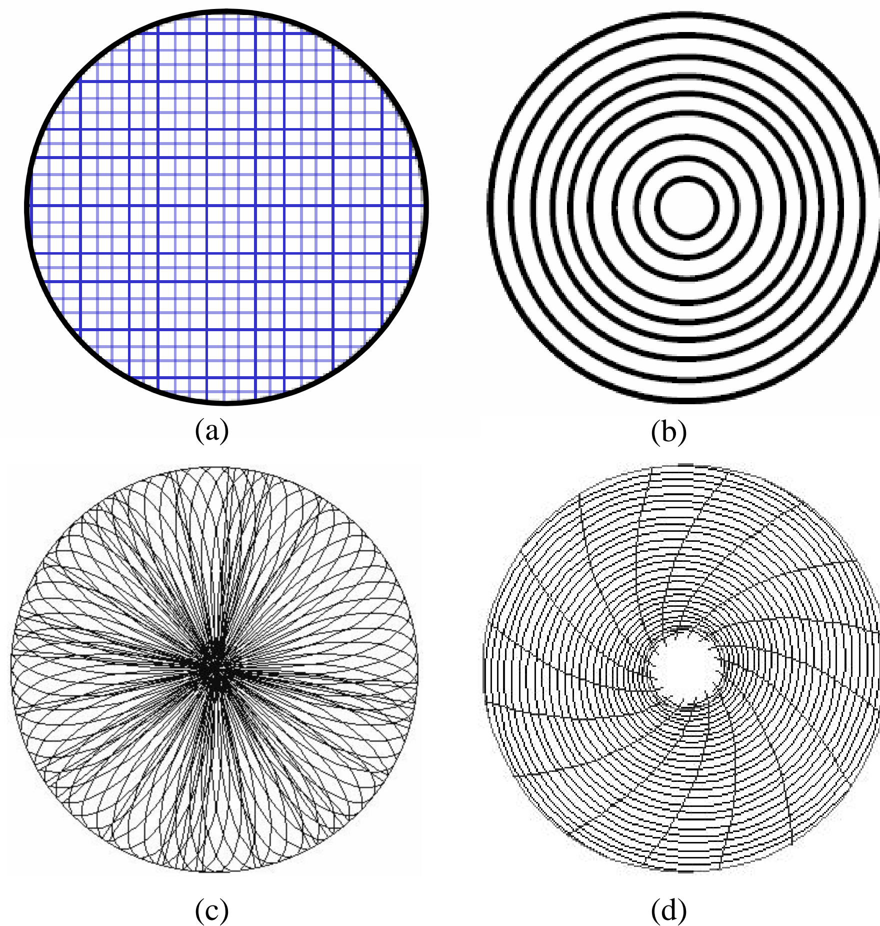

Figure 1.9: Top view of pads with (a) xy, (b) concentric, (c) floral, and (d) logarithmic spiral grooves (figures are not drawn to scale) (Sampurno 2008; Sun 2009).

In addition to pad macrostructures, pad microstructures are also critical. Differentiated by their microstructures, there are four main types of polishing pads: felts and polymer-impregnated (Type I); micro-porous synthetic leathers (Type II); filled polymer films (Type III) and unfilled textured polymer sheets (Type IV). Type I pads have continuous channels between fibers. Suba^{TM} is an example of this type of pad. They

are typically used for Si stock polish and W CMP. Type II pads have vertically oriented open pores. Politex™ and Fujibo™ are examples of this kind of pad, which are used for Si final polish, W CMP and post CMP buff (Li 2008). Type I and Type II pads are relatively soft, providing better global planarity and lower defectivity (Wolf 2004). Type III pads have closed-cell foam. Example pads are Dow IC-1000™ series and Cabot D100™ series. Type III pads can be used for Si stock, ILD, STI and metal CMP. Type IV pads are non-porous and IC 2000™ is an example of this type of pad (Li 2008). The last two types of pads are relatively hard, providing better local planarity and higher planarization efficiency (Wolf 2004). Figure 1.10 shows the cross-sectional scanning electron microscopy (SEM) images of these example pads.

There have been numerous studies on pad surface microstructures. Most of them have focused on pad surface roughness and its effects on polishing performance (Matsumura *et al.* 2008; Yoshida *et al.* 2006; Park *et al.* 2008; Liang *et al.* 1997). In general, a rougher pad surface generates a higher material removal rate and causes more defects. Since the pad surface roughness is extracted from the whole range of the pad surface (i.e. both its up and down feature), and since the down features do not participate in CMP, it does not exhibit high correlation with coefficient friction (COF) and material removal rate (Sampurno *et al.* 2011). Recently, a new descriptor of pad surface micro-texture, referred to as pad surface abruptness (λ), was proposed by our research group and its effect on polishing performance was investigated (Sampurno *et al.* 2011; Liao *et al.* 2011; Liao *et al.* 2013; Liao *et al.* 2014). Unlike the pad surface roughness, pad surface abruptness is extracted from the top asperities that contact the wafer during polishing

(Liao *et al.* 2014). It is therefore expected that it may directly impact COF and material removal. Sampurno *et al*. showed that a pad surface with a larger abruptness rendered a higher COF and tungsten removal rate (Sampurno *et al.* 2011). Liao *et al*. extensively investigated the effect of the pad surface contact area and pad surface abruptness on polishing performance during copper, ILD and STI CMP (Liao *et al.* 2011; Liao *et al.* 2013; Liao *et al.* 2014).

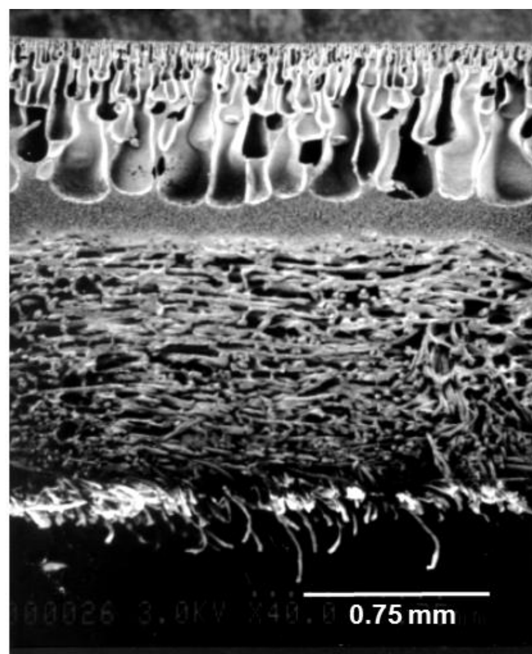

(a) (b)

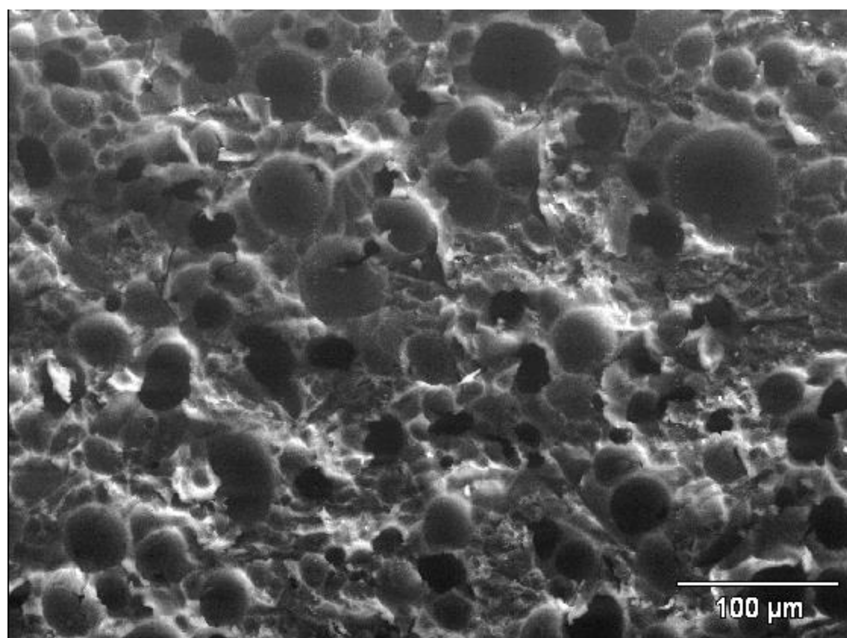

(c)

Figure 1.10: Pad micrographs of (a) Suba^{TM}, (b) Politex^{TM}, and (c) IC1000^{TM} (DOW; JSR).

1.4.2 CMP Slurry

Slurry is another major consumable used in CMP. Slurry provides both chemical and mechanical actions during CMP. More specifically, chemicals in the slurry react with the wafer surface to form a softer porous layer. This layer is then removed by mechanical forces generated by abrasive nanoparticles in slurry as well as pad asperities. Slurry may contain oxidizers, chelating agents, corrosion inhibitors, surfactants, and abrasive particles.

The oxidizer is one of the most important components of the metal CMP slurry. It reacts with the metal surface to raise the oxidation state of the metal. This may result in either dissolution of the metal or the formation of a softer porous layer which can be more easily removed by mechanical actions (Kaufman *et al.* 1991). Numerous oxidizers such as nitric acid, hydrogen peroxide, ferric nitride and potassium permanganate were reported (Caprio *et al.* 1995; Lu *et al.* 2004; Aksu *et al.* 2003). Among these oxidizers, hydrogen peroxide is widely used in today's CMP slurries.

During CMP, the abraded materials may redeposit on the wafer surface, causing surface defects. In order to address this problem, chelating agents are typically added in CMP slurries. For metal CMP slurries, chelating agents react with metal oxides in the slurry to form a metal complex, which has greater solubility than the oxide of metal. As a result, this process facilitates the dissolution of the abraded material. Ammonia, amino acids and organic acids are widely used as chelating agents for CMP slurry (Oliver 2004; Li 2008).

As mentioned previously, the oxidizers chemically modify the metal film for easy removal. One issue is that the chemical attack may lead to isotropic dissolution of the film (Li 2008). More specifically, the chemical attack may result in the dissolution of films in both the protruding area and the lower lying area, resulting in very low step height reduction efficiency. In this case, a corrosion inhibitor is needed to address the issue. Benzotriazole (BTA) is the most commonly used corrosion inhibitor in copper CMP slurries. During CMP, BTA adsorbs on the copper surface to form a Cu-BTA surface complex. This complex film works as a physical barrier between the oxidizer and wafer surface. As such, the lower lying area can be protected while the protrude area can be selectively removed by mechanical action leaving the copper surface free to be oxidized later (Li 2005).

Surfactant is another important component of CMP slurry. Surfactants help control slurry stability. Dispersion stability of slurry abrasive nanoparticles is critical since particle-particle aggregation may significantly increase the mean particle size, which may result in surface defects and enhance the settling of the particles. Surfactants can alter the charge characteristic of the particle, producing strong electrostatic repulsion to help stabilize these particles. Surfactants can also provide steric barrier between particles to enhance the stability of the dispersion (Yu *et al.* 1994).

In addition to the chemical components described above, slurry typically contains abrasive particles. The primary function of these particles is to enhance the abrasiveness of the pad, acting as the chemical "tooth" in the removal process (Sivaram *et al.* 1992).

Particle hardness, shape, size and size distribution are key parameters, which greatly impact the effectiveness of these particles.

A wide variety of materials such as alumina, silica, ceria and diamond have been employed as abrasive nanoparticles in CMP processes. Among them, silica is one of the most commonly used abrasive nanoparticles. Silica particles are produced by either the fuming process (Barthel *et al.* 1998) or the precipitated process (Stober *et al.* 1968).

Fumed silica is synthesized via the combustion process of silicon tetrachloride in an oxygen flame (Barthel *et al.* 1998). In comparison, colloidal silica is made by a wet method. Potassium silicate reacts with a specific acid to form colloidal silica, which can be produced in spherical shape with uniform size distribution (Oliver 2004). Due to their structural formation, fumed silica typically has a larger mean diameter than that of the colloidal silica. As a result, fumed silica may cause more surface defects. Figure 1.11 shows transmission electron microscope (TEM) images of these two types of silica particulates.

Slurry accounts for as much as 45 percent of the total CoO during CMP (Holland *et al.* 2002). In current state-of-the-art technology, fresh slurry is injected onto the pad center area through a single slurry tube. It provides very low slurry utilization efficiencies, ranging from 2 to 22 percent (Philipossian *et al.* 2003). In addition, corrosion chemicals, abrasive nanoparticles and metal ions in the used slurry are harmful to the environment. Therefore, optimizing slurry injection schemes to improve slurry utilization will not only reduce CoO, but also decrease the potential environmental

impact caused by the used slurry. In chapter 5 of this dissertation, different slurry injection schemes will be compared on different pad groove designs.

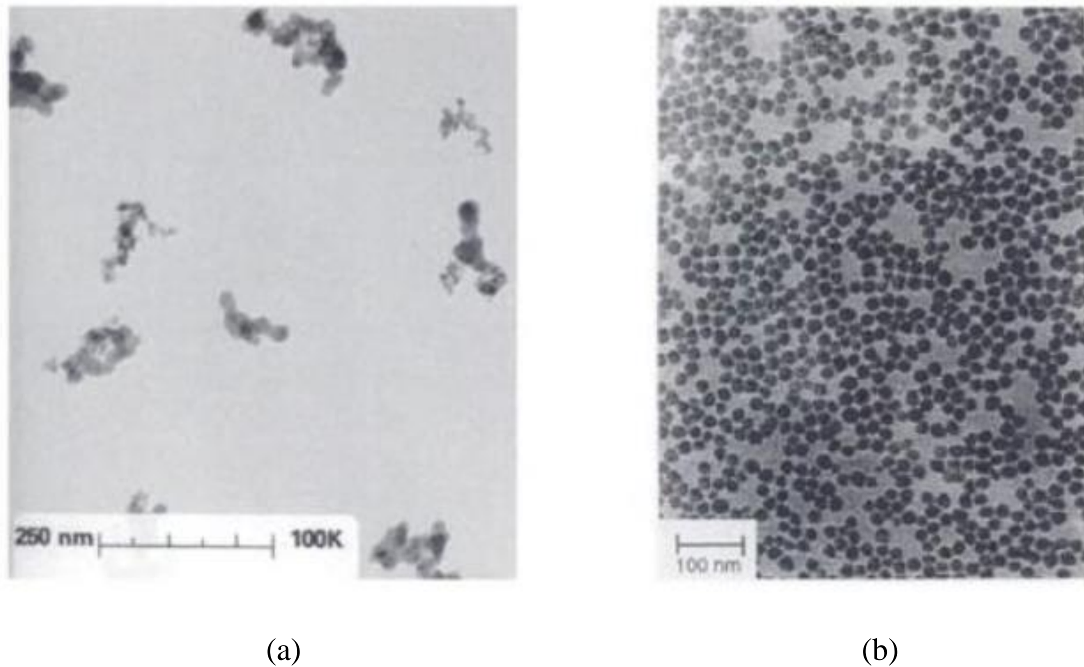

(a) (b)

Figure 1.11: TEM images of (a) fumed silica slurry and (b) colloidal silica slurry (Cabot Microelectronics Corporation; Dow).

1.4.3 Pad Conditioner

Pad conditioning is typically required to prevent material removal rate decay during CMP. More specifically, a pad conditioner is used to regenerate pad asperities and re-open the pores on the pad surface. Without pad conditioning, pad asperities may be flattened by continuous mechanical contact between the pad and the wafer surface; and the pores may be clogged with slurry abrasive particles, pad debris and polishing by-products. This phenomenon is known as pad glazing (Oliver 2004). Pad glazing enhances

the real contact area between the wafer and pad surface and hence decreases the local contact pressure, leading to lower material removal rates (Li 2008). Therefore, pad conditioning greatly impacts pad surface micro-texture, which in turn affects polishing performance in terms of material removal rate, dishing and erosion (Liao 2014).

Our research group has extensively investigated the effect of pad conditioning on pad surface micro-texture and polishing performance. For example, Liao *et al*. employed two different diamond disks to condition an IC1010 M-groove pad, on which 200-mm blanket copper wafers were polished. The fractured and collapsed pore walls generated by one of the disks partly covered the adjacent pores, making the pad surface more lubricated and hence resulting in a significantly lower COF and copper removal rate (Liao *et al*. 2011). In another study, two pad conditioning forces were used during ILD CMP. Results showed that the two forces generated similar pad surface abruptness, but pad surface contact area was significantly lower (by 71%) at the lower conditioning force. Such a dramatic decrease in pad surface contact area resulted in a significant increase in local contact pressure and therefore led to a significant increase in oxide removal rate (Liao *et al*. 2013).

A diamond disk typically consists of tens of thousands of diamonds embedded on a nickel-plated or steel disk. Figure 1.12 shows an SEM image of a top view of a diamond disk.

Diamond size is an important parameter in disk design. As observed in Figure 1.12, diamonds may have different sizes. The size of diamonds is represented by the grit system. Higher grit size number indicates smaller average diamond diameters. Typical

diamond disks can be categorized in several ranges from coarse (16-24 grit), to medium (36-60 grit), fine (80-120 grit) and superfine (150-325 grit) (Sampurno 2008; Sun 2009). In general, the smaller grit sizes are more aggressive than the higher grit sizes. As shown in Figure 1.13, the diamond disk with 200-grit number (i.e. smaller diamond size) fails to completely open pad pores. In this case, the removal rate of the CMP process may drop significantly. In contrast, the disk with 60-grit number (i.e. larger diamond size) is too aggressive and destroys the micro-texture of the pores. This will shorten pad life, which will translate to higher CoO and less tool availability.

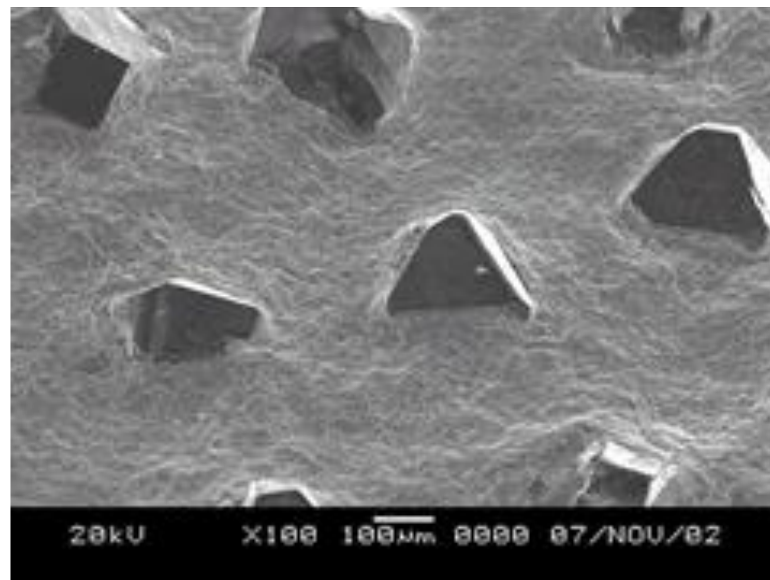

Figure 1.12: SEM image of a top view of a diamond disk (http://www.kinik.com.tw/kinik/products/cmp_en.asp).

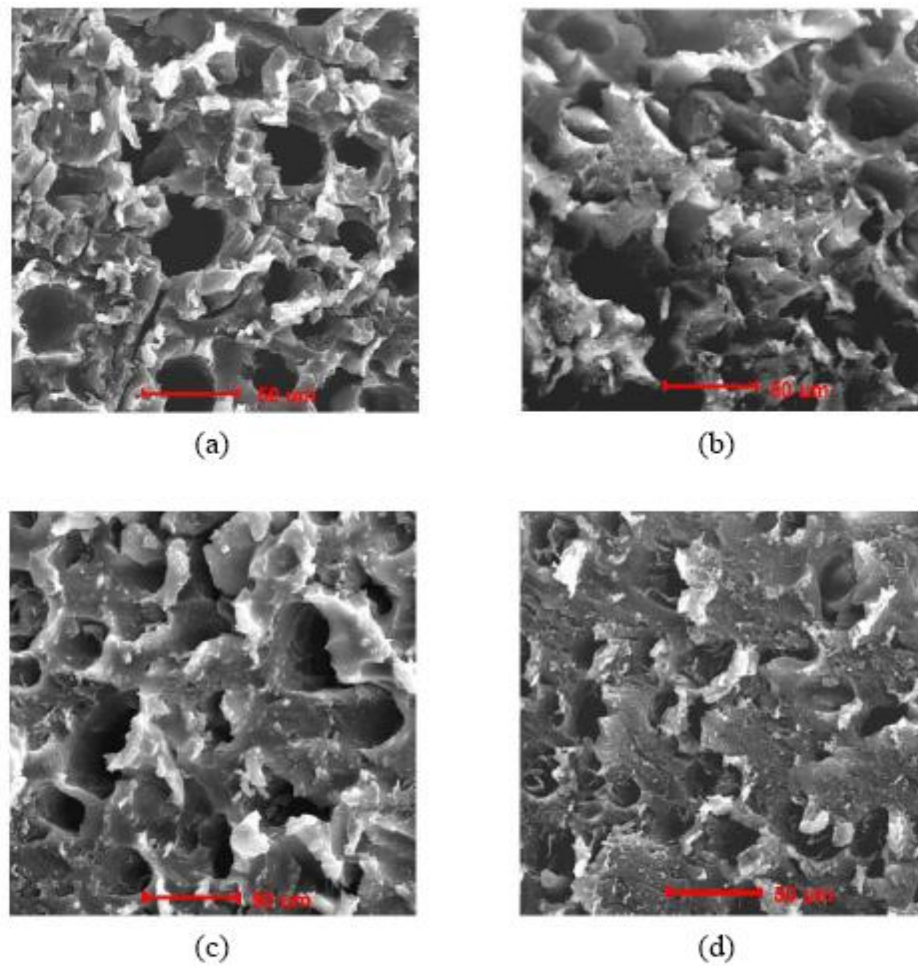

Figure 1.13: SEM images of Freudenberg FX-9 pad conditioned by various sizes of diamond: (a) new pad, (b) 60-grit, (c) 100-grit and (d) 200-grit (Charns *et al.* 2003).

Diamond shape is another critical parameter in disk design. Diamond shape can be either blocky or sharp. Block diamonds lead to lower pad cutting rate, but tend to wear slower. In comparison, sharp diamonds (see Figure 1.12) are more aggressive and render higher pad cutting rates. However, sharp diamonds typically tend to wear quickly and fracture easily (Sun 2009).

During pad conditioning, pad asperities and slurry abrasives make mechanical contact with the diamonds, causing the diamonds to wear. Figure 1.14 shows SEM images of a diamond on the disk before and after 24-hour wear test (Meled *et al.* 2010). Micro-wear was present on the cutting edges of the diamond after the test, as shown in Figure 1.14 (b). Diamond wear leads to the loss of disk effectiveness (Wu *et al.* 2013). Due to diamond wear, a conventional diamond disk is typically replaced after dozens of hours of use (Borucki *et al.* 2007). To provide a better understanding of diamond wear and its impacts on the process, aggressive diamond characterization and wear analysis during CMP will be studied in Chapter 6 of this dissertation (Wu *et al.* 2013).

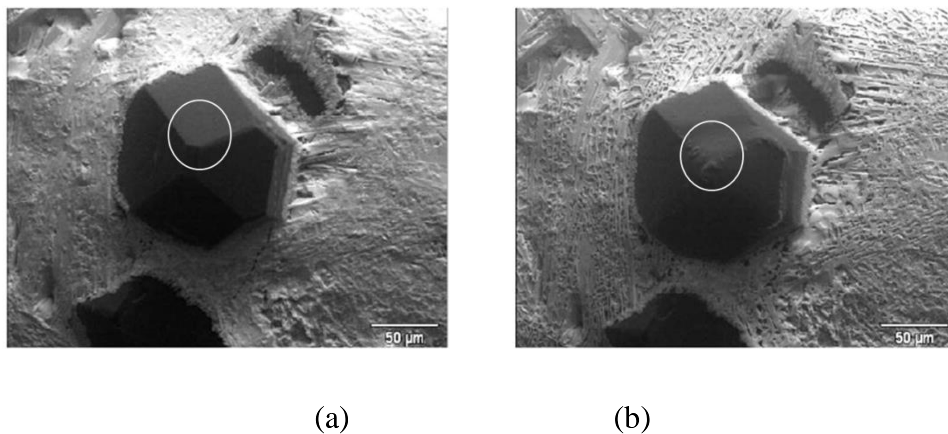

(a) (b)

Figure 1.14: SEM images of an aggressive diamond (a) before and (b) after the 24-hour wear test (Meled *et al.* 2010).

1.5 Challenges in CMP

As an enabling technology, CMP has been widely used in IC processing to achieve local and global surface planarity. But CMP also faces many challenges such as

film thickness control, surface defect reduction, dishing, erosion, CoO and environmental considerations (Fu *et al.* 2001; Wolf 2002; Wolf 2004; Holland *et al.* 2002; Philipossian *et al.* 2003).

1.5.1 CMP Film Thickness Control

CMP is not considered a well-controlled process by today's IC manufacturing standards. Compared with film deposition and etching processes, CMP film thickness control, whether across wafer radius or wafer to wafer, is poor (Li 2008).

Figure 1.15 shows an example of removal rate profile where the copper removal rate is shown as a function of distance from the wafer center. As evident in Figure 1.15, wafer edge is polished faster than wafer center. The variation in removal rate across wafer radius impacts within wafer removal rate non-uniformity (WIWRRNU), which is a critical parameter to determine film thickness planarity at a global (i.e. wafer-scale) level. This is essential for the dimensional accuracy required for the subsequent photolithographic processes and grossly impacts yield (Fu *et al.* 2001).

As such, several methods have been proposed to improve WIWRRNU. These methods include the polishing head with multiple pressure zones, retaining ring pressure adjustment, process condition optimization (i.e. pad/wafer angular velocity adjustment), novel CMP process (i.e. "face-up" CMP), and so forth (Wang *et al.* 2011; Lee *et al.* 2009; Mau 2008). While the above methods help improve WIWRRNU, all of them are mechanical in nature. In Chapter 4 of this dissertation will present a totally different pathway, chemical in nature, to improve WIWRRNU (Wu *et al.* 2015).

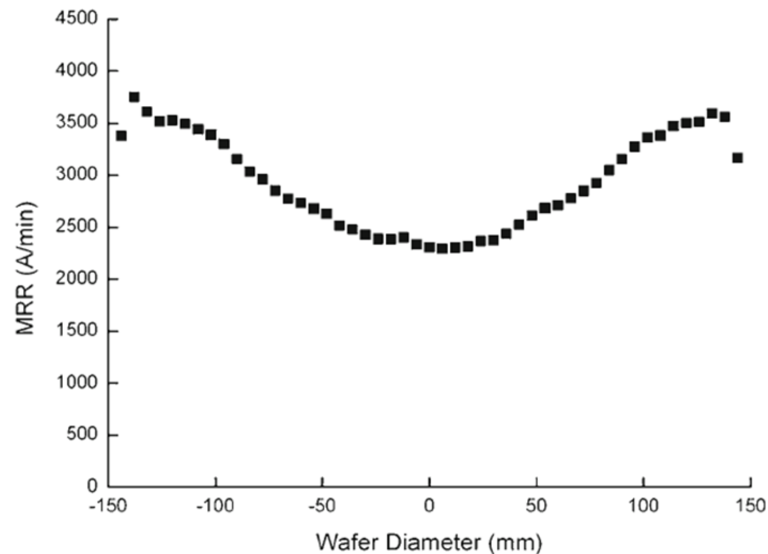

Figure 1.15: Example removal rate profile (Wang *et al.* 2013).

In comparison, wafer to wafer control of thickness is mainly improved by employing end-point detection methods. End-point detection monitors the state of the wafer surface (film thickness, reflectivity, etc.) or of the entire polishing system (friction, motor torque, etc.) to predict when the process is done (Li 2008). End-point detection methods can be classified as optical, electrical, thermal and frictional based on their working principles. Among these, the optical method is the most practical one. The optical module is installed inside the platen, at the periphery of the platen or inside the wafer carrier head, and the light is directed to the wafer surface (Hocheng *et al.* 2003). For oxide CMP, the change in oxide film thickness can be measured by the changes in wavelength of the reflected light. In comparison, for metal CMP, the removal of a reflective surface tells the endpoint of the process. However, one of the disadvantages of this method is that it relies on one point on the wafer surface to represent the condition

across the whole wafer surface. This may give a wrong end-point for the process (Hocheng *et al.* 2003).

1.5.2 Surface Defect Reduction

Surface defect reduction is a great challenge to CMP. Figure 1.16 shows various types of surface defects which are commonly found after CMP processing. These defects are mainly related to foreign objects, large abrasive particles, defective pads, dislodged diamonds, pad debris, and so forth (Sun 2009; Meled 2011). For example, organic residue from the slurry or the cleaning solution may remain on the wafer surface after polishing. Also, metal ions from chemical and abrasive nanoparticle manufacturing can significantly degrade IC performance. In addition, as soft, low-*k* dielectric materials are employed, damage defects become another significant source of concern. Scratches across the wafer are not uncommon with these soft films (Li 2008).

Depending on the severity of the defect, wafers may need to be re-processed or even discarded; hence reducing the throughput. To reduce surface defects, in some cases, a buffing step is implemented as a part of CMP process. For example, the buffing step is employed to remove residues and particles, and to correct some minor defects at the end of a Cu or W CMP process (Shen *et al.* 1998; Hegde *et al.* 2003). Recently, our research group has developed a novel slurry injection system, which can also reduce surface defects (Meled *et al.* 2011; Philipossian *et al.* 2014). As the novel slurry injection system blocks used slurry containing polishing by-products and pad debris from re-entering the pad-wafer interface, it generates lower polishing defects than the standard slurry

application method. In addition, a post-CMP scrubbing process can help correct some defects. In this process, both mechanical (i.e. brush scrubbing) and chemical (cleaning solutions) actions are used.

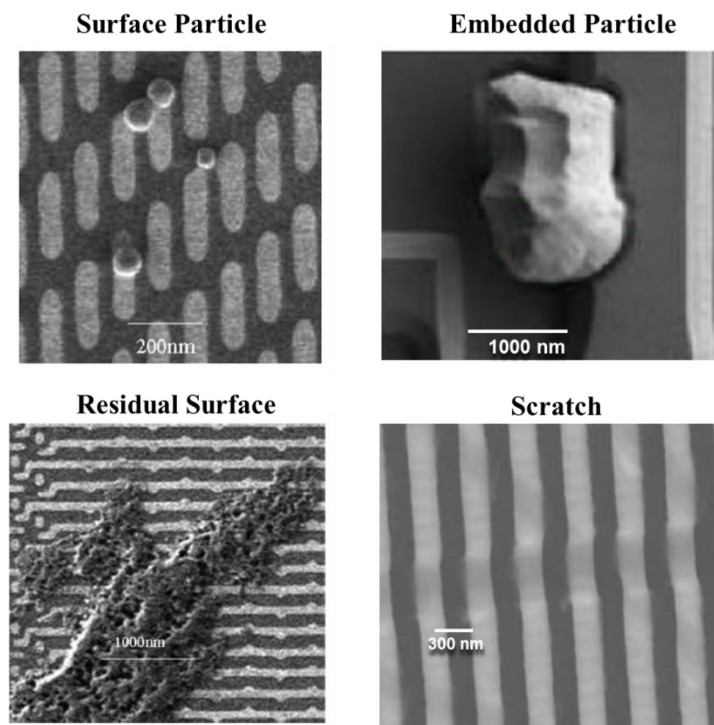

Figure 1.16: Various types of surface defects (Tseng *et al.* 2014; Becker *et al.* 2007; Choi *et al.* 2009).

1.5.3 CoO and Environmental Considerations

CMP is one of the most expensive unit processes in IC manufacturing. The CoO includes consumables (pad, wafer, slurry, diamond disk, etc.), equipment, labor, and other spending. Figure 1.17 shows these factors contributing to the total CoO of the CMP module (Holland *et al.* 2002). As indicated in Figure 1.17, the usage of slurry and pad

accounts for approximately two thirds of the total CoO of CMP, which makes the study of consumables very important.

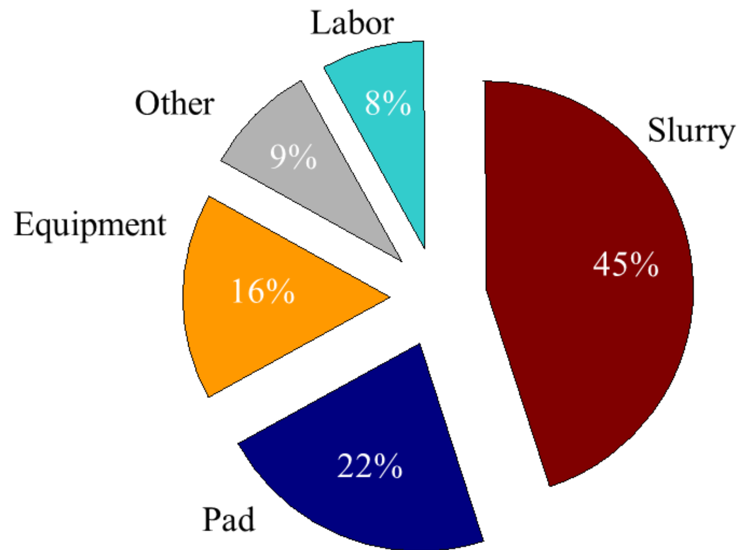

Figure 1.17: Factors contributing to the total CoO of the CMP module (Holland *et al.* 2002).

CMP slurry represents approximately 45 percent of the total CoO, as shown in Figure 1.17. In current state-of-the-art technology, fresh slurry is injected onto the pad center area through a single slurry tube, as shown in Figure 1.5. In some processes, a significant portion of the fresh slurry may flow directly off the pad surface due to inertial forces without ever entering the pad-wafer interface. As such, this method offers low slurry utilization efficiencies, ranging from 2 to 22 percent (Philipossian *et al.* 2003). In addition, corrosion chemicals, abrasive nanoparticles and metal ions in the used slurry are harmful to the environment. Therefore, optimizing slurry injection schemes to improve

slurry utilization is critical to achieving a more cost effective and environmental benign process (Meled 2011). Chapter 5 of this dissertation will underscore the importance of optimum slurry injection schemes.

Polishing pad accounts for 22 percent of the total CoO, as shown in Figure 1.17. Extending pad life can not only reduce the expense associated with pad replacement, but it also can increase tool availability. In addition, groove design on the pad surface is critical to delivering slurry. This significantly impacts slurry utilization efficiency (Philipossian *et al.* 2003). In Chapter 5 of this dissertation, the effect of pad groove design on slurry injection schemes will be investigated.

CMP diamond disk is another important consumable, which is commonly used for pad conditioning to prevent removal rate decay during CMP. Due to diamond wear, a conventional diamond disk is typically replaced after dozens of hours of use (Borucki *et al.* 2007; Wu *et al.* 2013). Therefore, it is important to investigate diamond wear and the loss of disk efficiency. Chapter 6 of this dissertation will provide a better understanding of diamond wear and its impacts on the disk efficiency during CMP.

1.6 Research Motivation and Goals

The primary motivation of this dissertation is to understand the fundamentals of CMP technology and to explore solutions to the challenges outlined in Section 1.5. The results of this dissertation can be beneficial not only by achieving improved polishing performance but also by addressing the CoO and environmental problems. There are

three primary studies in this dissertation (presented in separate chapters). The motivation and goals of each study are described below:

- *Pad Surface Thermal Management during Copper Chemical Mechanical Planarization* (Chapter 4): WIWRRNU is a critical parameter for determining film thickness planarity at a global (i.e. wafer-scale) level. It also grossly impacts the throughput. The objective of this study is to show the feasibility of adopting a new, and much more economical, method to improve WIWRRNU during copper CMP that is solely based on intentional local temperature manipulation of the pad. In this study, a pad surface thermal management system is developed. This system consists of one or more thermal transfer modules, which contact the pad surface during polishing. The system is used to adjust the "center-fast" removal rate profile to illustrate its effect during the process. Results show that, when two thermal transfer modules are employed, local removal rates in the wafer center region decrease significantly while maintaining the removal rates near the wafer edge thereby significantly improving WIWRRNU.

- *Effect of Pad Groove Design on Slurry Injection Scheme during Interlayer Dielectric Chemical Mechanical Planarization* (Chapter 5): Slurry represents as much as 45 percent of the total CoO in CMP and its utilization efficiency in the current state-of-the-art slurry injection method is very low, depending on

pad groove types and process parameters. Moreover, used slurry causes gross environmental effects. As such, optimizing slurry injection schemes is very important to reduce CoO and the environmental effects. In this study, different slurry injection schemes are compared, in terms of material removal rate, on a concentrically grooved pad and an xy-groove pad, respectively. This study underscores the importance of optimum slurry injection schemes for different pad groove designs.

- *Aggressive Diamond Characterization and Wear Analysis during Chemical Mechanical Planarization* (Chapter 6): Diamond disk is commonly used for pad conditioning to prevent removal rate decay during CMP. However, due to diamond wear, a conventional diamond disk is typically replaced after dozens of hours of use. Therefore, it is important to investigate diamond wear and loss of disk efficiency. In this study, a 3M A3700 diamond disk is used to condition a Cabot Microelectronics Corporation D100 pad for 30 hours, and the extent wear on its aggressive diamonds is analyzed. Results show a general trend for conventional diamond disks during their early life: the disk initially loses its aggressiveness due to wear of its original aggressive diamonds; as the original aggressive diamonds wear out, new aggressive diamonds are "born", but these new aggressive diamonds are less aggressive than the original aggressive diamonds; the disk aggressiveness can be maintained if these new aggressive diamonds withstand further wear.

CHAPTER 2

EXPERIMENTAL APPARATI

The studies in this dissertation utilize a large scale CMP polisher and several analytical tools. All polishing tests are performed on the Araca APD-800 polisher and tribometer, which is described in Section 2.1. The analytical tools used in this work are as follows:

- Four-point probe
- Reflectometer
- Infrared (IR) camera

The general configurations and working principles associated with the above tools are described in Section 2.2.

2.1 The Araca APD-800 Polisher and Tribometer

The APD-800 is a single-platen polisher and tribometer designed for 200 and 300 mm wafer polishing. It can be also converted to a 450 mm polisher for research and development purposes by installing a special interface module onto the wafer carrier head (http://www.aracainc.com/products/apd-polishers; Jiao *et al*. 2012).

The APD-800 is manufactured by Fujikoshi Machinery Corporation with signal acquisition and analysis hardware/software integrated by Araca Inc. It has the unique ability to acquire real-time shear force and down force during polishing (APD-800 operations manual). Figure 2.1 shows the main hardware components of the APD-800.

Their functions are listed in Table 2.1 and will be described in detail in the subsequent sections.

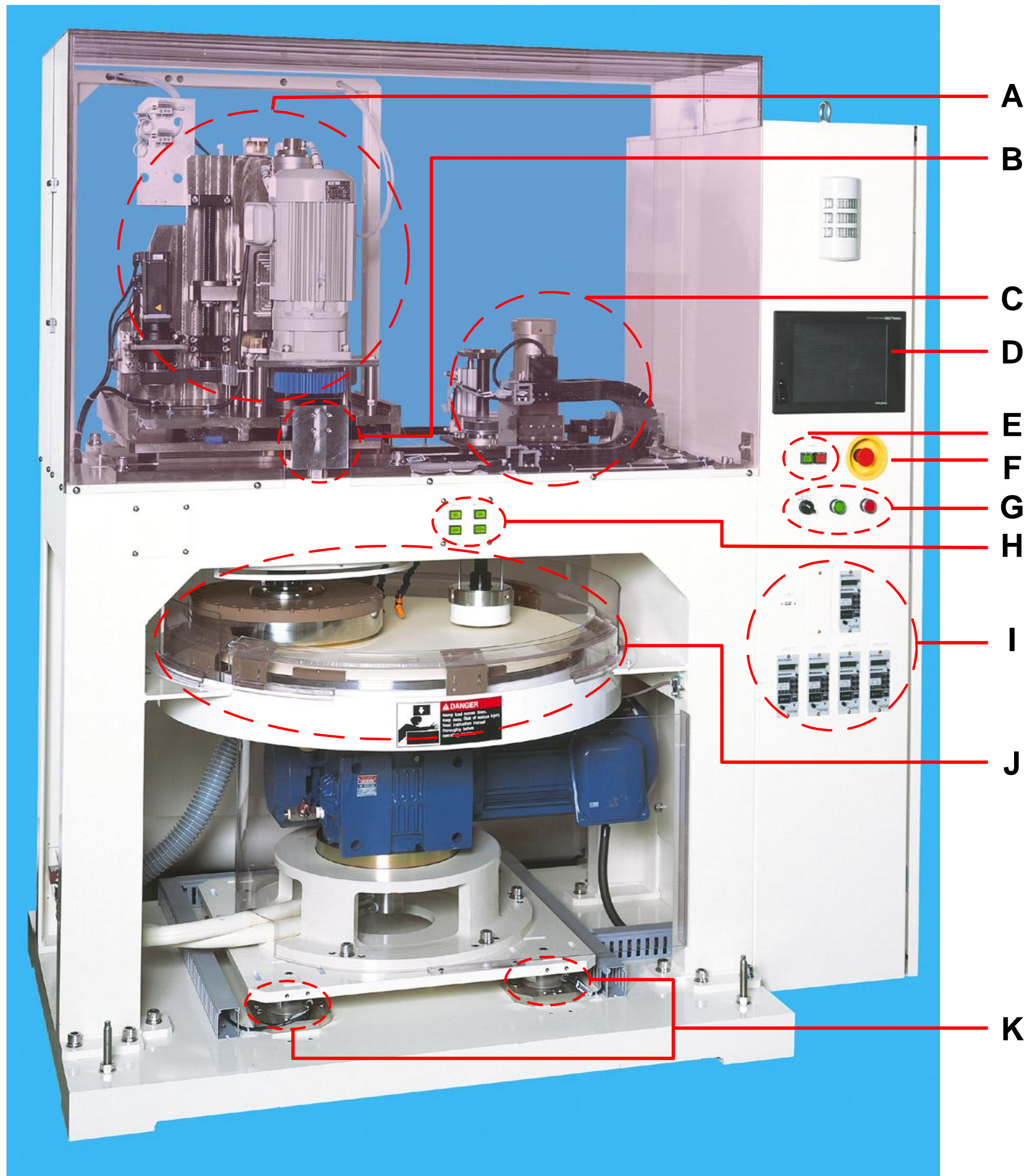

Figure 2.1: The Araca APD-800 polisher and tribometer (APD-800 operations manual).

Table 2.1: Parts of the APD-800 and their functions (APD-800 operations manual)

Part	Part Name	Function
A	Wafer carrier motor	Operate rotation and vertical movement of wafer carrier
B	Shear force load cell	Measure real-time shear force
C	Conditioner carrier motor	Operate rotation and oscillation of conditioner carriers
D	Control panel	Control hardware operation
E	Secondary ON/OFF switch	Turn on/off the APD-800
F	Emergency stop switch	Turn off the APD-800 immediately in case of emergency
G	Automatic run switches	Run polishing sequence with automatic set up
H	Manual control switches	Manually attach/release wafer and raise/lower wafer carrier
I	Signal amplifiers	Reset and amplify force signal from load cells
J	Platen, wafer and conditioner carriers	See Sections 2.1.2 – 2.1.4 for more details
K	Down force load cells	Measure real-time down force

2.1.1 Switches and Control Panels

The APD-800 has several switches and control panels. Figure 2.2 shows the primary ON/OFF switch, which is located on the right side of the APD-800. To turn on the APD-800, the first procedure is to turn on the primary ON/OFF switch. Figure 2.3 shows the manual switches on the front side of the APD-800, which are operated while attaching or releasing the wafer from the carrier head. Functions of these manual switches are summarized in Table 2.2.

Figure 2.2: The primary ON/OFF switch of the APD-800.

Figure 2.3: Manual switches on the front side of the APD-800.

Table 2.2: Manual switches and their functions (APD-800 operations manual).

Part Name	Function
Carrier UP	Raise wafer carrier head
Carrier Down	Lower wafer carrier head
Wafer VAC	Attach wafer to carrier head
Wafer BLOW	Release wafer from carrier head

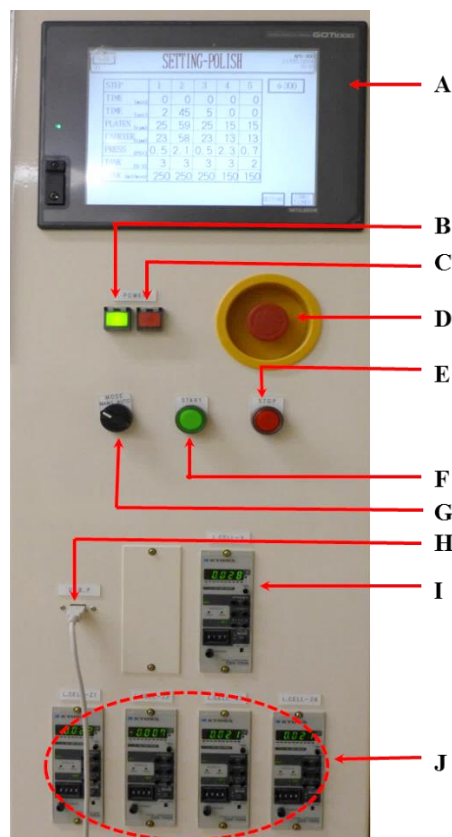

Figure 2.4: The front panel of the APD-800.

Figure 2.4 shows the front panel of the APD-800. Its components' functions are listed in Table 2.3. Among these components, particularly, the control panel controls hardware operations. Through the control panel, users can program the polishing

sequence by setting polishing time, rotation speed of the platen and the carrier head, polishing pressure, and slurry/DI water flow rate for each polishing step (up to 5). Figure 2.5 shows an example of polishing sequence.

Table 2.3: Parts and functions of the APD-800 front panel (APD-800 operations manual).

Part	Component	Function
A	Control panel	Control hardware operation
B	Secondary ON switch	Turn on APD-800 after the primary “ON/OFF” switch is turned on
C	Secondary OFF switch	Turn off APD-800 before the primary “ON/OFF” switch is turned off
D	Emergency stop switch	Stop polisher operations immediately in case of emergency
E	Auto run STOP switch	Stop polishing sequence for automatic run set-up; reset tool after alarm deactivation
F	Auto run START switch	Start polishing sequence for automatic run set-up
G	Manual/auto run switch	Switch run mode between manual and auto
H	USB connector	Connect APD-800 to the PC
I	Shear force conditioner and amplifier	Reset and amplify shear force signal from load cell
J	Down force conditioner and amplifier	Reset and amplify down force signal from load cell

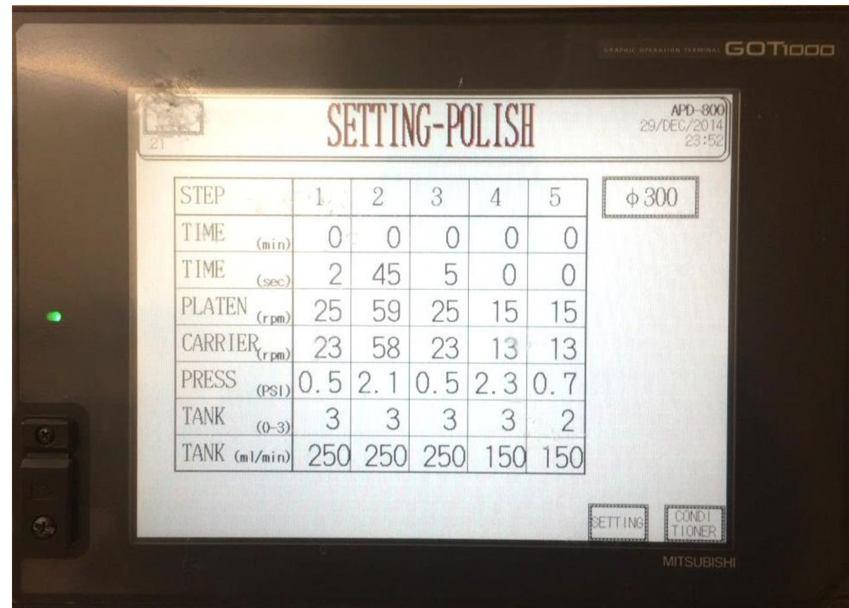

Figure 2.5: An example of polishing sequence defined by the control panel.

2.1.2 Wafer Carrier System

During CMP, a certain pressure is applied on the rotating wafer against a polishing pad. The wafer carrier system offers two basic functions: applying a certain pressure to the wafer and rotating the wafer.

The wafer carrier system of the APD-800 is shown in Figure 2.6. It consists of the carrier head, carrier rotation motor, carrier up/down motor, and two separate vacuum pressure lines. Figure 2.7 shows the ceramic template of the carrier head, which incorporates a pressure chamber inside. One vacuum pressure line applies pressure to this chamber, acting as the down force on the wafer during polishing (Liao 2014). In addition, the bottom of the carrier head has many holes, which allow the other vacuum line to hold the wafer template during polishing (Liao 2014). The carrier rotation motor and carrier

up/down motor are designed for the rotation and vertical movement of the carrier head, respectively.

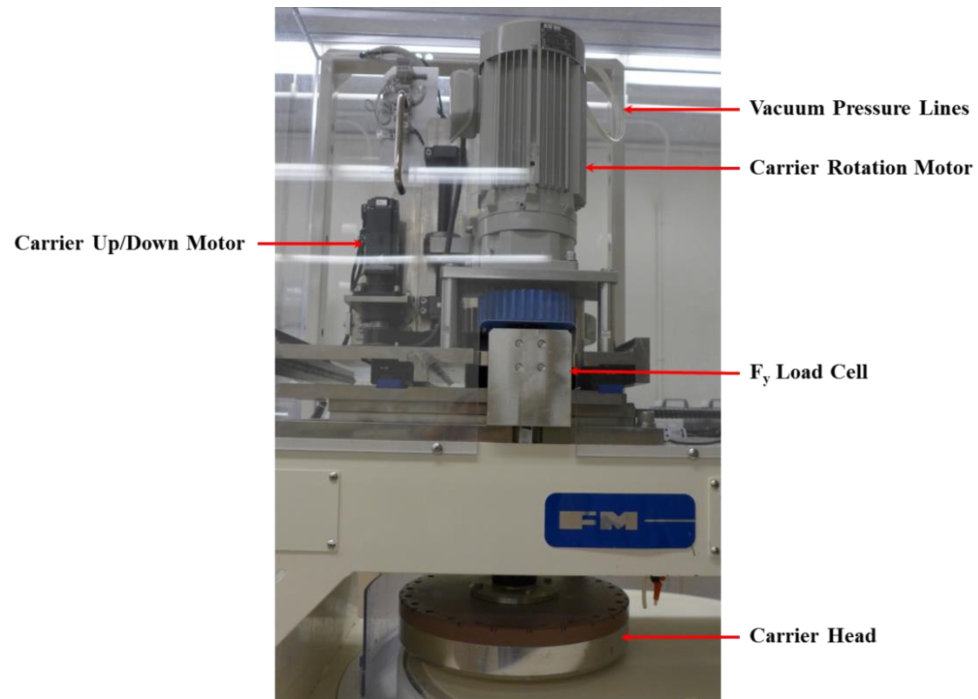

Figure 2.6: Wafer carrier system of the APD-800.

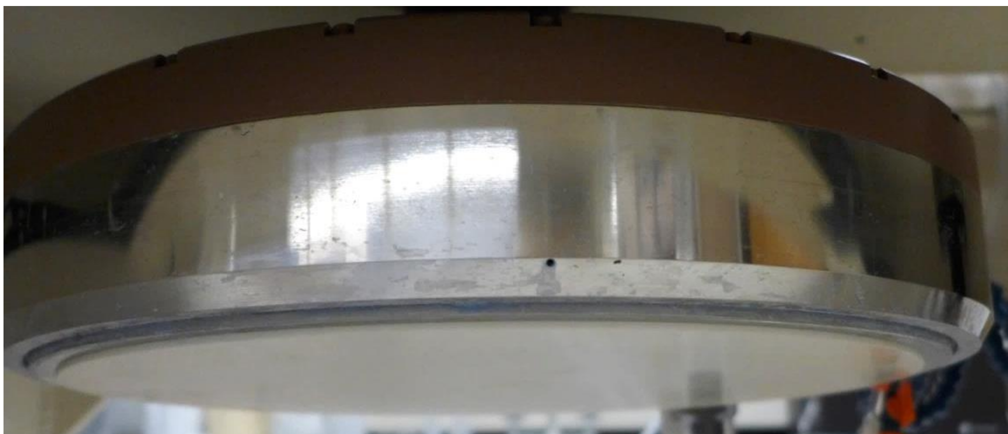

Figure 2.7: Ceramic template of the carrier head.

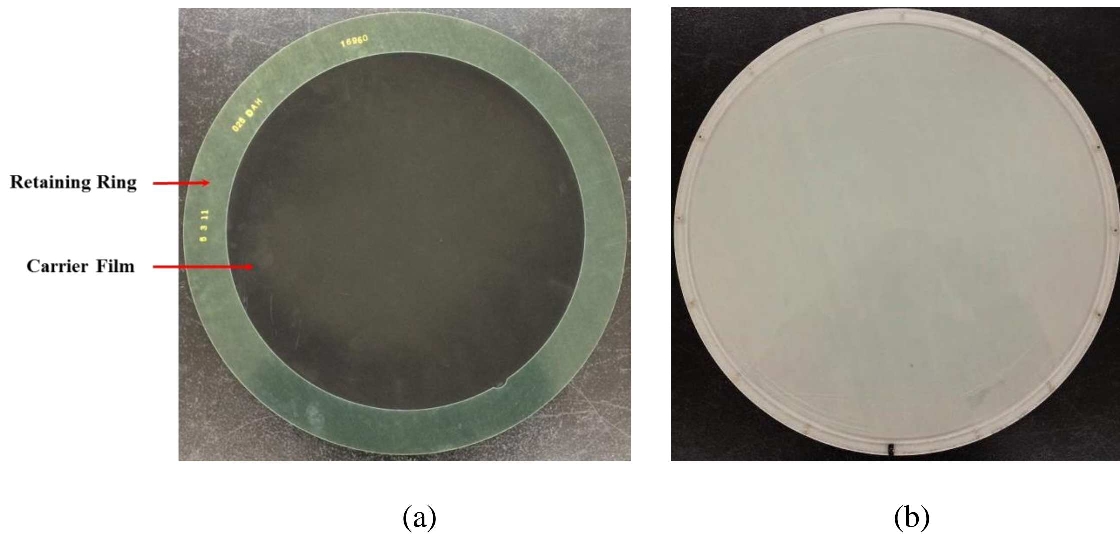

(a) (b)

Figure 2.8: The front side (a) and backside (b) of the wafer template with backing film for 300 mm wafer polishing.

Figure 2.8 shows the wafer template with a backing film designed for 300 mm wafer polishing. The backing film consists of a sheet of carrier film and a retaining ring (Liao 2014). The retaining ring is used to prevent the wafer slipping away from the carrier film during polishing. The inner diameter of the retaining ring is slightly larger than the wafer size and the thickness of the ring is thinner than that of the wafer to be polished. Since the carrier film is porous material, the wafer can be securely held in place through the capillary forces by the wetted carrier film (Jiao *et al*. 2012). Figure 2.8 (b) shows the backside of the wafer template. A ring protrudes along the perimeter of the backside of the wafer template and its inner diameter is designed slightly larger than the ceramic template (Jiao 2012). As such, users can load the wafer to the wafer template and then attach the wafer template to the ceramic template, as shown in Figure 2.9. After attaching the template, the vacuum line is turned on to hold the wafer template. As

mentioned before, the APD-800 can be converted to a 450 mm polisher by installing a special interface module (i.e. wafer template) onto the carrier head. The backside of this module is shown in Figure 2.10. The module (480 mm in diameter) is made of anodized alumina and its back is fitted with an o-ring which ensures a secure fit onto the carrier head using the existing vacuum conditions in the head (Jiao *et al*. 2012).

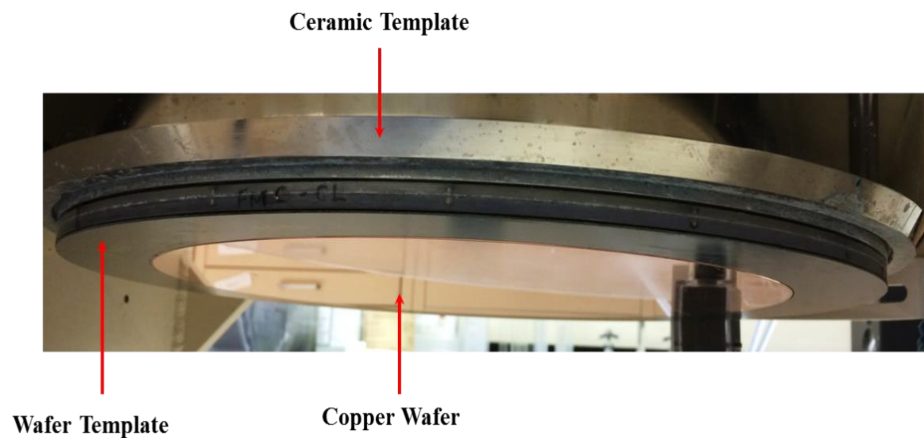

Figure 2.9: The wafer template (with wafer) attached to the ceramic template.

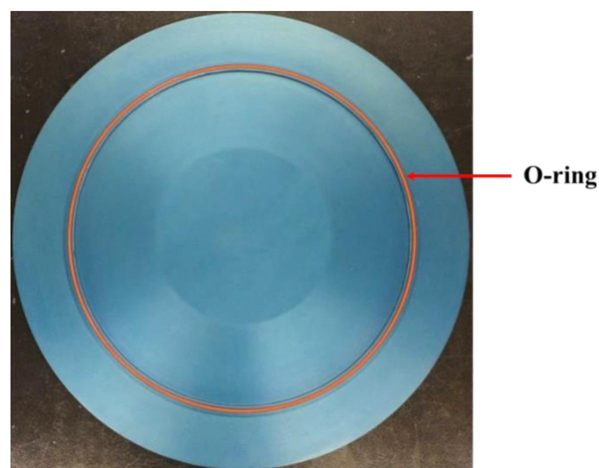

Figure 2.10: The backside of the wafer template for 450 mm wafer polishing.

2.1.3 Polishing Platen System

Figure 2.11 shows the polishing platen system of the APD-800. Polishing pad is attached on top of the polisher platen, which rotates counter clockwise during wafer polishing. The platen has a diameter of 800 mm and is made of alumina (APD-800 operations manual). Since CMP slurry may contain oxidizers and can be highly acidic or basic, alumina is selected as the material of choice to minimize corrosion from chemicals (Sun 2009). The platen rotation is driven by a motor. The body of the platen is set-up on top of 4 load cells. The front two cells are shown in Figure 2.11 and they will be described in Section 2.1.7.

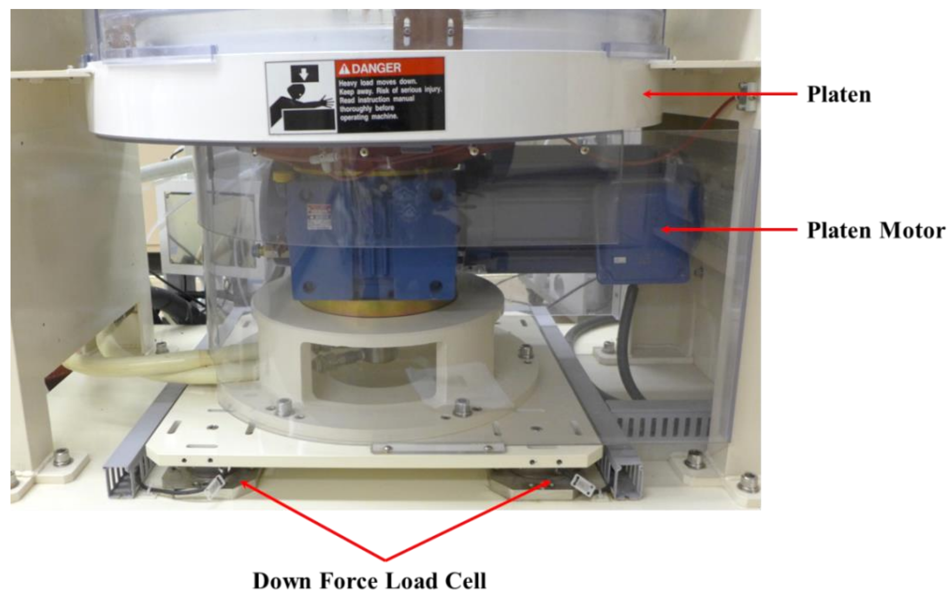

Figure 2.11: The polishing platen system of the APD-800.

2.1.4 Pad Conditioning System

Pad conditioning is required to regenerate pad asperities and remove used slurry and pad debris. The pad conditioning system of the APD-800 is shown in Figure 2.12.

The conditioner rotation motor and the hydraulic piston are designed for the rotation and vertical movement of the conditioner, respectively (Liao 2014). Besides rotation, via the rail (see Figure 2.12), the conditioner sweeps across the radius of the pad surface. Users can set the rotation speed and sweep schedule via the control panel, as shown in Figure 2.4. The sweep schedule can be divided into as many as 10 different zones. Users can input the length of each zone as well as the sweep speed or the dwell time in any defined zone (Liao 2014). In addition, users can also set the conditioning down force via the control panel. A vacuum pressure line (see Figure 2.12) applies pressure to the conditioner through the pressure chamber (Wei 2010), as shown in Figure 2.13.

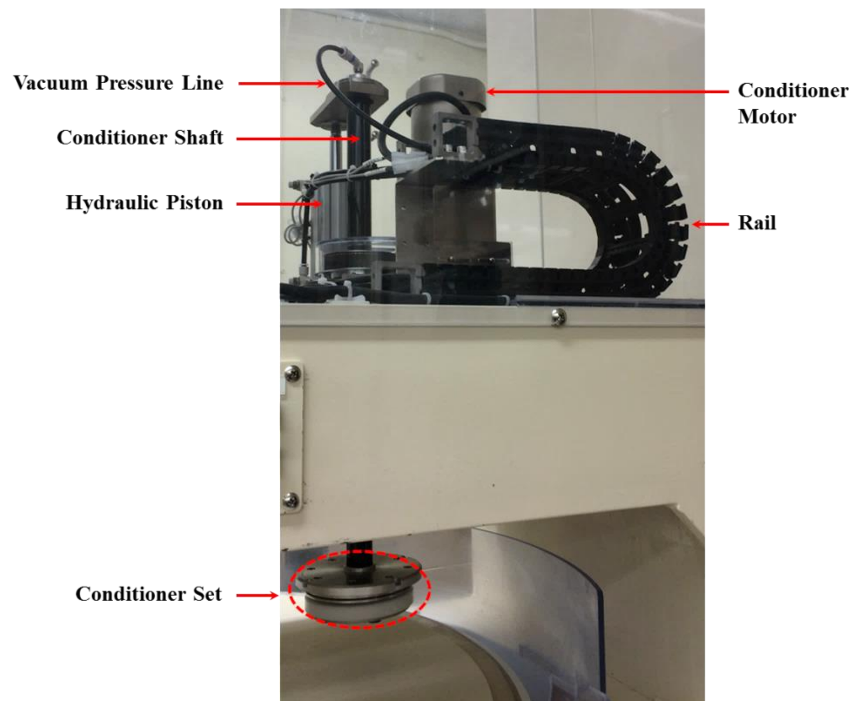

Figure 2.12: The pad conditioning system of the APD-800.

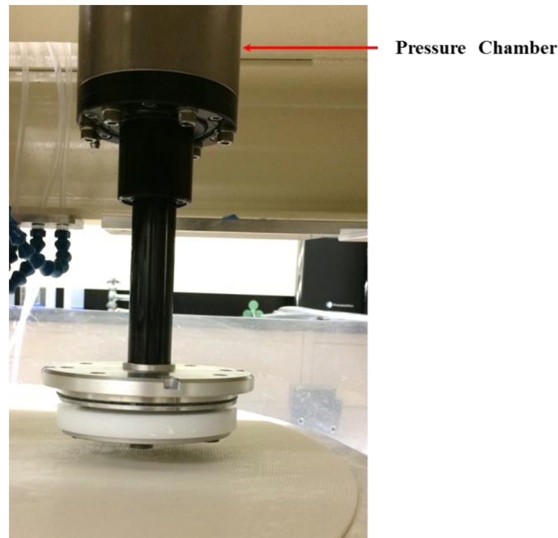

Figure 2.13: Pressure chamber of the pad conditioning system.

2.1.5 Slurry/DI Water Distribution

The APD-800 has three independent tanks for storage of slurry and DI water, as shown in Figure 2.14. Each tank is equipped with a peristaltic pump to delivery slurry/DI water onto the pad surface. The tubing is directed to the pad surface through delivery tubes shown in Figure 2.15.

Figure 2.14: Three slurry/DI water tanks of the APD-800.

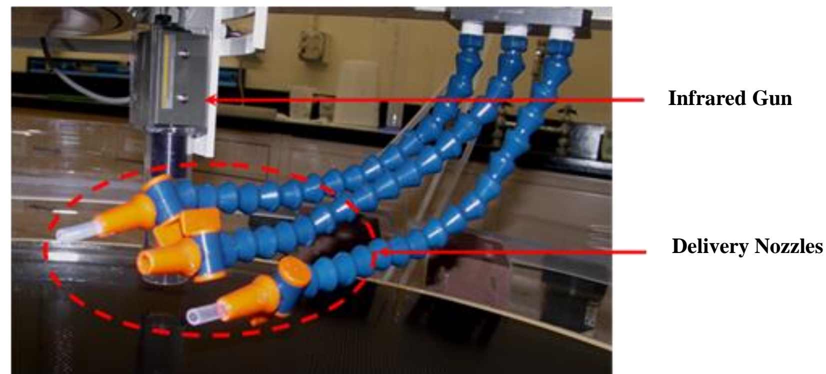

Figure 2.15: Slurry/DI water delivery tubes and the infrared gun (APD-800 operations manual).

2.1.6 Pad Surface Temperature Measurement System

Material removal rate is sensitive to pad surface temperature during a chemically limited CMP process (Sorooshian *et al.* 2003; Li *et al.* 2005). The APD-800 is equipped with an IR gun to measure real-time temperature of the pad surface, as shown in Figure 2.15. The position of the IR gun corresponds to the wafer center track. Essentially, IR gun measures the temperature over a single location. In order to capture the temperature over multiple locations, an external IR camera can be used and will be described in Section 2.2.3.

2.1.7 Force Measurement System

As mentioned previously, the APD-800 is capable of acquiring real-time shear force and down force during polishing. To measure the shear force between the wafer and pad, a sliding table is designed shown in Figure 2.16. The sliding table consists of two plates. The bottom plate is stationary while the upper plate is movable (Philipossian *et al.*

2003). During polishing, the upper plate slides with respect to the bottom plate in only one direction (i.e. the x direction). The degree of sliding is quantified by coupling the two plates to a load cell, which sends a voltage signal to a data acquisition board (Philipossian *et al.* 2003). The relationship between the shear force and voltage signal is pre-calibrated by the manufacturer. As such, the APD-800 reports the shear force associated with a particular voltage reading.

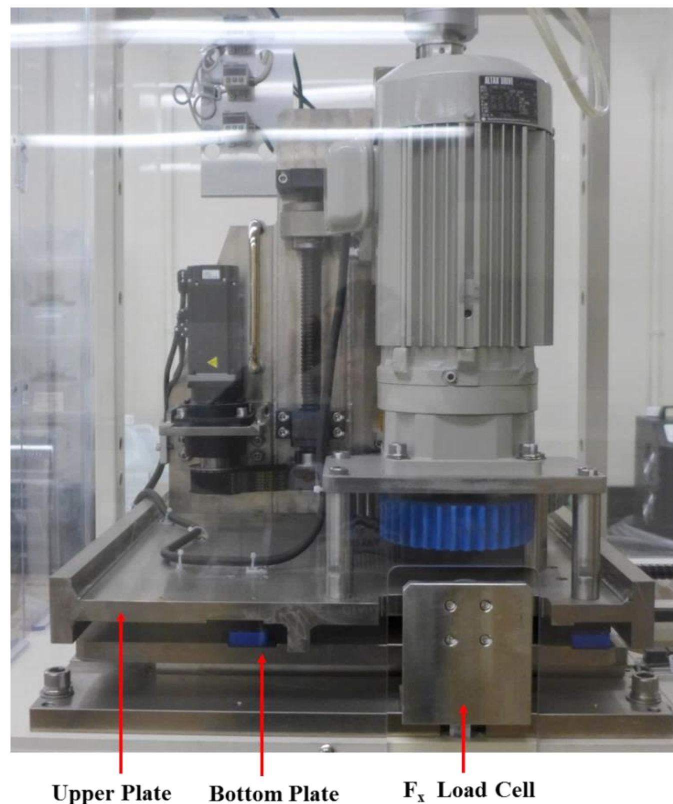

Figure 2.16: Shear force measurement system of the APD-800.

To measure the down force, the APD-800 installs four down force load cells at the bottom of the platen assembly (one at each corner). Figure 2.11 shows the front two

load cells. The down force is reported as the summation of these 4 load cells. As an example, Figure 2.17 shows the shear force and the down force measured during polishing. In the figure, the red and green curves represent the shear force and down force, respectively.

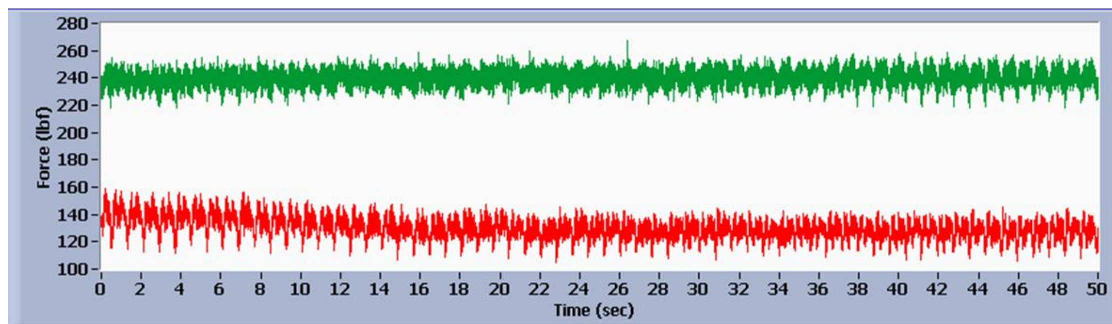

Figure 2.17: Example of shear force and down force measured during polishing.

2.1.8 Data Acquisition Program

As mentioned previously, the APD-800 is equipped with data collection and analysis software integrated by Araca, Inc. The data acquisition program is written in LabVIEW® 8.0 and has two sub-programs: the conditioning down force program and the polishing measurements program. Figure 2.18 shows the interface of the conditioning down force program, which aims to set a baseline for down force measurement. By subtracting the conditioning down force and other down forces generated by pad rotation and slurry flow, users can obtain the actual down force applied on the wafer during polishing (Sun 2009; Liao 2014).

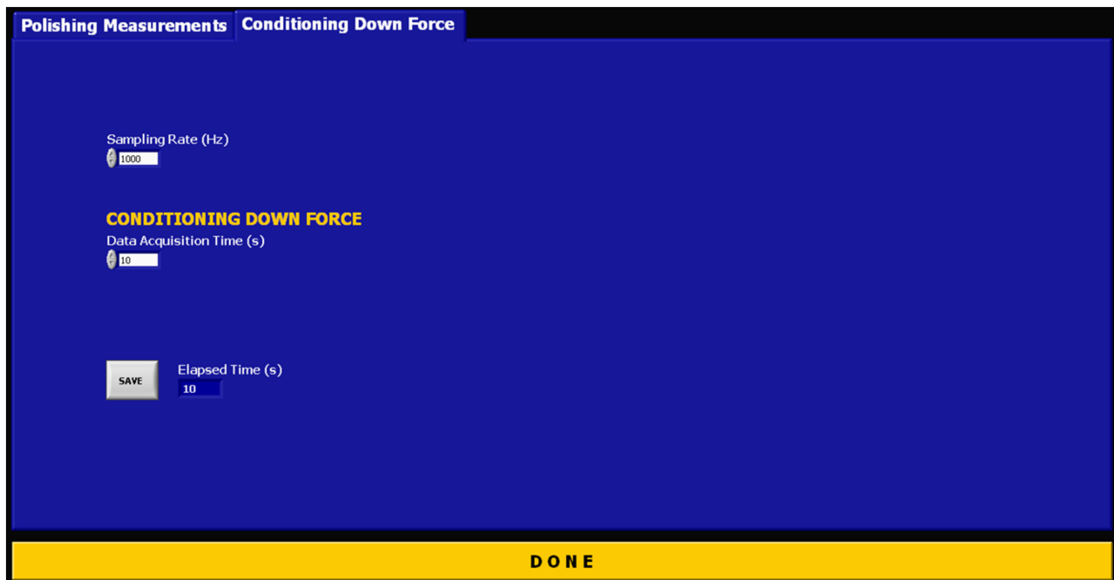

Figure 2.18: Data acquisition program: conditioning down force sub-program.

The polishing measurements program, as shown in Figure 2.19, is used to acquire the real-time polishing parameters. The interface displays the collected data including (APD-800 operations manual):

- Temperature (℃)
- Shear force (lb_f)
- Down force (lb_f)
- Flow rate (ml/min)
- Pad velocity (RPM)
- Wafer velocity (RPM)
- Conditioner velocity (RPM)
- Conditioner position (mm)
- Conditioner oscillation (count/min)

- Conditioner motor current (A)
- Platen motor current (A)
- Carrier motor current (A)

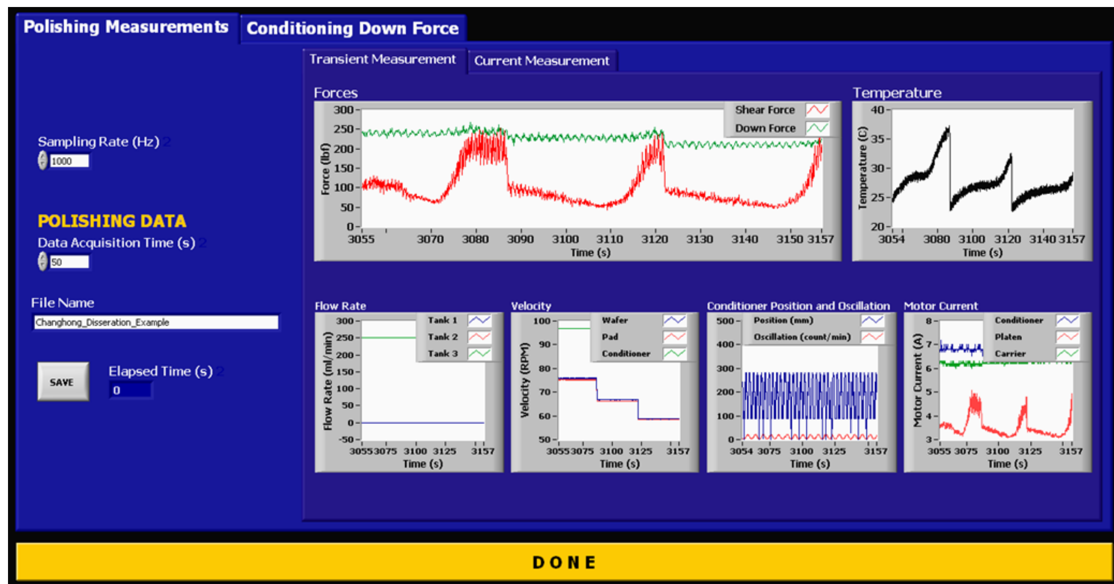

Figure 2.19: Data acquisition program: polishing measurements sub-program.

2.1.9 Data Analysis Program

The data analysis program performs analysis on forces, coefficient of friction (COF), flow rates, kinematics, temperature and motor current (APD-800 operations manual). In this dissertation, COF and temperature analysis are highlighted. COF is defined as the ration of the shear force to the down force. Figure 2.20 shows the interface of COF analysis. COF is shown as a function of polishing time. The mean value and variance of COF can be also attained. Figure 2.21 shows the interface of temperature analysis. The initial, mean and highest pad surface temperatures are reported.

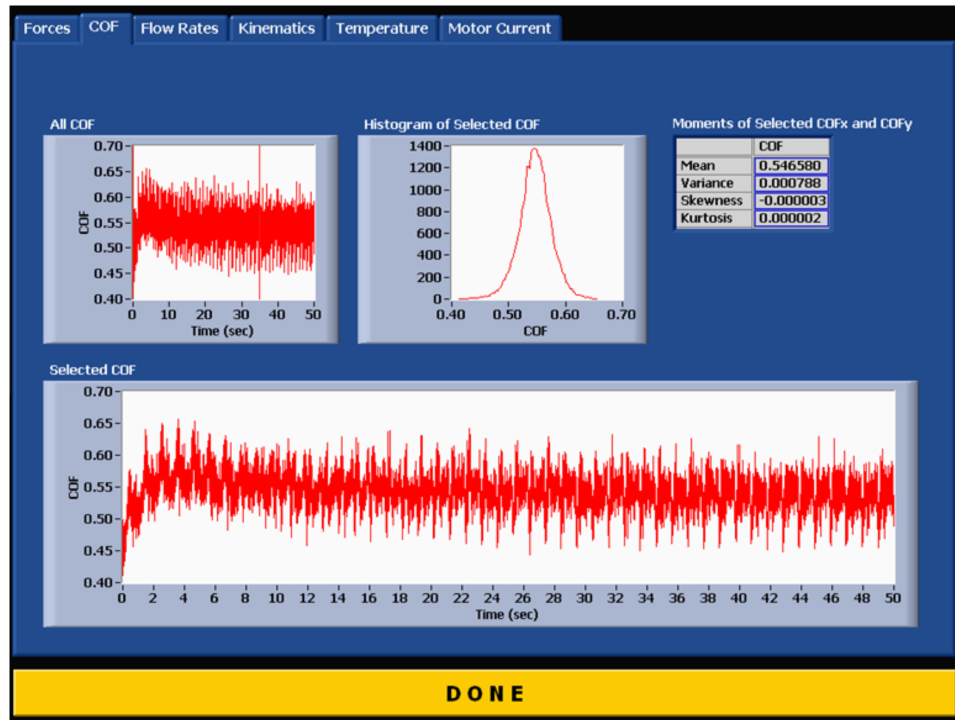

Figure 2.20: COF data analysis.

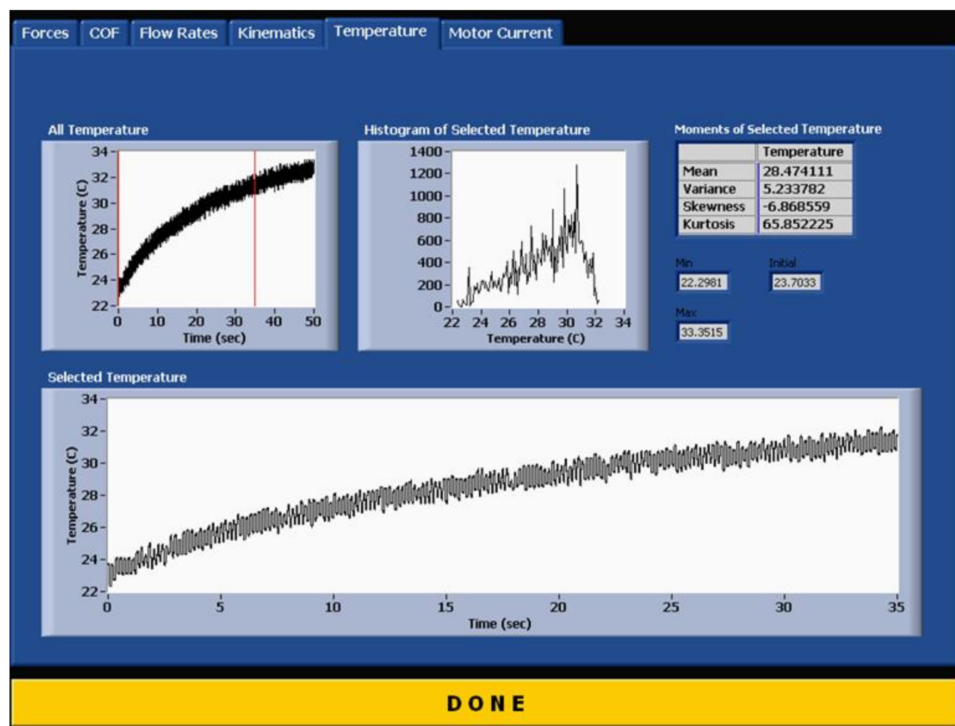

Figure 2.21: Temperature data analysis.

2.1.10 Tool Specifications

The APD-800 and major component specifications are listed in Table 2.4.

Table 2.4: The APD-800 component specifications (APD-800 operations manual).

Manufacturers	Fujikoshi Machinery Corporation and Araca Incorporated
Wafer Size	300-mm (or smaller)
Wafer Carrier	Down force control = Pneumatic Pressure = 0.6 to 8.0 PSI (1.4 to 8.0 PSI for 200-mm) Rotation rate = 15 to 200 RPM
Platen	Φ = 800 mm Rotation rate = 20 to 180 RPM Material = SUS410 Built-in heat exchanger (requires external coolant)
Conditioner	Φ = 108 mm Rotation rate = 12 to 120 RPM Stroke length = 320 mm Sweep velocity = 0 to 500 mm/sec through 10 independently controlled zones Down force = 3.3 to 13.2 lb Scheme = ex-situ or in-situ
Chemical Delivery Systems	Three computer-controlled, 20-liter, chemical-resistant, removable tanks with impeller mixers, roller pumps and level sensors. Flow rate = 10 to 450 cc/min.
Pad Water Rinse	Dedicated high flow rate water rinse injector Flow rate up to 3,000 cc/min
Force Sensors	Shear force (1 sensor) and down force (4 multiplexed sensors)
Temperature Sensor	Adjustable single-point pad surface IR detector
Data Capture vs. Time (capture frequency up to 2,300 Hz; display frequency = 1 Hz)	Platen rotational velocity Carrier rotational velocity Conditioner rotational velocity, position, oscillation speed and motor current Tanks 1, 2 and 3 chemical flow rates Shear force and down force Coefficient of Friction (COF) Pad surface temperature
Basic Data Analysis	Average and variance for the entire (or a subset of the) polishing period for all parameters being captured
Advanced Data Analysis and Correlation	Shear force and down force Fast Fourier Transform (FFT) COF vs. Sommerfeld number COF vs. pad temperature
Control, Monitoring and Analysis	Programmable touch-screen controller for polisher operation Notebook computer for process monitoring and data analysis
W × L × H	100 × 140 × 203 cm (polisher) 80 × 38 × 190 cm (electrical cabinet) 50 × 150 × 81 cm (three chemical delivery systems)
CDA	Minimum pressure = 72 PSI (500,000 Pa) Flow rate = 550 liters per minute
Platen Coolant Water	Maximum pressure = 43 PSI (300,000 Pa) Flow rate = 15 liters per minute

2.2 Analytical Tools

In this dissertation, several analytical tools are used including four-point probe, reflectometer and IR camera. Their general configurations and working principles are described in this section.

2.2.1 Four-point Probe

In this dissertation, film thickness is measured before and after polishing to determine material removal rate and WIWRRNU. The metal film thickness is measured via an Advanced Instrument Technology (AIT) CMT-SR5000 sheet resistance/resistivity measurement system (i.e. four-point probe). Figure 2.22 shows a photograph of the four-point probe used in this study. It is a fully automatic system for measuring sheet resistance and resistivity for 200 and 300 mm wafers. The measurement accuracy is ±0.5% and the measurement repeatability is ±0.15% (AIT CMT-SR5000 sheet resistance/resistivity measurement system operation & service manual).

The working principle of the four-point probe is described as follows (Liao 2014): Four probes, placed along a straight line with equal spacing, contact the top surface of the film. Current (*I*) passes through the outer two probes and the voltage (*V*) between the inner two probes is measured. Assuming the sample is semi-infinite with respect to the probe spacing, based on Maxwell's field equations, the sheet resistance (R_s) can be expressed as (Wolf 2004)

$$R_s = 4.532\frac{V}{I} \qquad \text{Eq. 2.1}$$

The sheet resistance is defined as the resistance in a unit area of the thin film sheet. As such, sheet resistance is divided by resistivity to obtain the film thickness.

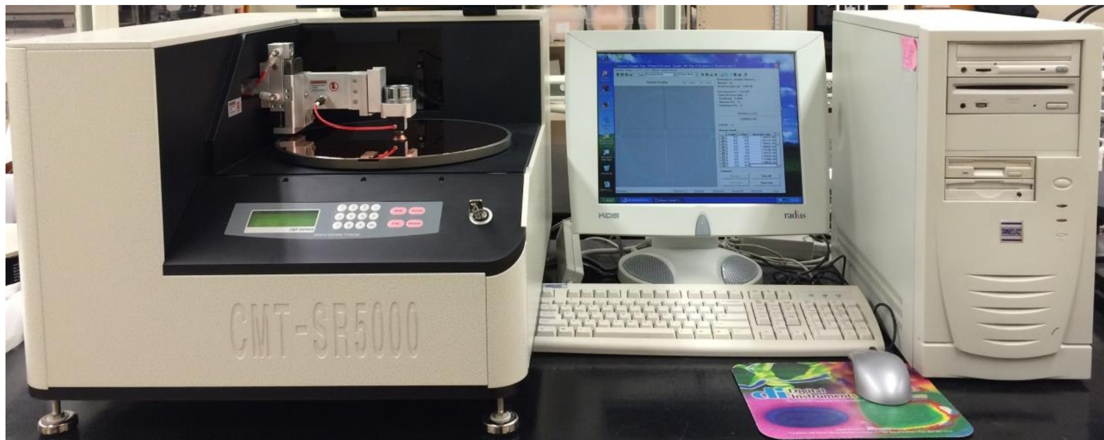

Figure 2.22: AIT CMT-SR5000 sheet resistance/resistivity measurement system.

2.2.2 Reflectometer

In this dissertation, the oxide film thickness is measured via a SENTECH Film Thickness Probe (FTP) reflectometer, which is shown in Figure 2.23. The basic principle of the reflectomter is as follows (Film Thickness Probe FTPadvanced operating manual): The film surface is illuminated by a light beam having a certain range of wavelength. As rays reflected from the top and bottom interfaces of the thin film can be in-phase or out-of-phase, they will interfere either constructively or destructively. As such, a characteristic reflectance spectrum is formed. This spectrum is determined by the film thickness (t), refractive index (n_r) and extinction coefficient (k_e) of the film and the substrate. To determine film thickness, the software calculates a reflectance spectrum theoretically based on initial values of the film properties (i.e. t, n_r, k_e). The software then

varies these parameters until the calculated reflectance spectrum matches the measured one. Therefore, the optimized film thickness is obtained and reported.

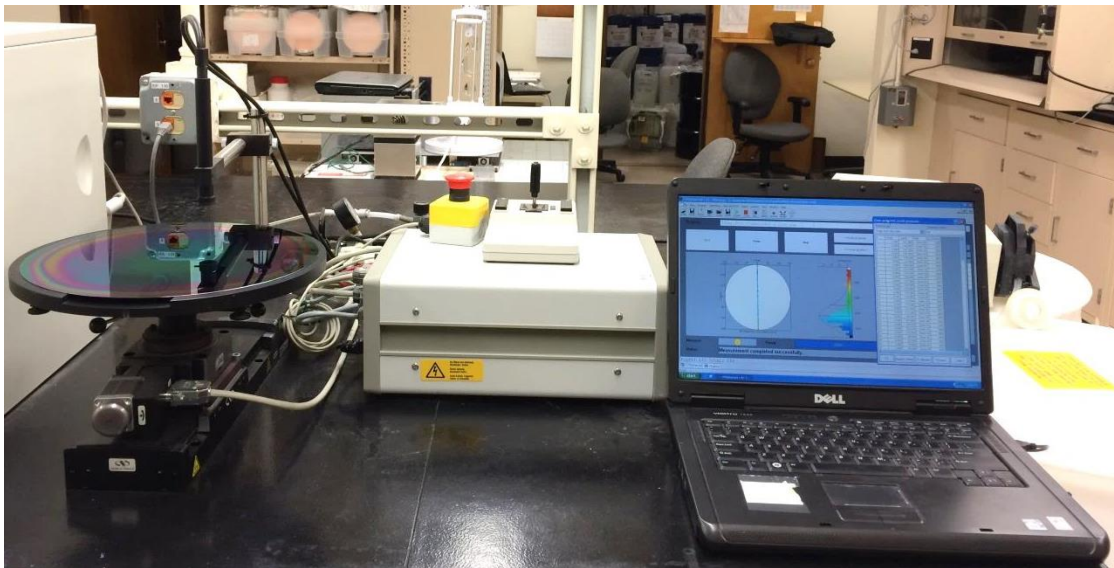

Figure 2.23: SENTECH FTP reflectometer.

2.2.3 IR Camera

As mentioned before, the IR gun of the APD-800 polisher measures the pad surface temperature over a single location. This section will introduce an Agema Thermovision® 550 IR camera, which is capable of capturing the temperature over multiple locations (Jiao 2012).

The Thermovision® 550 measures and images the emitted IR radiation from an object (Thermovision® 550 operating manual). The amount of IR radiation emitted by an object increases with temperature, therefore allowing users to see variations in temperature. The IR camera is calibrated to record temperature measurements. The

measurement accuracy is ± 2 % of range, and the thermal sensitivity is less than 0.1°C (Thermovision® 550 operating manual).

As shown in Figure 2.24, the camera is positioned to image the CMP process. A software (called ThermalCAM Researcher® 2001) is used to control the camera to capture the thermal image (ThermoCAM™ Researcher 2001 Operating Manual). An example of the thermal image is shown in Figure 2.25. In this figure, different colors represent different temperatures and the color bar is shown in the right hand side of the image. Temperatures on the locations of interest can be then extracted from the thermal image. For example, Figure 2.26 shows the pad surface temperatures, on spots SP01 – SP05 in Figure 2.25, as a function of polishing time.

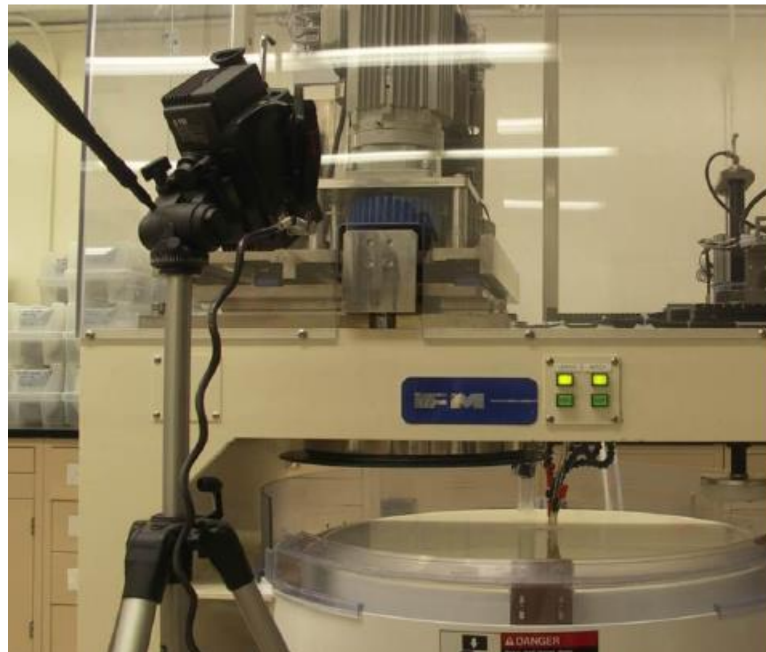

Figure 2.24: The IR camera positioned to the polishing pad (Jiao 2012).

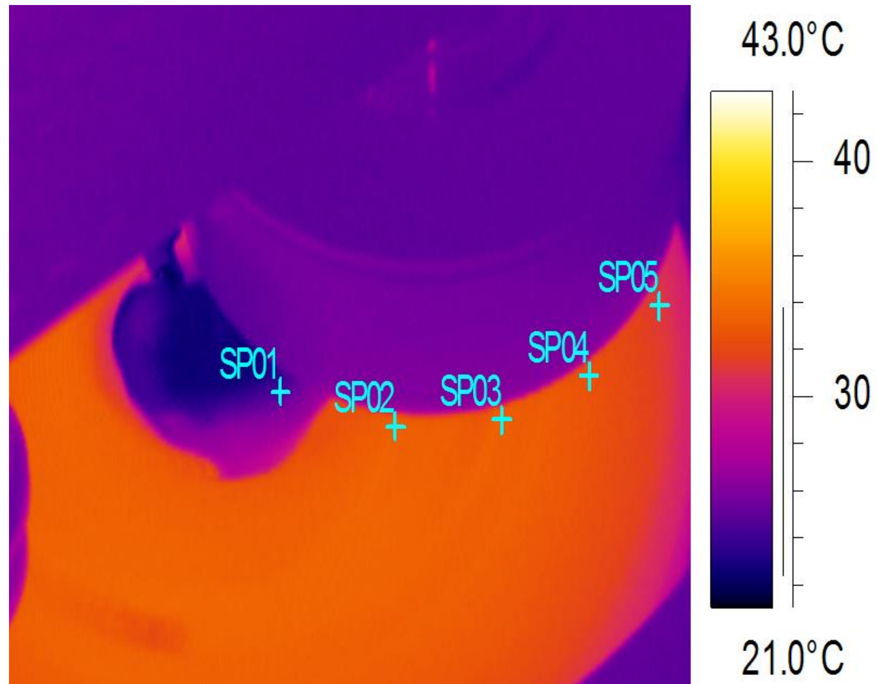

Figure 2.25: An example of the thermal image.

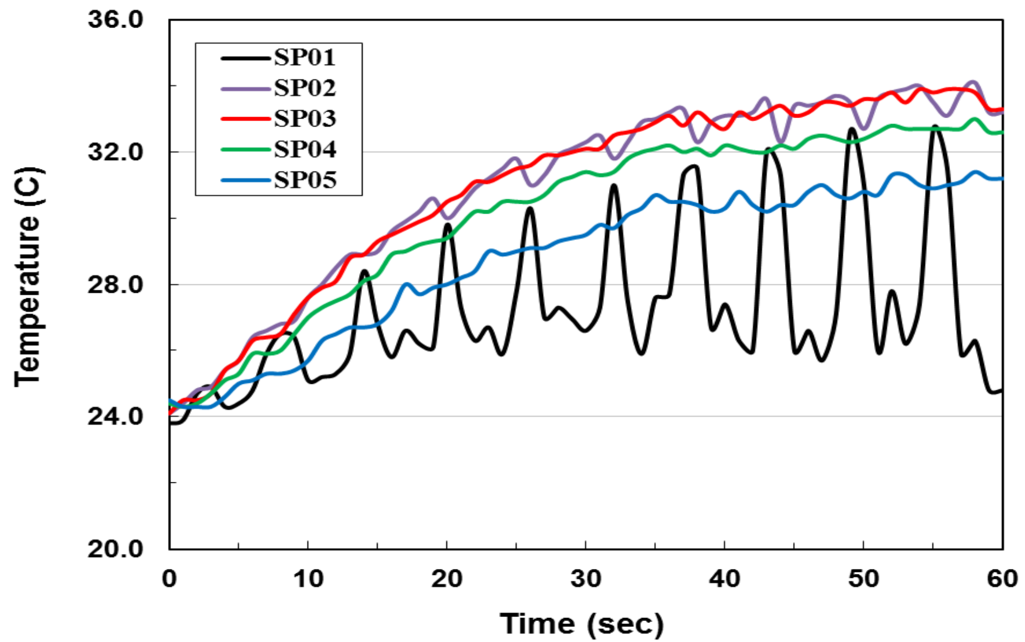

Figure 2.26: Pad surface temperatures as a function of polishing time.

CHAPTER 3

GENERAL THEORY

This Chapter describes the general theory of tribology, material removal mechanisms, and various material removal rate models in CMP.

3.1 Tribology in CMP

Tribology is generally understood as the science and technology of interacting surfaces in relative motion, which includes friction, lubrication, and wear. The field of tribology has existed for many years and played a significant role in CMP (Liang *et al*. 2005).

3.1.1 Friction

Friction is the resistance between bodies which are in contact and are in relative motion. Friction can be generated due to adhesion, ploughing, and deformation (Stolarski 1990). There are three laws of friction. The first law states that the friction force is proportional to the normal load; the second and third laws of friction state that the friction force is independent of the apparent area of contact and the sliding velocity, respectively (Amontons 1699; Coulomb 1785; http://www.tribology-abc.com/abc/history.htm). The proportionality constant between the friction force and normal load is called the coefficient of friction (COF).

During CMP, the wafer is pressed against the polishing pad under a certain pressure. Both wafer and pad rotate in counter clockwise. In addition, slurry containing chemicals and nanoparticles are transported into pad-wafer interface via pad/wafer rotation, pad grooves and the retaining ring. As such, three-body contact (i.e. wafer, pad asperities, and slurry abrasives) occurs in CMP, as shown in Figure 3.1.

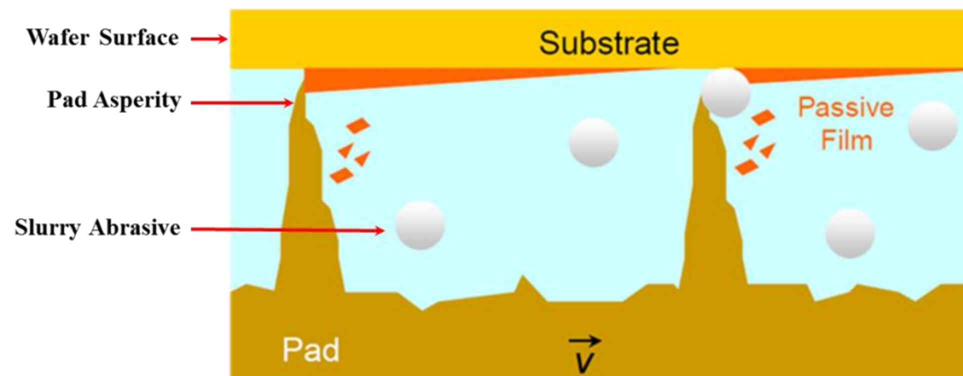

Figure 3.1: Schematic of three-body contact in CMP (DeNardis 2006; Liao 2014).

Shear force (i.e. friction force) is generated between the wafer, pad, and slurry abrasives and can be measured using appropriate instruments. In this dissertation, all polishing tests are performed on the Araca APD-800 polisher and tribometer which is equipped with the force measurement system, as described in Section 2.1.7. The force is measured by load cells which are connected to a computer. The computer synchronizes the force from the load cells to the polishing process so that the real-time shear force and down force data can be obtained (Meled 2011). As an example, Figure 3.2 shows the transient shear force and down force as a function of polishing time.

As mentioned previously, COF is defined as the ratio of the shear force to the down force. Therefore, the transient COF can be expressed as:

$$COF_i = \frac{Shear\ Force_i}{Down\ Force_i} \qquad \text{Eq. 3.1}$$

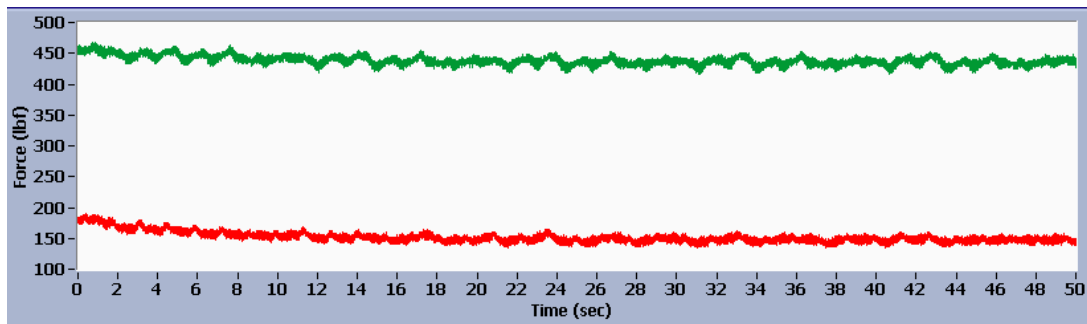

Figure 3.2: The Transient shear force and down force as a function of polishing time.

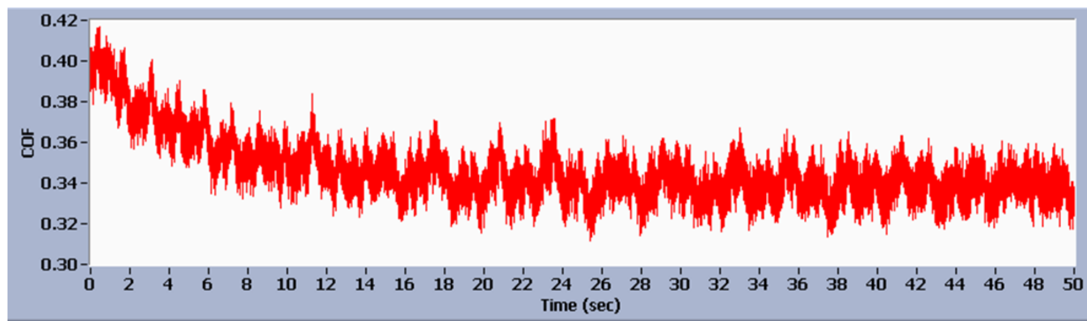

Figure 3.3: Transient COF based on Figure 3.2.

Figure 3.3 shows the transient COF calculated using Eq. 3.1. Based on the transient COF, the average COF can then be calculated via:

$$\overline{COF} = \frac{\sum_{i=1}^{n} COF_i}{n} \qquad \text{Eq. 3.2}$$

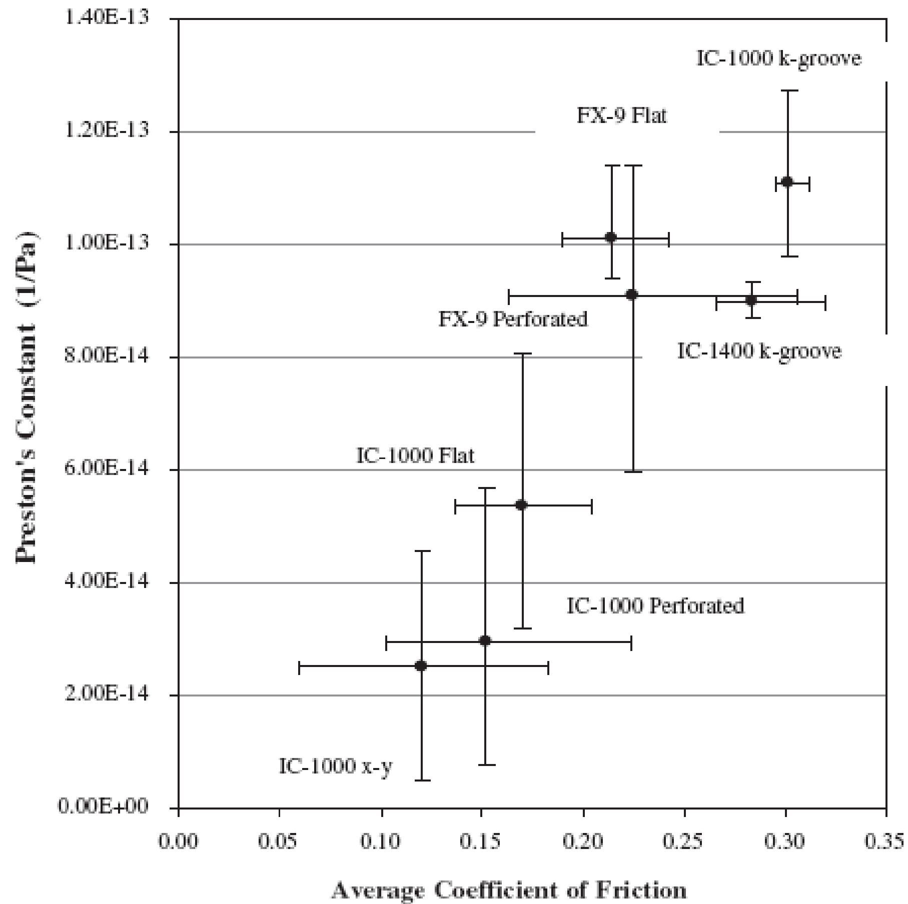

Figure 3.4: Correlation between Preston's constant and average coefficient of friction for different types of pads (Philipossian *et al*. 2003).

COF is a critical parameter for characterizing CMP processes (Philipossian *et al*. 2003). For example, COF in the process of pad seasoning is typically monitored to ensure the stable values are achieved prior to monitor wafer polishing (DeNardis *et al*. 2006).

COF can also be used to estimate the material removal rate during a mechanically-limited process (Philipossian *et al*. 2003; Lee *et al*. 2010). For instance, Figure 3.4 shows that oxide removal rate (i.e. Preston's constant) and average coefficient of friction are linearly related for different types of pads investigated (Philipossian *et al*. 2003). Figure 3.5 shows the correlation between the oxide removal rate and COF for different pad conditioning methods. It is also found that the removal rate increases linearly with COF (Lee *et al*. 2010). As such, oxide removal rate can be estimated from COF based on this linear relationship. In addition, the plot of COF vs. Sommerfeld number is used to determine the lubrication mechanism in CMP, as described in Section 3.1.2.

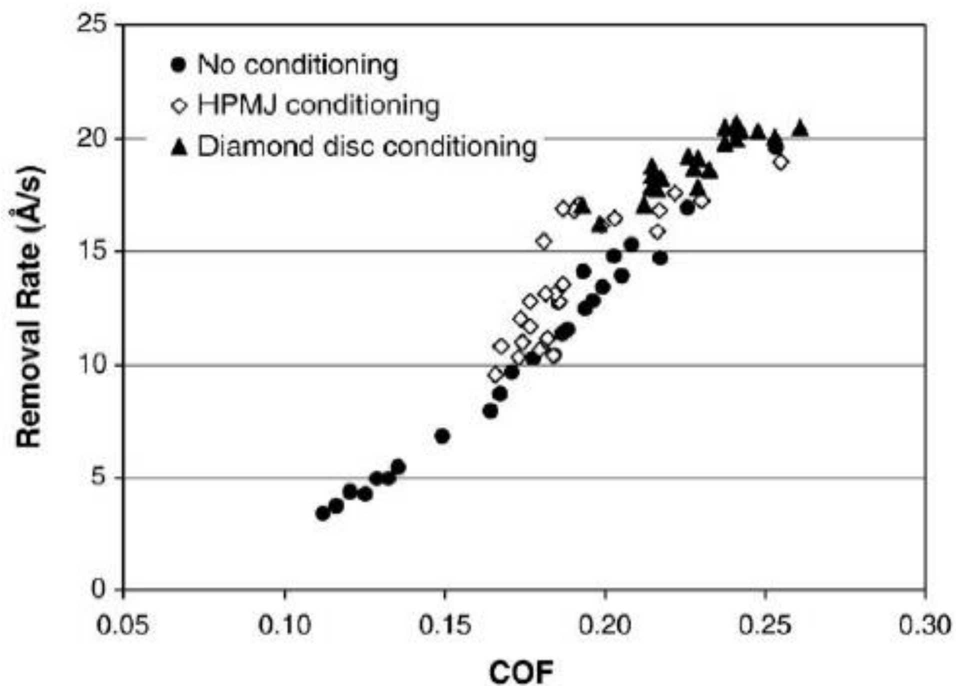

Figure 3.5: Correlation between the oxide removal rate and COF under different pad conditioning methods (Lee *et al*. 2010).

3.1.2 Lubrication Mechanism in CMP

Besides just the friction force, the lubrication mechanism is also a dominant factor for material removal in CMP (Liang *et al*. 2005). The lubrication mechanism in CMP processes can be determined by the Stribeck curve, which is constructed by plotting COF as a function of Sommerfeld number (So). So is a dimensionless parameter and expressed as (Philipossian *et al*. 2003):

$$So = \frac{\mu U}{p\delta_{eff}} \qquad \text{Eq. 3.3}$$

where μ is the slurry viscosity, U is the pad-wafer sliding velocity, p is the wafer pressure, and δ_{eff} is the effective slurry film thickness at the wafer and pad interface. A brief description of calculating So is summarized below while a more detailed description can be found elsewhere (Philipossian *et al*. 2003).

Slurry viscosity μ can be measured experimentally for a given slurry at a given range of shear rates. The pad-wafer sliding velocity U can be calculated based on the tool geometry and the relative angular velocity of the wafer and platen (Philipossian *et al*. 2003).

The wafer pressure p is the applied down force divided by the contact area between the wafer and the pad. It should be noted that the pad land area under the wafer could be different for pads with different groove types. A dimensionless parameter, α , is

introduced to describe the percent land area for a given type of pad (Philipossian *et al*. 2003). α can be expressed as:

$$\alpha = \frac{A_{land-area}}{A_{flat}} \qquad \text{Eq. 3.4}$$

As the percent land area is different, each pad may experience a different pressure when the same down force is applied on the wafer. As such, the actual pressure in Eq. 3.3 should be the product of the term $1/\alpha$ and the applied pressure.

Figure 3.6 shows the values of α and the actual pressure for pads with different groove types. The values of α for the flat, k, perforated, and xy groove pads are 1, 0.83, 0.91, and 0.76, respectively. Accordingly, the actual pressure is 1, 1.2, 1.1, and 1.3 times of the applied pressure (Philipossian *et al*. 2003).

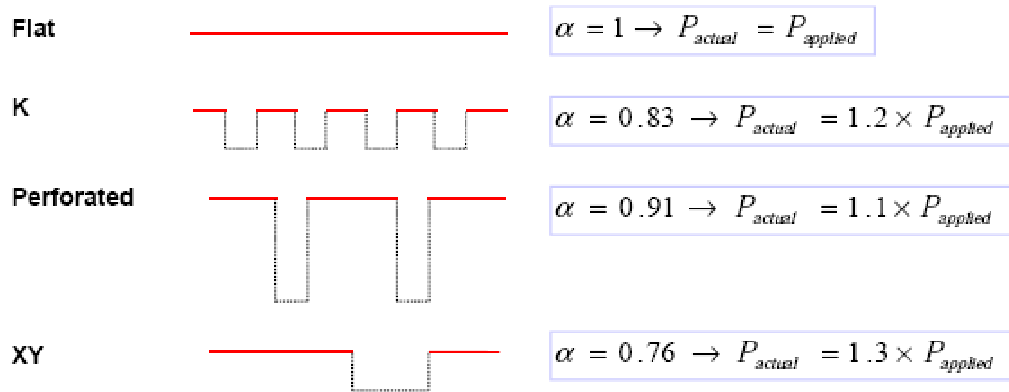

Figure 3.6: Calculation for α and the actual pressure (Philipossian *et al*. 2003).

It is harder to obtain the effective slurry film thickness δ_{eff}. Lu *et al*. and Rogers *et al*. employed the DELIF (i.e. dual emission laser introduced fluorescence) method to measure the slurry film thickness on flat pads (Lu *et al*. 2000; Rogers *et al*. 1998). In addition, Lawing assumed that the slurry film thickness was approximately equal to the arithmetic average roughness of the pad (Lawing 2002). Based on Lawing's assumption, Philipossian *et al*. proposed a new method of calculating the slurry film thickness (Philipossian *et al*. 2003). This method accounts for the additional slurry retained inside pad grooves.

$$\delta_{eff} = \alpha \times R_a + (1-\alpha) \times \delta_{groove} \qquad \text{Eq. 3.5}$$

where R_a is the arithmetic average roughness of the pad. R_a can be measured experimentally using a surface profiler. δ_{groove} is the groove or perforation depth, which can be physically measured. α is the percent land area as described previously (Philipossian *et al*. 2003).

After μ, U, p, and δ_{eff} are obtained, So is fully determined as indicated by Eq. 3.3. In addition, Section 3.1.1 has described how to calculate COF. As such, the Stribeck curve can be constructed by plotting COF vs. So.

Figure 3.7 shows a generic Stribeck curve (Philipossian *et al*. 2003). As evident from Figure 3.7, there are three contact modes: boundary lubrication, partial lubrication, and hydro-dynamic lubrication. Boundary lubrication occurs at smaller values of the

Sommerfeld number. In this regime, the slurry film thickness is small. The wafer, pad, and slurry abrasives are in intimate contact with one another (Philipossian *et al*. 2003). As such, COF is high and independent of the sommerfeld number. From a process control point-of-view, boundary lubrication is preferable because of its high and stable COF (Liao 2014). As it turns out, boundary lubrication is the dominant in most CMP processes (Liang *et al*. 2005).

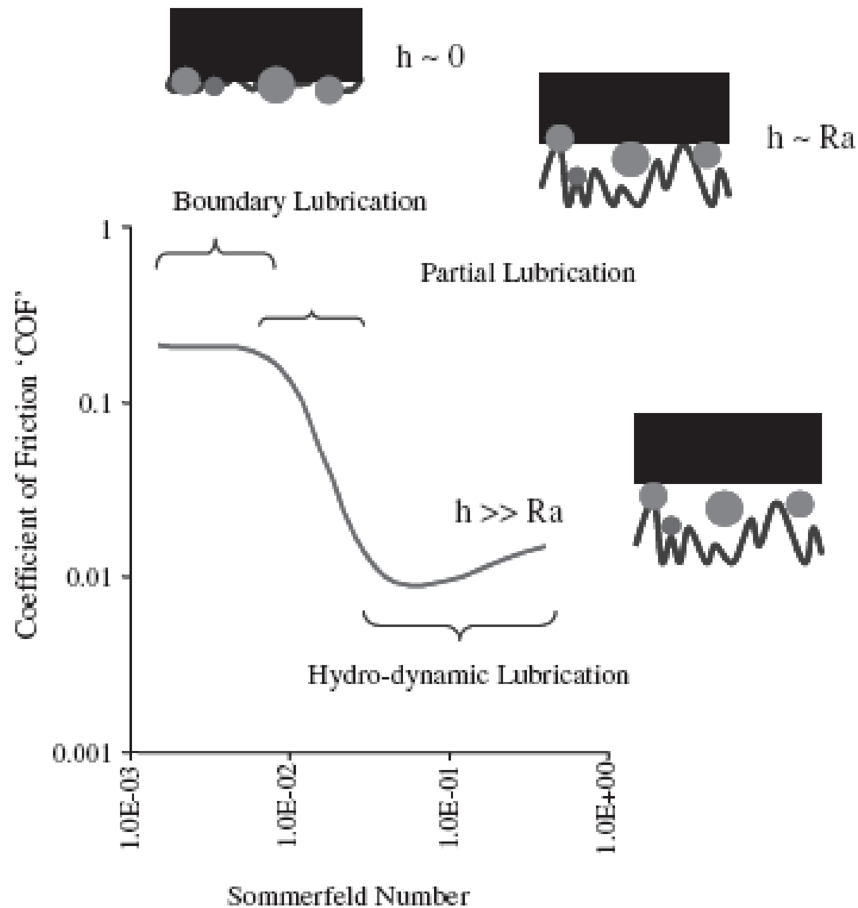

Figure 3.7: Generic Stribeck curve based on Sommerfeld number (Philipossian *et al*. 2003).

The second mode of contact is partial lubrication (also called mixed lubrication), which occurs at intermediate values of the Sommerfeld number. In this regime, the slurry film thickness is similar to that of the roughness of the pad (Philipossian *et al*. 2003). As such, the slurry film layer partially separates the wafer and the pad. In addition, COF dramatically decreases as increase in the Sommerfeld number. From a process control point-of-view, partial lubrication is not preferable because of its unstable COF (Liao 2014). In this regime, a small change in process parameter such as polishing pressure and velocity may cause a significant change in COF.

The last mode of contact is hydro-dynamic lubrication, which occurs at larger values of the Sommerfeld number. In this regime, the slurry film thickness is significantly larger than that of the roughness of the pad (Philipossian *et al*. 2003). As such, very little contact exists between the wafer and pad, resulting in a smaller COF. There are no reports that CMP processes run in this regime (Liang *et al*. 2002; Liang *et al*. 2005).

3.1.3 Wear in CMP

Wear plays a significant role in CMP. Wear mechanisms associated with CMP processes include adhesive wear, abrasive wear, tribochemical wear, electrochemical wear, and fatigue wear (Liang *et al*. 2005). Wear at the wafer surface is evaluated as the material removal rate (Liang *et al*. 2005). Section 3.2 will describe the material removal mechanism in CMP.

Besides wafer material removal, there have been a few studies on the pad wear during CMP. For example, Jiao *et al*. investigated the pad wear during ILD CMP. It was found that the polyether ether ketone (PEEK) retaining ring generated a significantly lower pad wear rate (by 31%) than the polyphenylene sulfide (PPS) retaining ring. In addition, the thermoplastic D100 pad exhibited lower pad wear rates than the thermoset IC1000 pad (Jiao *et al*. 2012). Meled investigated the effect of slurry abrasives on pad wear rate in STI CMP. A comparison between the fumed and colloidal abrasives at the same abrasive concentration showed that the colloidal slurry generated a higher pad wear rate compared to the fumed slurry. In addition, a comparison between the fumed and colloidal slurries at the same abrasive content showed that the fumed slurry generated a higher pad wear rate compared to the colloidal slurry (Meled *et al*. 2010).

There have been also a few studies on diamond disk wear during CMP. For example, Liao found that peripheral diamonds and the diamonds that originally protrude higher with crest lines oriented upward wear faster (Liao 2008). Borucki *et al.* demonstrated that the top 10 to 20 aggressive diamonds did the majority of the cutting and were therefore most susceptible to fracture or pull-out (Borucki *et al*. 2007; Borucki *et al*. 2008). Meled *et al.* conducted 24-hour wear tests and showed the presence of micro-wear on the aggressive diamonds but no appreciable wear on the inactive diamonds (Meled *et al*. 2010). Chapter 6 of this dissertation will repost on aggressive diamond characterization and wear analysis during CMP.

3.2 Material Removal Mechanisms in CMP

The Kaufman theory is widely used to describe material removal in CMP (Kaufman *et al*. 1991). Chemicals in the slurry react with wafer surface to form a passive film, which is then removed by mechanical forces through the actions of pad asperities and slurry abrasive nanoparticles, as shown in Figure 3.1. This two-step process is then repeated until the end of the CMP processes (Kaufman *et al*. 1991; Thakurta *al*. 2002; Borucki *et al*. 2004).

Cook and Tomozawa proposed the likely mechanism of oxide CMP (Cook 1990; Tomozawa 1997) where water molecules break the silicon and oxygen bonds of silica to form hydroxyl-terminated silicon bonds. Compressive forces and tensile loading then produce a net dissolution of silica in the form of $Si(OH)_4$. The so-called snow ball removal mechanism is currently practiced by the industry when the silica slurry abrasives are used in oxide CMP. This mechanism states that adhesion between the constantly hydrated wafer surface and the surface of hydrated silica abrasives leads to surface material removal, in a snowball effect (Liang *et al*. 2005; Holland 1964).

The mechanisms involved in metal CMP are complex. In general, the oxidation state of the metal is enhanced via oxidizers during metal CMP. For example, Hernandez *et al*. performed surface chemistry studies of Cu CMP. Blanket copper samples were polished using an acidic slurry which contains alumina abrasive particles and hydrogen peroxide. Surface studies were performed on the copper samples after chemical etching or CMP. The etching results showed the presence of Cu_2O on the etched sample surface while polished samples showed CuO and $Cu(OH)_2$ (Hernandez *et al*. 2001). For W CMP,

the passivation of W was first proposed by Kaufman *et al*. in 1991(Kaufman *et al*. 1991). In their study, W film was polished with a mixture of ferricyanide-phosphate in the presence of free abrasive particles. They proposed that a blanket passivating layer (i.e. WO_3) was formed on the surface of the tungsten due to the oxidizing nature of the slurry. Mechanical abrasion from the slurry abrasives and the polishing pad subsequently removes the passivating layer (Kaufman *et al*. 1991). The passivation reaction was proposed as (Kaufman *et al*. 1991):

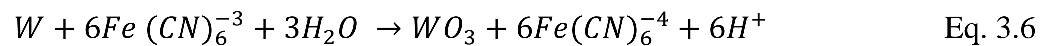

$$W + 6Fe\,(CN)_6^{-3} + 3H_2O \rightarrow WO_3 + 6Fe(CN)_6^{-4} + 6H^+ \qquad \text{Eq. 3.6}$$

3.3 Various Removal Rate Models in CMP

3.3.1 Preston's Equation

To date, various removal rate models have been proposed. One of the most famous and original models is the Preston's equation. Preston developed this empirical removal rate model in 1927 based on glass polishing. Preston's equation, shown in Eq. 3.7, states that removal rate is proportional to the product of the polishing pressure, *p*, and pad-wafer sliding velocity, *U* (Preston 1927):

$$RR = k \cdot p \cdot U \qquad \text{Eq. 3.7}$$

where *RR* is the material removal rate, *k* is Preston's constant, *p* is the polishing pressure, and *U* is the pad-wafer sliding velocity.

If the removal rate of a CMP process obeys the Preston's equation, we can claim that this process exhibits Prestonian behavior. As a matter of fact, Prestonian behavior is commonly observed in many processes. For example, Philipossian *et al*. found that ILD removal exhibited Prestonian behavior, as shown in Figure 3.8 (Philipossian *et al*. 2003).

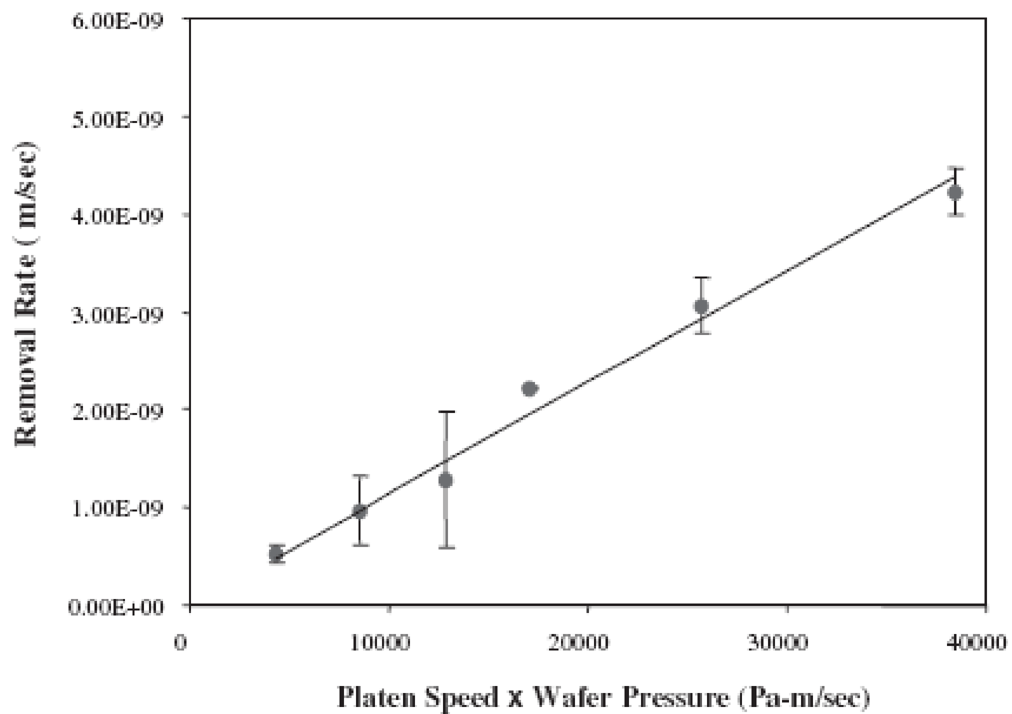

Figure 3.8: Prestonian removal rate model for ILD CMP (Philipossian *et al*. 2003).

3.3.2 Modifications of Preston's Equation

Prestonian behavior is commonly found in many processes, but non-prestonian behavior is also widely observed. To capture the non-prestonian behavior, many

modifications of Preston's equation were proposed (Sorooshian *et al*. 2005). For example, Zhang *et al*. and Tseng *et al*. proposed removal rate models as shown in Eq. 3.8 and Eq. 3.9, respectively (Zhang *et al*. 1998; Tseng *et al*. 1997).

$$RR = k \cdot (pV)^{1/2} \qquad \text{Eq. 3.8}$$

$$RR = k \cdot p^{5/6} \cdot V^{1/2} \qquad \text{Eq. 3.9}$$

The above models can capture the non-prestonian behavior to some extent (Sorooshian *et al*. 2005). However, it should be noted that Preston's equation and modifications of Preston's equation mainly consider the mechanical attributes of CMP processes. However, as described in Section 3.2, material removal is achieved through combined chemical and mechanical actions. In order to model material removal more accurately, it is necessary to develop removal rate models that combine chemical and mechanical attributes. A Langmuir-Hinselwood model described in Section 3.3.3 is a representing model of this type.

3.3.3 Langmuir-Hinselwood Removal Rate Model

Borucki *et al*. proposed a two-step modified Langmuir-Hinselwood model (Borucki *et al*. 2004; Sorooshian *et al*. 2005; Li 2008) based on the model originally developed by Thakurta *et al*. (Thakurta *et al*. 2002). The model is summarized as follows (Source: Borucki *et al*. 2004; Sorooshian *et al*. 2005; Li 2008; Jiao *et al*. 2011).

The model assumes that n moles of reactant R in the slurry react with surface film (S) on the wafer at a chemical rate constant k_1 to form a product layer $\underline{L}$,

$$S + nR \xrightarrow{k_1} \underline{L} \qquad \text{Eq. 3.10}$$

This product layer is then removed by mechanical abrasion with a mechanical rate constant k_2,

$$\underline{L} \xrightarrow{k_2} L \qquad \text{Eq. 3.11}$$

The abraded material L is assumed to be carried away by the slurry and not re-deposited on the wafer surface. Assuming that the rate of the formation of the surface layer is equal to that of its depletion, the local removal rate in this sequential mechanism is

$$RR = \frac{M_w}{\rho} \frac{k_1 k_2 C}{k_1 + k_2} \qquad \text{Eq. 3.12}$$

where M_w is the molecular weight, ρ is density and C is the local molar concentration of the reactant. To simplify the model, it is assumed that there is no or little reactant depletion so that C remains constant. This allows C to be absorbed into k_1 and its value is set to be unity as (Li 2008):

$$RR = \frac{M_w}{\rho} \frac{k_1 k_2}{k_1 + k_2}$$ Eq. 3.13

The chemical rate constant k_1 can be expressed as Arrhenius equation:

$$k_1 = A \exp(-E / k_b T)$$ Eq. 3.14

where A is an exponential factor, E is the slurry activation energy, k_b is a constant (8.62×10^{-5} eV/K), and T is the wafer surface reaction temperature.

The mechanical rate constant k_2 is considered to be proportional to the frictional power density as suggested in Preston's equation (Meled 2011):

$$k_2 = c_p \mu_k pV$$ Eq. 3.15

where c_p is a proportionality constant and μ_k is COF.

In order to calculate the wafer surface reaction temperature T in Eq. 3.14, Borucki *et al*. proposed a flash heating thermal model (Borucki *et al*. 2005; Li 2008). Assuming the chemical reaction is determined by transient flash heating, the wafer surface reaction temperature can be expressed as the summation of the mean pad surface temperature T_p and a term called wafer surface reaction temperature increment (Borucki *et al*. 2005; Li 2008):

$$T = T_p + \frac{\beta}{V^{1/2+e}} \mu_k p V \qquad \text{Eq. 3.16}$$

where β and e are fitting parameters.

The two-step modified Langmuir-Hinselwood model is summarized from Eq. 3.13 to Eq. 3.16. There are five fitting parameters in the model: E, A, c_p, β, and e. The slurry activation energy (E) can be calculated from a plot of the natural log of the removal rate verse the inverse of the mean pad temperature assuming an Arrhenius relationship (Sorooshian *et al*. 2004). As an example, Figures 3.9 and 3.10 show how to extract E in Cu CMP and STI CMP, respectively, using this method. The extracted E is 0.826 and 1.097 eV, respectively.

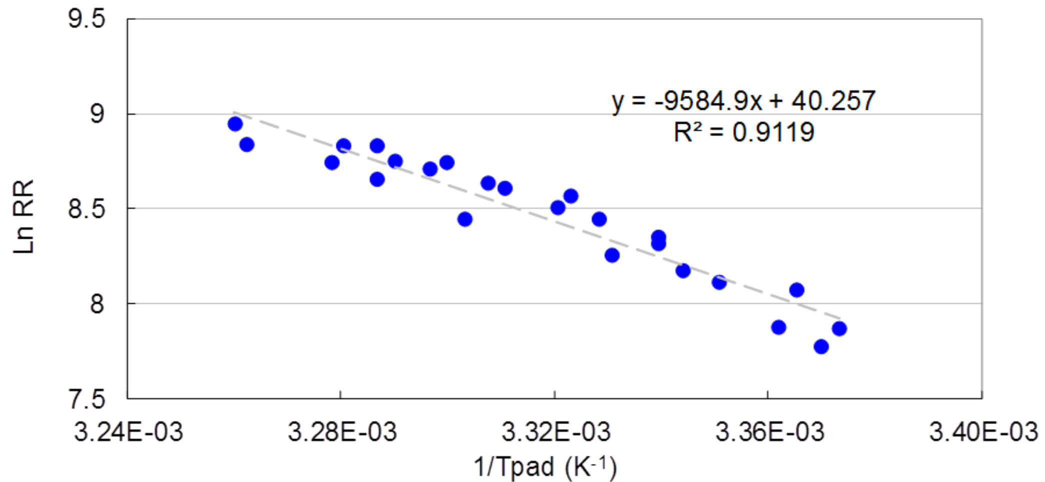

Figure 3.9: Arrhenius relationship between the copper removal rate and mean pad surface temperature.

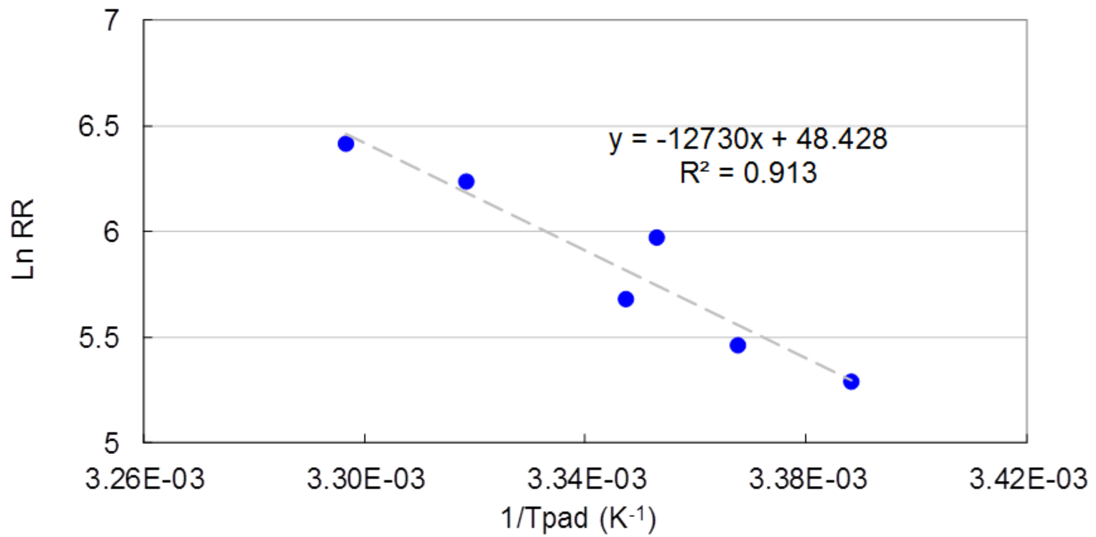

Figure 3.10: Arrhenius relationship between the oxide removal rate and mean pad surface temperature.

During simulation, parameters A, C_p, β, and e are optimized to minimize the square of the error associated with the experimental and simulated values of the removal rates (Jiao *et al*. 2011). This model agrees well with experimental results during ILD and metal CMP (Sorooshian *et al*. 2005; Jiao *et al*. 2011; Jiao *et al*. 2012).

Based on this model, it is apparent that material removal rate in CMP is a function of both chemical and mechanical attributes as indicated by Eq. 3.12. As such, material removal rate can be adjusted by either changing the mechanical parameters (e.g. polishing pressure and velocity) or by changing the chemical parameters (e.g. pad surface temperature). Chapter 4 of this dissertation will show the feasibility of adopting a new method to improve WIWRRNU during copper CMP that is solely based on intentional local temperature manipulation of the pad.

CHAPTER 4

PAD SURFACE THERMAL MANAGEMENT DURING COPPER CHEMICAL MECHANICAL PLANARIZATION

A pad surface thermal management system was developed to improve copper removal rate within wafer non-uniformity by locally adjusting the pad surface temperature. The system consisted of one or more thermal transfer modules, which contacted the pad surface during polishing. Hot or cold water circulated between the thermal transfer module and an external heater or cooler. With the module placed on the pad surface, heat conduction occurred between the module and the pad surface, producing a localized pad surface with higher or lower temperatures. As such, it was expected that local removal rates would change accordingly due to the temperature-sensitive nature of copper chemical mechanical planarization (CMP). In this study, the system was used to adjust the "center-fast" removal rate profile to illustrate its effect during the process. Results showed that, when two thermal transfer modules were employed, local removal rates in the wafer center region decreased significantly while the removal rates near the wafer edge were maintained thereby significantly improving within wafer removal rate non-uniformity.

4.1 Introduction

CMP has been widely used to planarize copper dual damascene structures in the integrated circuit (IC) manufacturing through combined chemical and mechanical means

(Jiao *et al*. 2011; Liao *et al*. 2011; Fan *et al*. 2010; Fan 2012; Zantye *et al*. 2004; Li 2008; Oliver 2004). CMP performance is characterized by some parameters such as removal rate, within wafer removal rate non-uniformity (WIWRRNU), step height reduction efficiency, and defect density (Sun *et al*. 2010; Paik *et al*. 2009).

WIWRRNU is a critical parameter to determine film thickness planarity on a global (i.e. wafer-scale) level. This is essential for the dimensional accuracy required for the subsequent photolithographic processes (Fu *et al*. 2001). For copper CMP, it has been widely observed that material removal rate across the wafer is non-uniform (Meled 2011; Lee *et al*. 2008; Lee *et al*. 2009; Lee *et al*. 2010; Stavreva *et al*. 1995). The variation in material removal rate across wafer surface impacts WIWRRNU and resolving this issue continues to be an area of intense focus in the industry.

As such, several methods have been proposed to improve WIWRRNU during CMP. Mau proposed a face-up polisher, allowing the pad to move from the wafer center region to its edge region to improve WIWRRNU (Mau 2008). Shendon invented a soft backed wafer carrier head to improve WIWRRNU (Shendon 2000). In addition, much work has focused on the application of the multi-zone wafer carrier head (Wang *et al*. 2011; Wang *et al*. 2008; Chen *et al*. 2008; Kajiwara *et al*. 2003; Chen 2004). For instance, Wang *et al*. proposed a multi-chambered carrier head, which is capable of applying different polishing pressures across the wafer surface to achieve an improved WIWRRNU (Wang *et al*. 2011). Kajiwara *et al*. and Chen also invented similar multi-zone carrier heads (Kajiwara *et al*. 2003; Chen 2004).

While the above methods help improve WIWRRNU, they are quite costly (often times comprising more than 10 percent of the original capital expense of the entire polisher) and require the introduction of a new generation of polisher or costly retrofitting of the existing polisher.

The objective of this study is to show the feasibility of adopting a new, and much more economical, method to improve WIWRRNU during copper CMP that is solely based on intentional local temperature manipulation of the pad. In this paper, this alternative approach is referred to as pad thermal management, or PTM.

4. 2 The PTM System

Previous studies have shown that copper removal rate is highly sensitive to the pad surface temperature during a chemically-limited CMP process (Sorooshian *et al*. 2003; Renteln *et al*. 1999; Li *et al*. 2005). For example, assuming a chemical removal rate that is Arrhenius in nature, given a slurry activation energy of 1 eV, a 10 °C change in the pad surface temperature can easily double copper removal rate (Li *et al*. 2005). Higher pad surface temperatures lead to hotter polished substrates. This causes enhanced oxidation reactions on the substrate surface and therefore a higher copper removal rate (Sampurno *et al*. 2005). Because of this temperature sensitivity, it is possible to locally, and intentionally, adjust copper removal rate to improve WIWRRNU by locally adjusting the pad surface temperature.

Figure 4.1 schematically shows the top view of a polisher with the PTM system. The system consists of one or more non-rotating thermal transfer modules which may be

lined up along a holding bar and placed on the pad surface. The bottom side of each thermal transfer module incorporates a heat transfer disk made of silicon carbide as shown in Figure 4.2. Silicon carbide is selected as the material of choice for its high thermal conductivity (Borucki *et al*. 2011), its wear resistance, its purity and its current acceptability and adoption in CMP as the premier substrate material for high-end CVD diamond disks which also happen to contact the pad surface during the process.

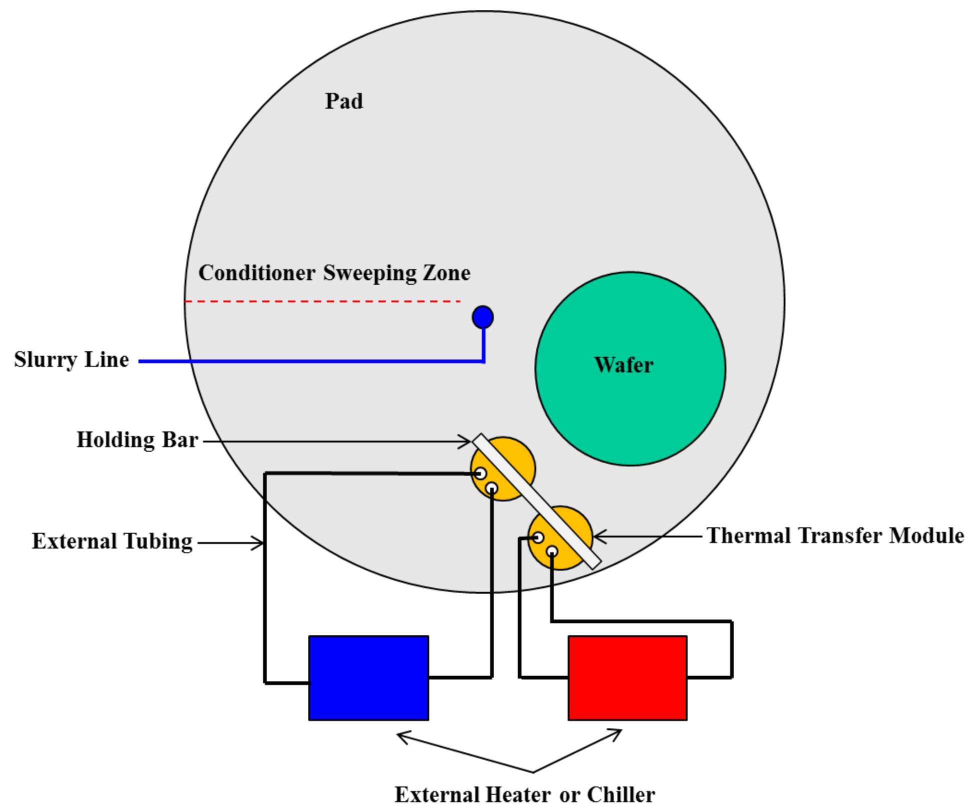

Figure 4.1: Schematic of the top view of a polisher with the PTM system. Both pad and wafer are rotating in a counter-clockwise fashion.

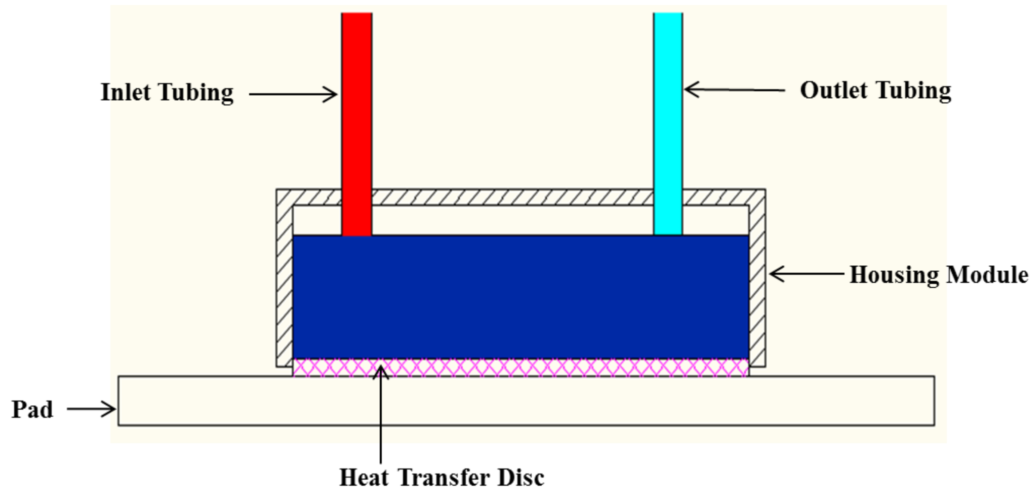

Figure 4.2: Schematic of the thermal transfer module and water circulation.

The heat transfer disk (with a diameter of 50 mm) is completely sealed along its periphery as well as its upper region by a housing module made of an acetal resin. The inner space of the housing is designed to be large enough to act as a reservoir allowing hot or cold water (from an external heater or chiller) to be brought in and out of the system via external tubing thus acting as an energy source, or sink, during the process.

On a rotary polisher, due to pad rotation, an annular pad surface region with higher or lower temperatures can be produced with the PTM (Borucki *et al*. 2011). Heat exchange takes place in a continuous fashion as water enters and exits through the outlet tubing and returns to the external heater or chiller. The PTM is designed such that the location of the thermal transfer module relative to the pad center is adjustable (Borucki *et al*. 2011). In addition, it should be noted that these modules are placed on the pad surface near the leading edge of the wafer carrier head, which allows local heating or cooling of the pad surface just before it comes into contact with the wafer surface. It should be also

noted that no built-in chiller is used to directly heat or cool the platen during polishing in this study.

4.3 Experimental

200-mm blanket copper wafers were polished on an Araca APD-800 polisher and tribometer equipped with the unique ability to acquire real-time shear force and down force during polishing (Liao 2014; Wu *et al*. 2013; Sun 2009). A 3M A2810 diamond disk was used to condition a 32-inch IC1000 K-groove pad during wafer polishing at a conditioning down-force of 44.5 N. Each wafer was polished for 1 minute at 10.3 kPa and 1.0 m/s. Prior to wafer polishing, the diamond disk was used to break in the pad for 30 min with deionized (DI) water. The diamond disk rotated at 95 RPM and swept at a frequency of 10 per minute across the radius of the pad surface. Pad break-in was followed by pad seasoning during which the shear force was monitored to ensure that stable values were achieved prior to monitor wafer polishing (Liao *et al*. 2013).

The slurry, dispersed at 300 ml/min, consisted of 7 volume parts of Hitachi Chemical HS-2H-635-12 slurry, 7 volume parts of DI water and 6 volume parts of 30% ultra-pure hydrogen peroxide.

Two blanket monitor copper wafers were polished with and without the PTM system, respectively. Local copper removal rates were determined by the thickness of the copper film measured before and after polishing using a four-point probe. Two perpendicular diameter scans containing 98 points were performed to measure the thickness of the copper film across the wafer surface. The mean values of these two lines

were reported as a function of the distance from wafer center. In addition, during wafer polishing, the pad surface temperature was measured in real-time with a 1 Hz acquisition frequency using a FLIR infrared video camera. A customized computer program was then used to extract values of temperature from the thermal images (Sampurno *et al*. 2005; Jiao *et al*. 2012).

4.4 Results and Discussion

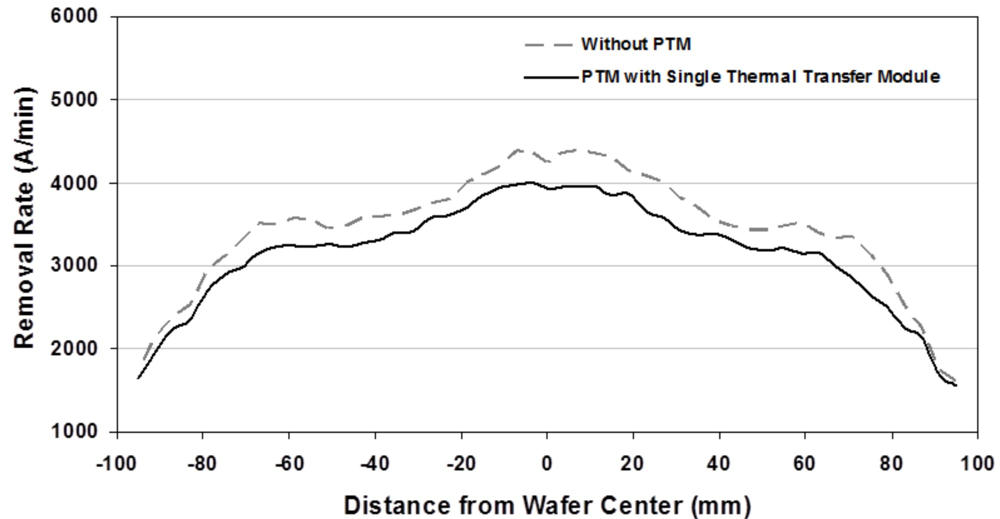

Figure 4.3: Removal rate profile comparison with and without the single thermal transfer module.

In Figure 4.3, the grey dashed line shows the removal rate profile as a function of distance from the wafer center where the PTM system is not installed on the polisher. Conditions having to do with this particular process are selected such that a gross “center-fast” removal rate profile is attained whereby the wafer center region (i.e. from -50 to

+50 mm) is polished faster than the wafer edge regions thus resulting in a high WIWRRNU.

In the case of the "center-fast" removal process, properly reducing the local removal rates at the wafer center region will help improve WIWRRNU. As such, the PTM system is employed to reduce the local removal rates on the wafer center region by lowering temperature of the pad surface that corresponds to that location.

First, the PTM system with a single thermal transfer module is tested. Figure 4.4 schematically shows the position of the module, which is placed on the pad surface such that the center of its heat transfer disk (incorporated at the bottom of the module, see Figure 4.2) corresponds to the center track of the wafer. An external chiller connects to the thermal transfer module and introduces cooled water with a constant temperature of 2 ^{0}C.

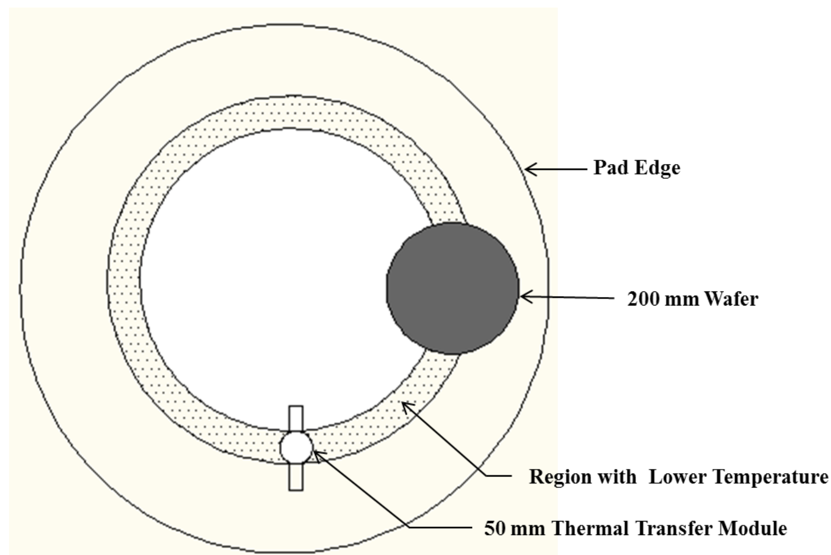

Figure 4.4: Position of the single thermal transfer module on the pad surface. Both pad and wafer are rotating in a counter-clockwise fashion.

Figure 4.5(a) shows the thermal image of the pad surface with the single thermal transfer module. Different colors represent different pad surface temperatures. The color bar is shown on the right hand side of Figure 4.5(a). As evident from Figure 4.5(a), an annular pad surface region with lower temperature is produced by the thermal transfer module. The point "SP01" is in the region where the module makes contact. The other three spots (i.e. "SP02" through "SP04") are outside of this region towards the edge of the pad, but they are still located inside the wafer edge track, as shown in Figure 4.5(b).

It should be noted that the thermal image around the module as shown in Figure 4.5 (a) is not directly affected by the freshly injected slurry as it does not flow directly to the heat transfer module region. As shown in Figure 4.1, due to the counter-clockwise rotation of the platen and the polishing head, most of the freshly injected slurry flows directly to the leading edge of the polishing head. The freshly injected slurry immediately affects the polishing process and the pad temperature in the wafer-pad polishing region. After passing the polishing region, the pad surface of the wafer track retains a thin layer of used slurry. Therefore, the thermal images (i.e. captured around the heat transfer modules located on the wafer track near the leading edge of the polishing head) essentially represent the temperatures of the pad surface with very thin used slurry film before it enters the polishing region.

The pad surface temperatures at these four spots (i.e. "SP01" through "SP04") are extracted and summarized as a function of polish time as shown in Figure 4.6(a). As expected, "SP01" has significantly lower pad surface temperatures than those of the other three spots. For comparison, Figure 4.6(b) summarizes the pad surface temperatures on

these same four spots as a function of polish time when the PTM system is not installed on the polisher. By comparing Figure 4.6(a) with Figure 4.6(b), one can summarize that "SP02" through "SP04" have similar temperatures with and without the PTM system while the temperature associated with "SP01" is significantly lower (on average, by 3.2 ℃) when the PTM system is used. It is therefore expected that the local removal rates near the wafer center region will be reduced.

Figures 4.6(a) and 4.6(b) show an initial decrease in pad surface temperature, followed by a gradual rise in temperature afterwards regardless whether the PTM system is installed or not. As the body of the pad/platen retains heat generated from the previous polishing runs, the initial pad surface temperature is higher than the temperature of the fresh slurry. As such, when the fresh slurry is applied on the pad to polish the next wafer, it cools down the pad surface globally during the initial 10 to 15 sec polishing. Afterwards, as more frictional heat is generated, the pad temperature shows an increasing trend.

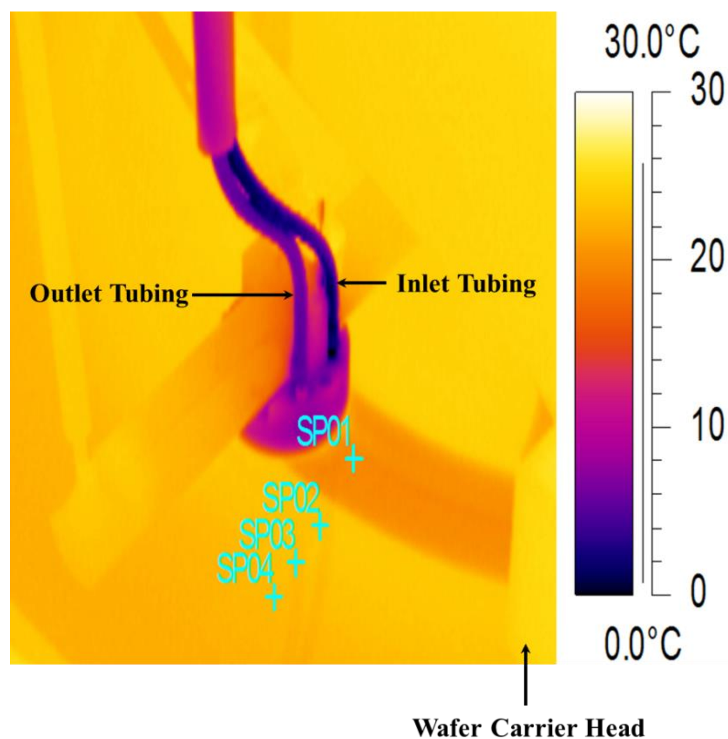

(a)

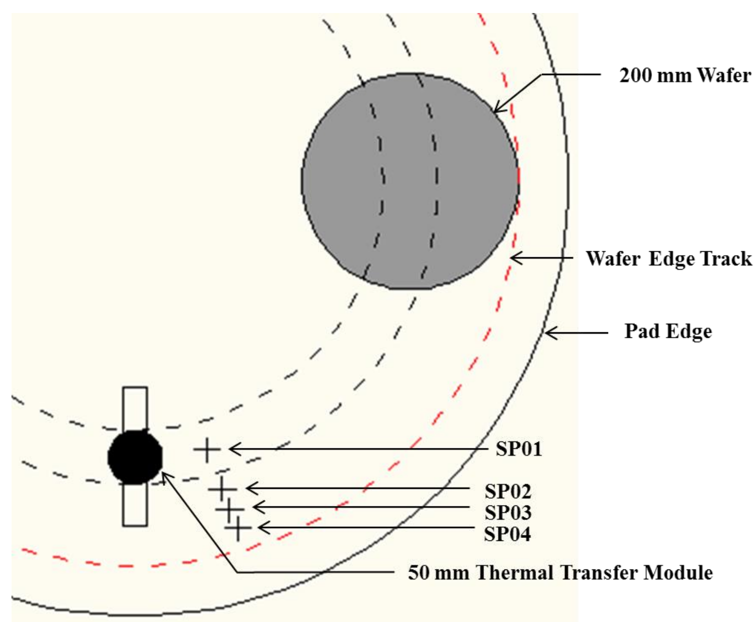

(b)

Figure 4.5: Thermal image of the pad surface (a) and locations of “SP01” through “SP04” (b) using the single thermal transfer module. Both pad and wafer are rotating in a counter-clockwise fashion.

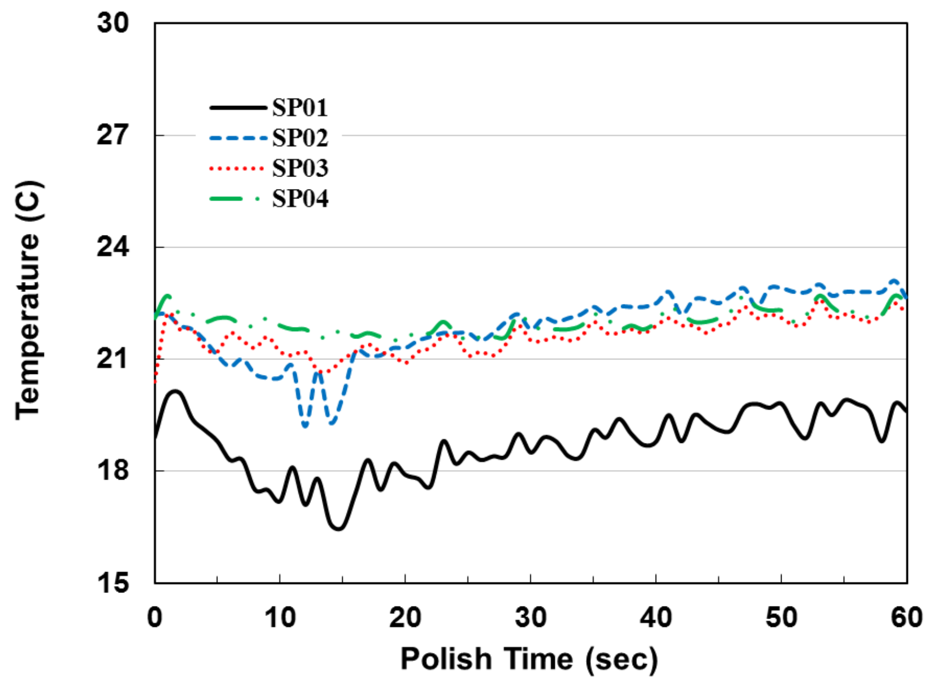

(a)

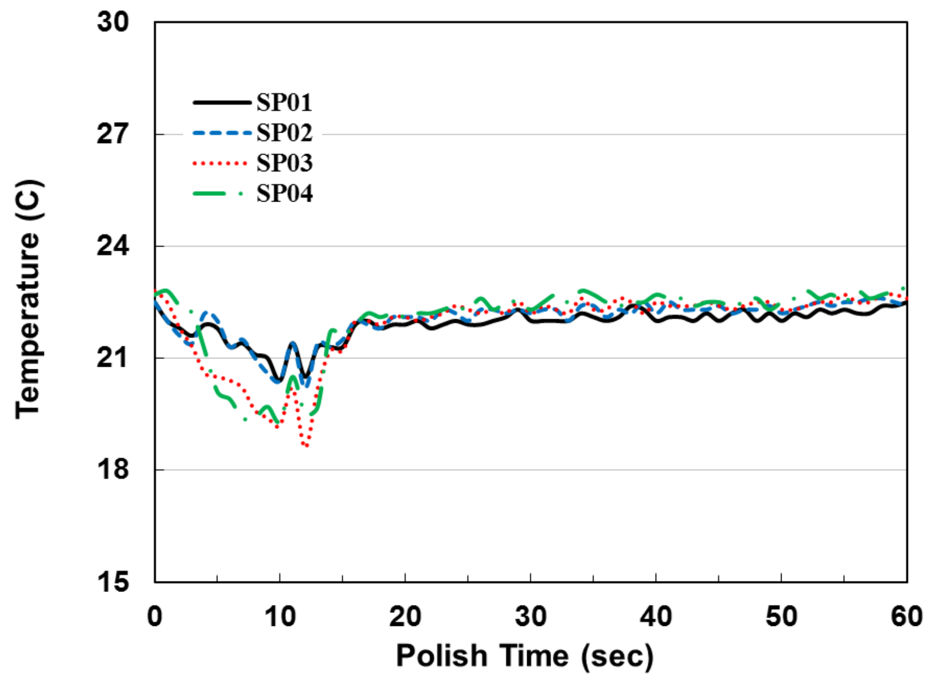

(b)

Figure 4.6: Pad surface temperature comparison with (a) and without (b) the PTM system (with the single thermal transfer module).

During in-situ pad conditioning, the diamond disk conditioner induces additional heat transfer path to the pad as it moves the slurry on top of the pad surface. As shown in Figure 4.6(a), the zigzag pattern for the measured pad surface temperatures after 15 sec polishing indicates the diamond disk sweeping effect. As the conditioner moves from the pad center to the pad edge, it drags the cool slurry that is just applied on the pad center area towards the pad edge. When the conditioner sweeps from the pad edge back to the pad center, it moves the warm polished slurry from the pad edge towards the pad center. As the conditioner sweeps back and forth covering the whole pad area, the heat transfer effect due to the conditioner is averaged out and therefore, no local effect is observed on the removal rate profile as shown in Figure 4.3.

Figure 4.3 shows the removal rate profile comparison for polishing done with and without the PTM system equipped with the single thermal transfer module. As expected, local removal rates at the wafer center region decrease significantly with the PTM system compared to the removal rate profile when the PTM system is detached.

Results in Figure 4.3 also indicate that, besides the wafer center region, local removal rates at the wafer edge region decrease as well. The main reason is that the wafer edge region periodically contacts the pad surface region with the lower temperature due to wafer rotation during polishing (see Figure 4.7).

Figure 4.7 shows that point C always contacts this region during polishing while points A and B periodically contact this region. For example, at $t = t_1$, points A and B do not contact the region. But point B contacts this region at $t = t_2$ and t_3, and point A contacts this region at $t = t_3$. The dwell time (i.e. the contact time) of a point at the wafer

surface (e.g. a random point B on the blue color circle in Figure 4.7(a)) contacting the lower temperature region can be calculated via the following equation,

$$t = \frac{length\ of\ Arc\ I + length\ of\ Arc\ \text{II}}{perimeter\ of\ the\ circle} \times polish\ time \qquad \text{Eq. 4.1}$$

Arcs I, II (in pink color) and the circle (in blue color) are shown in Figure 4.7(a).

Figure 4.8 shows the dwell time as a function of distance from the wafer center with the single thermal transfer module. Results show that a point in the wafer region from -25 to +25 mm has the longest dwell time of 60 sec. This indicates that a point in this wafer region always contacts the annular region during polishing.

In comparison, a location within the wafer from ±25 to ±100 mm only periodically contacts the annular region such that its dwell time ranges between 10 and 60 sec. As a result, the entire wafer surface is cooled and hence local removal rates decrease across the whole wafer surface, as observed in Figure 4.3. Therefore, the PTM system with a single cold module placing on the wafer center track does not improve WIWRRNU significantly in this particular case.

In order to reduce local removal rates on the wafer center region while maintaining removal rates at the wafer edge region, the PTM system, this time with two thermal transfer modules, is tested. Figure 4.9 schematically shows the positions of these two modules on the pad surface. The cold module, same as before, is placed on the wafer center track where chilled water, at 2 ℃, is introduced. On the other hand, a hot module is employed with the intention to heat the wafer edge region, this time, using 34 ℃ water.

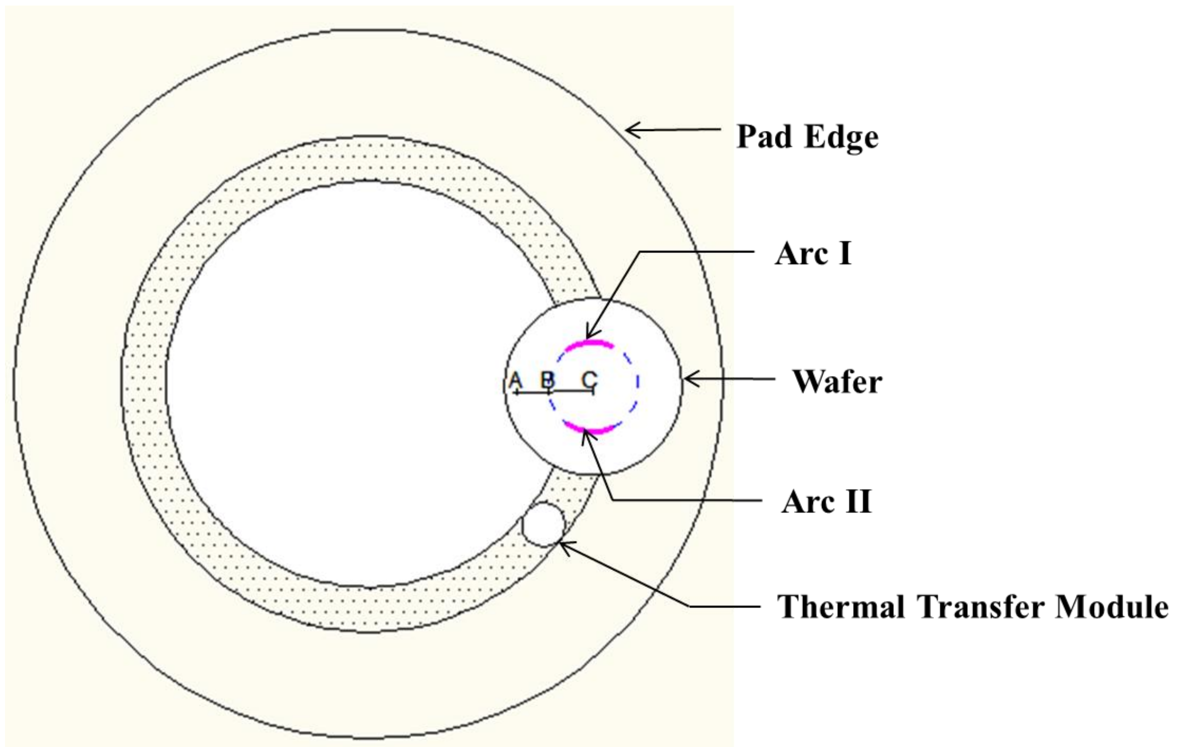

(a)

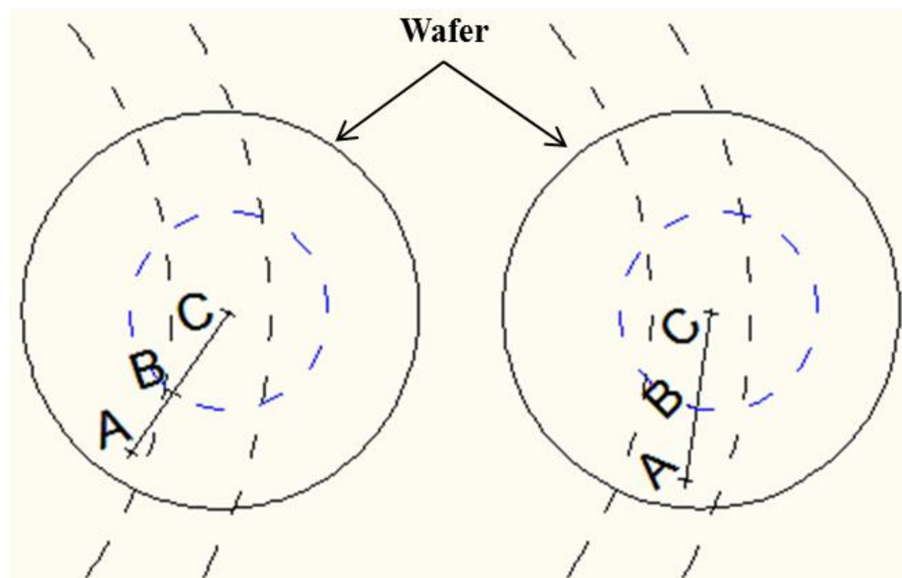

(b) (c)

Figure 4.7: Schematic of wafer rotation at (a) t = t1, (b) t = t2 and (c) t = t3 with the single thermal transfer module. Both pad and wafer are rotating in a counter-clockwise fashion.

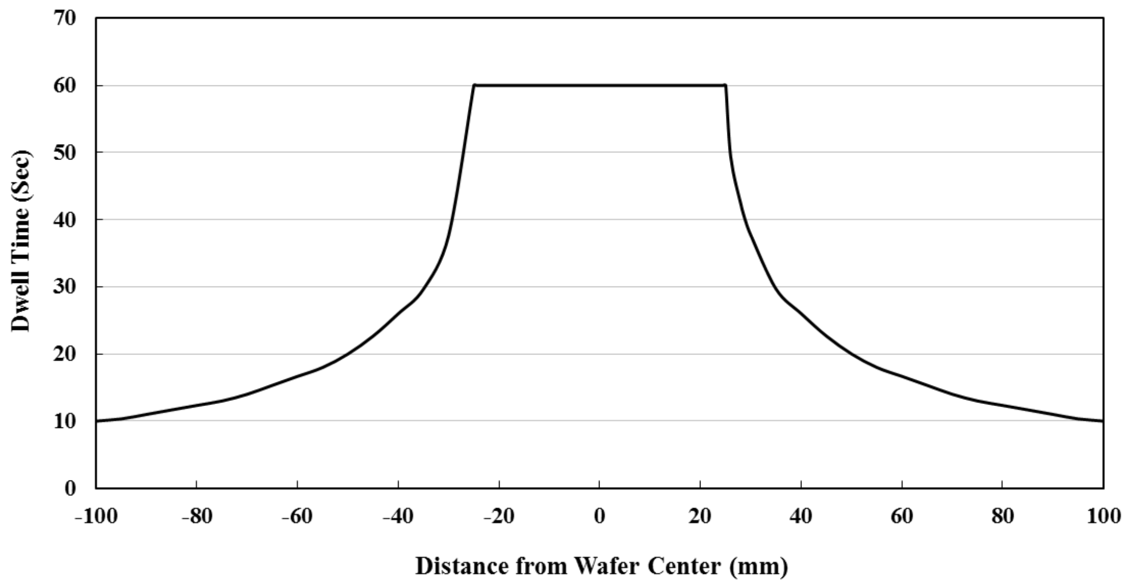

Figure 4.8: Dwell time analysis with the single thermal transfer module.

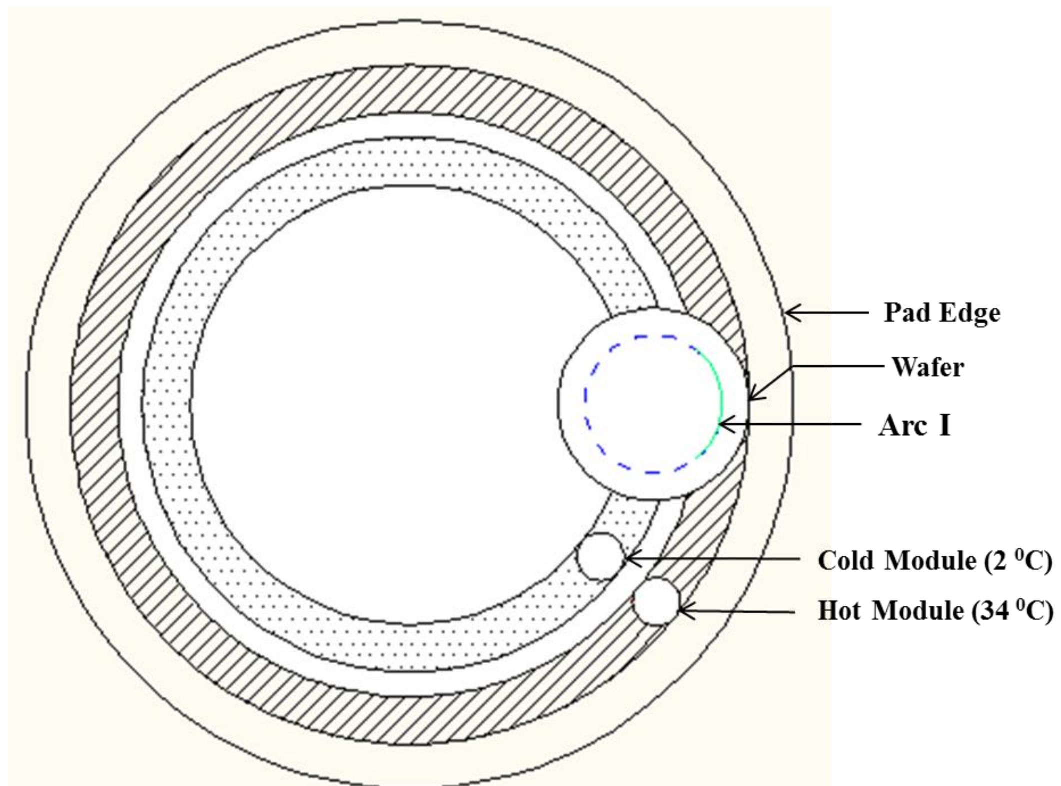

Figure 4.9: Positions of the two thermal transfer modules on the pad surface. Both pad and wafer are rotating in a counter-clockwise fashion.

Figure 4.10 shows the thermal image of the pad surface with the two thermal transfer modules. As evident in Figure 4.10, annular pad surface regions with both lower and higher temperatures are produced. Figure 4.11 summarizes the pad surface temperatures on the four spots (same locations as “SP01” through “SP04” in Figure 4.5(a)) as a function of polish time using the two modules. “SP01” is in the region where the cold module contacts, while “SP03” and “SP04” correspond to regions in contact with the hot module. “SP02” is located in the middle of the two modules. Compared to Figure 4.6(b), when the two modules are used, the temperature corresponding to “SP01” is significantly lower (on average, by 2.6 ℃) while “SP03” and “SP04” have significantly higher temperatures (on average, by 3.3 ℃), and “SP02” corresponds to a slightly higher temperature (on average, by only 1.3 ℃).

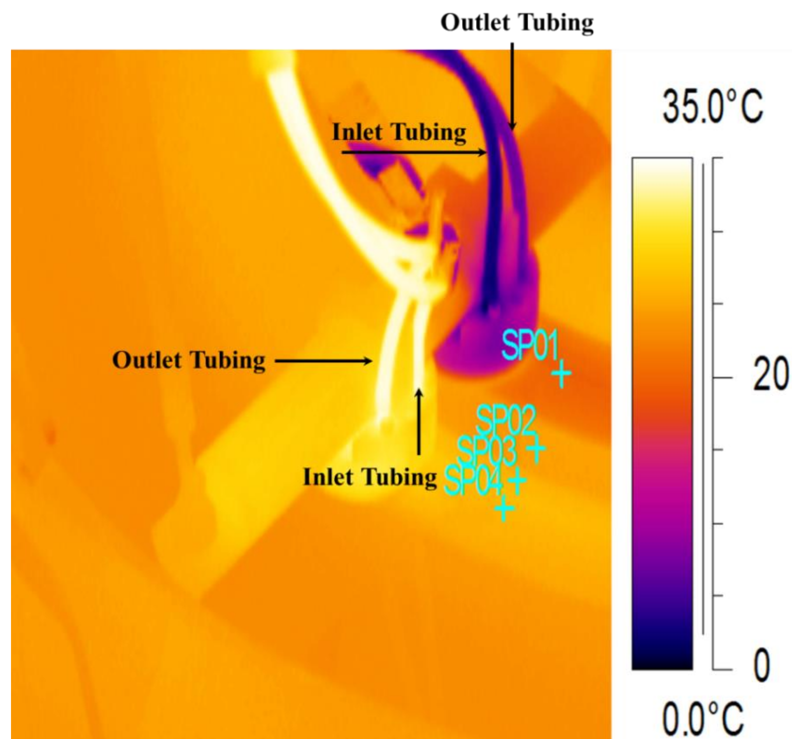

Figure 4.10: Thermal image of the pad surface with the two thermal transfer modules. Both pad and wafer are rotating in a counter-clockwise fashion.

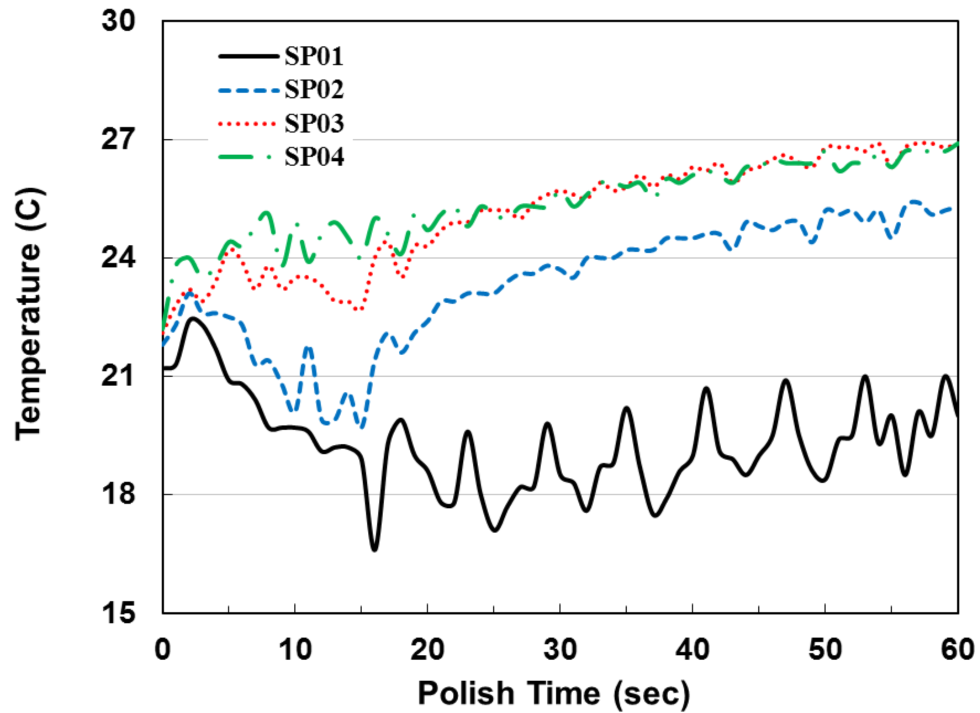

Figure 4.11: Pad surface temperature with the two thermal transfer modules.

The dwell time (calculated by Eq. 4.1) of a point at the wafer surface contacting the lower temperature region is summarized in Figure 4.12. As discussed previously, the whole wafer surface contacts the pad surface that has lower temperatures. As evident in Figure 4.9, besides the lower temperature region, the wafer edge region also periodically contacts the pad surface that has higher temperatures. The dwell time of a point at the wafer surface (e.g. a random point on the blue color circle in Figure 4.9) contacting the higher temperature region can be calculated by Eq. 4.2 and is also summarized in Figure 4.12.

$$t = \frac{length\ of\ Arc\ I}{perimeter\ of\ the\ circle} \times polish\ time \qquad \text{Eq. 4.2}$$

Arc I (in green color) and the circle (in blue color) are shown in Figure 4.9.

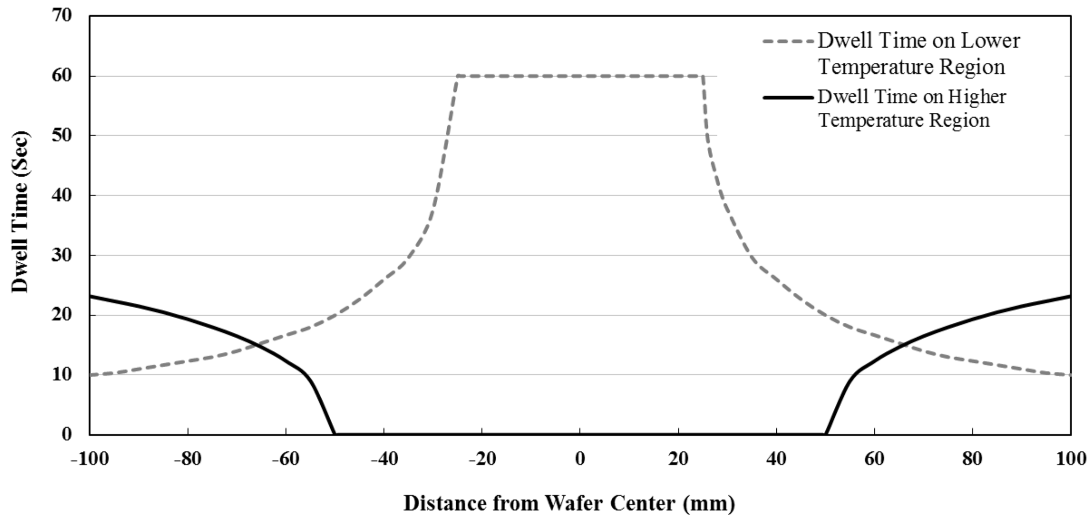

Figure 4.12: Dwell time analysis with the two thermal transfer modules.

As indicated in Figure 4.12, the wafer center region contacts the lower temperature region during polishing where its dwell time ranges from 20 to 60 sec. Therefore, it is expected that local removal rates in the wafer center region will decrease. In comparison, the wafer edge region periodically contacts the pad surface region with higher and lower temperatures, respectively. The dwell time on the lower temperature region ranges from 10 to 20 sec which should reduce local removal rates. On the other hand, the dwell time in the higher temperature region ranges from 0 to 23 sec which should enhance the local removal rates. Combining the effects of these two factors, it is expected that the local removal rates in the wafer edge region will not change significantly.

Figure 4.13 shows the removal rate profile comparison with and without the PTM system (i.e. with two thermal transfer modules). As expected, local removal rates in the

wafer center region decrease significantly. In comparison, local removal rates in the wafer edge region do not change significantly thus significantly improving WIWRRNU when two thermal transfer modules are used.

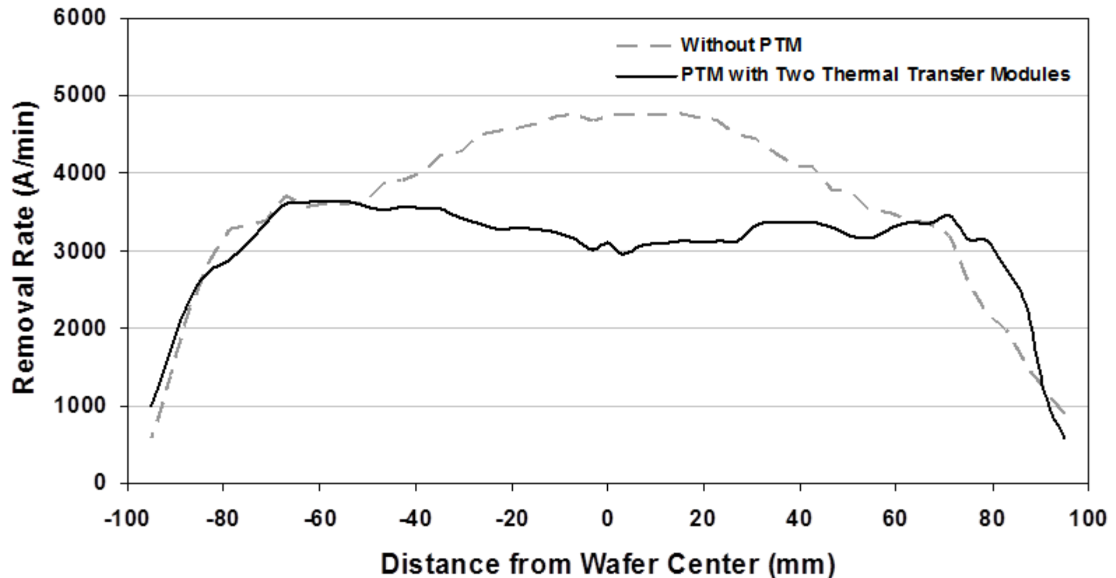

Figure 4.13: Removal rate profile comparison with and without the two thermal transfer modules.

4.5 Conclusions

This study presented the feasibility of using a novel pad surface thermal management (PTM) system to improve WIWRRNU by locally adjusting the pad surface temperature. The system successfully showed that "center-fast" removal rate profiles can be modulated and improved during copper CMP. At first, a system with a single thermal transfer module was tested. To help reduce local removal rates near the center of the wafer, a cold module was placed on the pad surface with its center corresponding to the center track of the wafer. Chilled water (2 ℃) was introduced to the module via an external chiller. Results showed that local removal rates decreased in both the central

region of the wafer as well as the edge. Therefore, the uniformity was not improved significantly since the wafer edge region periodically contacted the pad surface region with the lower temperature due to wafer rotation during polishing. As the entire wafer surface was cooled, the local removal rates decreased across the whole wafer surface. In order to reduce the local removal rates in the wafer center region while maintaining the removal rates in the wafer edge region, two thermal transfer modules were then tested. The cold module, same as before, was placed on the wafer center track and cooled water (2 ℃) was introduced. A hot module aimed to heat the wafer edge region using hot water at 34 ℃ was introduced. Results showed that local removal rates in the wafer center region decreased significantly while the removal rates in the wafer edge region were maintained. As a result, the uniformity was improved significantly: the wafer center region contacted the lower temperature region during polishing thus lowering the removal rates locally; on the other hand, as the wafer edge region periodically contacted the pad surface region with the lower and higher temperatures, respectively, the local removal rates in the wafer edge region did not change significantly.

CHAPTER 5

EFFECT OF PAD GROOVE DESIGN ON SLURRY INJECTION SCHEME DURING INTERLAYER DIELECTRIC CHEMICAL MECHANICAL PLANARIZATION

In this Chapter, the effect of pad groove design on slurry injection scheme during interlayer dielectric chemical mechanical planarization was investigated. A novel slurry injector with multiple slurry outlets was designed to allow fresh slurry to be injected through one or multiple points. At first, the one injection point scheme was compared with the standard slurry application method on a concentrically grooved pad and an xy-groove pad. On the concentrically grooved pad, the one injection point scheme generated significantly higher oxide removal rates (ranging from 22 to 35 percent) compared to the standard slurry application method at different slurry flow rates. On the xy-groove pad, the one injection point scheme still resulted in higher removal rates (ranging from 3 to 9 percent), however, its removal rate enhancement was not as high as that of the concentrically grooved pad. In order to further improve slurry availability on the xy-groove pad, the multi-injection point scheme was tested. Results showed that the multi-injection point scheme resulted in significantly higher removal rates (ranging from 17 to 20 percent) compared to the standard slurry application method. This work underscored the importance of optimum slurry injection schemes for accommodating particular pad groove designs.

5.1 Introduction

Chemical mechanical planarization (CMP) has been widely used in the integrated circuit (IC) processing industry to achieve both local and global surface planarity through combined chemical and mechanical actions (Liao *et al*. 2011; Wu *et al*. 2013). Slurry, one of the consumables, represents almost half of the total cost of ownership (COO) of the CMP module (Holland *et al*. 2002). It also contains environmentally harmful chemicals. In the current state-of-the-art, fresh slurry is injected onto near the pad center through a single tube (called standard slurry application method), as shown in Figure 5.1a. Platen-wafer rotation, pad grooves and the retaining ring help transport the fresh slurry to the pad-wafer interface. In some processes, a significant portion of the fresh slurry may flow directly off the pad surface due to the retaining ring and inertial forces without ever entering the pad-wafer interface. On the other hand, some slurry that has passed under the wafer stays on the pad (called used slurry), mixes with fresh slurry and re-enters the pad-wafer interface. The chemicals in the used slurry may become less reactive and hence may decrease material removal rate as they continue to reside on the pad surface (Sampurno *et al*. 2005). Furthermore, large amounts of deionized (DI) water are typically used to rinse the pad between wafer polishes. At the end of the pad rinse step, appreciable DI water may stay on the pad surface. When fresh slurry is introduced to polish the next wafer, it mixes with the residual water and gets diluted, resulting in lower material removal rate (Meled *et al*. 2011). As such, the standard slurry application method does not provide efficient slurry utilization. A previous study has shown that the slurry utilization efficiencies of the standard slurry application method range from 2 to 22

percent depending on operating conditions and the type of the pad grooves (Philiposisan *et al*. 2003). Therefore, developing a new slurry injection scheme that leads to more efficient slurry utilization will help achieve a more cost effective and environmentally benign process.

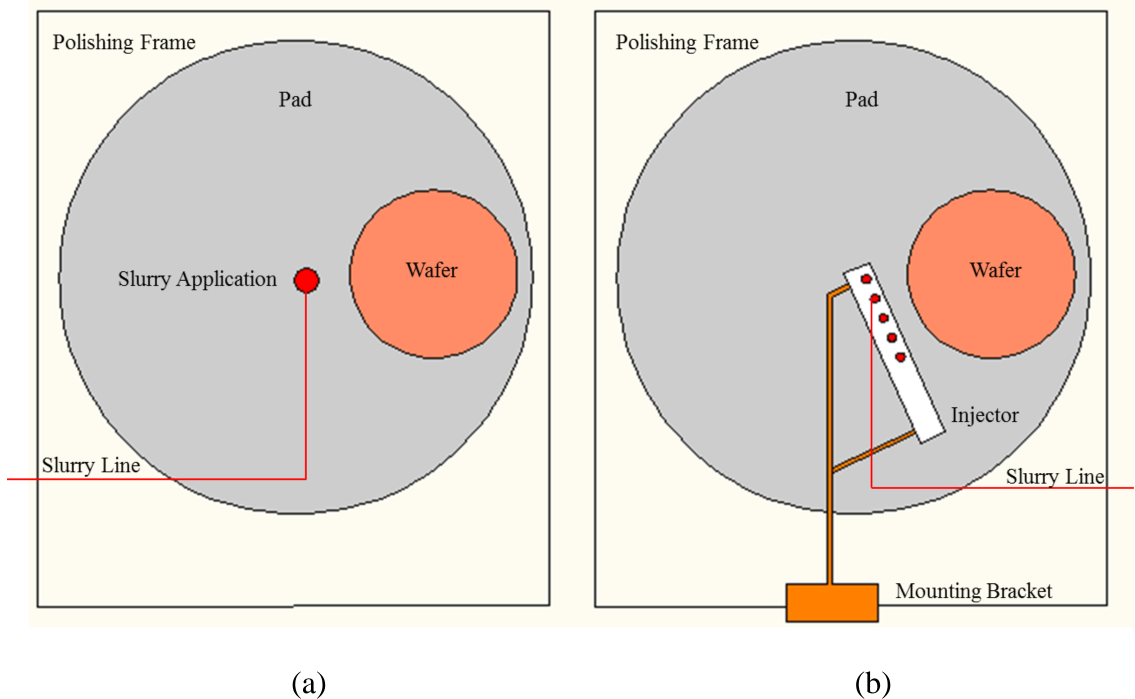

(a) (b)

Figure 5.1: Top view of a polisher with the (a) standard slurry application method and (b) novel slurry injection system. Both pad and wafer are rotating in a counter-clockwise fashion.

To date, several other slurry injection schemes have been proposed to improve slurry availability. For example, Sampurno *et al*. investigated the effect of slurry injection position on slurry utilization (Sampruno *et al*. 2005). It was found that injecting slurry at the edge of the wafer carrier could increase removal rate up to 15 percent compared to

injection at the pad center. Lu *et al*. invented an adjustable dispensing device involving a translatable slurry delivery assembly, allowing the user to dispense fresh slurry at a desired location on the pad surface (Lu *et al*. 2006). Chamberlin *et al*. and Chang proposed a method for dispensing slurry on the pad surface through multiple nozzles (Chamberlin *et al*. 1999; Chang 2005). Guthrie *et al*. proposed a two-step method for slurry distribution (Guthrie *et al*. 1998). Slurry was injected on the pad surface and a slurry wiper was then used to sweep the slurry evenly and thinly across the pad surface. While the above methods help increase slurry utilization efficiency and improve slurry flow uniformity to some extent, none of them prevent the used slurry and the rinse water from mixing with the fresh slurry, leaving significant room to maintain slurry freshness and to further improve slurry utilization.

Recently, our research team has developed a new slurry injection system (SIS). A detailed description of this system can be found elsewhere (Meled *et al*. 2011; Borucki *et al*. 2012; Liao *et al*. 2012; Borucki *et al*. 2013; Zhuang *et al*. 2014). Using the SIS, fresh slurry is introduced through an injector which is placed on the pad surface, as shown in Figure 5.1b. The pressure exerted on the pad surface by the injector is about 0.7 kPa (Meled *et al*. 2011). As such, the injector can effectively separate the used slurry and rinse water from the fresh slurry and provide improved slurry availability. Meled *et al*. showed that the SIS, on an IC1020 M-groove pad, generated significantly higher material removal rates than the standard slurry application method (Meled *et al*. 2011). However, their study did not evaluate the SIS on pad with other groove designs.

As mentioned previously, the pad groove design impacts slurry utilization efficiency (Philiposisan *et al*. 2003). As such, several questions still remain to be answered. For instance, compared to the standard slurry application method, can the SIS also generate significantly higher removal rate on pad with other groove designs? And how does the pad groove design impact slurry injection scheme?

This study aims to answer the above questions and to expose the importance of optimum slurry injection schemes for accommodating particular pad groove designs. A novel slurry injector of the SIS is developed, which provides optional slurry injection schemes (i.e. one injection point scheme and multi-injection point scheme). These injection schemes are compared with the standard slurry application method on a concentrically grooved pad and an xy-groove pad, respectively.

5.2 The Slurry Injector

Figure 5.2 schematically shows the novel slurry injector developed in this study. As can be seen from Figure 5.2a, the injector consists mainly of a “body” and an “arm”. The “body” has a rectangle shape and is attached to the “arm” by two connecting rods. The injector is placed on the pad surface and attached to the polisher by a mounting bracket through the “arm”. Multiple slurry inlets (referred to as inlet A ~ E, as shown in Figure 5.2a) are designed on the top of the “body” and each inlet matches an outlet (referred to as outlet A ~ E, as shown in Figure 5.2b) at the bottom of the “body” (in the trailing edge). The distance between two adjacent inlets or outlets is 28 mm. This design allows one to inject the slurry through one or multiple holes. Fresh slurry is introduced

through the slurry line from the slurry tank where it flows into the inlet(s), and then flows out through the outlet(s). In addition, a channel (see Figure 5.2b) which connects these five outlets is designed at the bottom of the "body". It helps spread the fresh slurry onto pad surface during polishing.

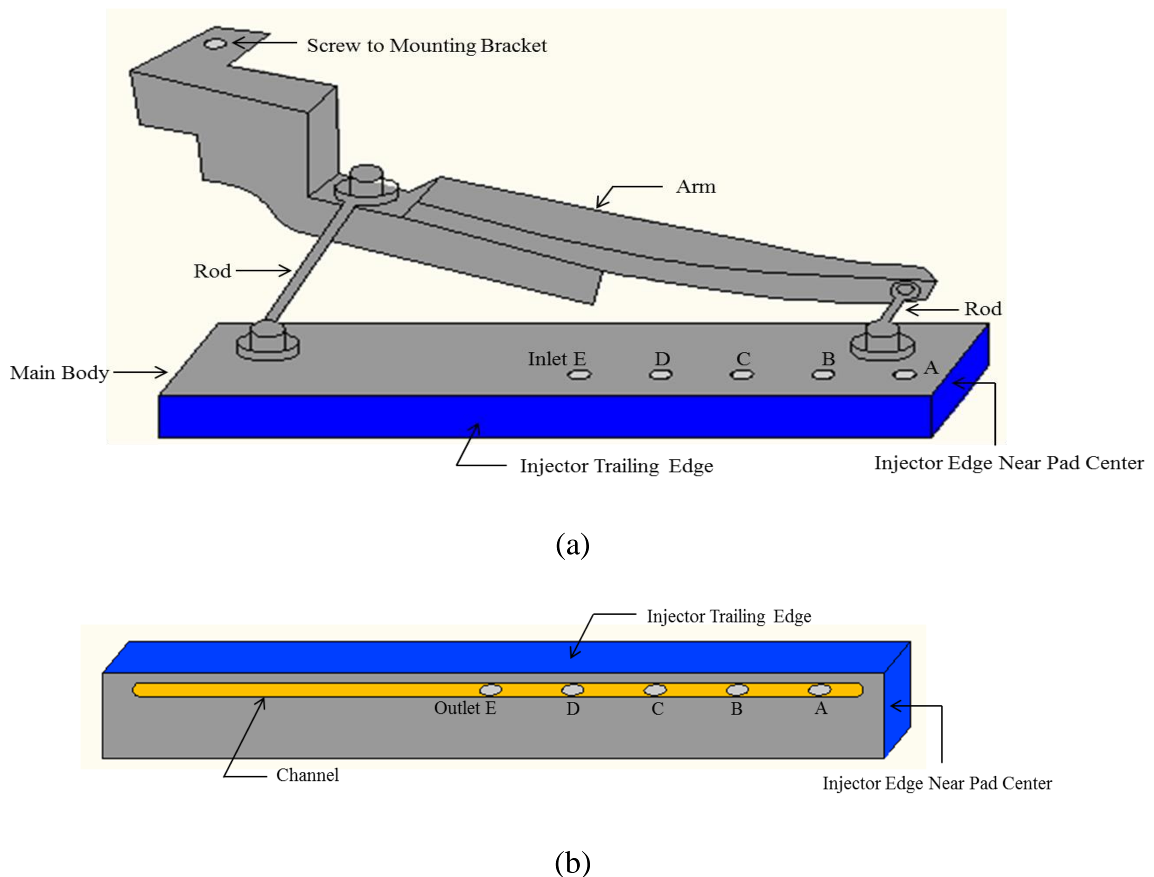

Figure 5.2: Schematic of (a) the novel slurry injector and (b) its "body" bottom.

5.3 Experimental

In this study, SIS was used to inject fresh slurry onto the pad surface. For comparison, the standard slurry application method was also employed. To investigate the effect of pad groove design, an IC1000 concentrically grooved pad and an IC1000 xy-

groove pad were tested. Concentric groove and xy groove were selected because they represented a highly non-communicative groove and a highly communicative groove pad, respectively, and because both designs are used widely in high volume manufacturing worldwide. For the communicative pads, grooves are connected to one another. In comparison, for non-communicative pads, grooves do not "talk" to one another (Philiposisan *et al*. 2003).

In these tests, 200-mm blanket oxide wafers were polished on an Araca APD-800 polisher and tribometer, equipped with the unique ability to acquire real-time shear force and down force during polishing (http://aracainc.com/products/apd-800; Liao 2014). A 3M A2810 diamond disk was used to condition the pads with *ex-situ* for 45 sec between wafer polishing at a conditioning down-force of 59.2 N. Each wafer was polished for 1 minute at 22.8 kPa and 0.71 m/s. Prior to wafer polishing, the diamond disk was used to break-in each pad for 15 min with DI water. The disk rotated at 95 RPM and swept at a frequency of 11 per minute across the radius of the pad surface. Pad break-in was followed by pad seasoning during which the shear force was monitored to ensure that stable values were achieved prior to monitor wafer polishing (Liao *et al*. 2013).

The polishing slurry consisted of 1 volume part of Cabot Microelectronics Semi-Sperse 25 slurry and 1 volume part of DI water. Three slurry flow rates (200, 150, and 100 ml/min) were tested. For each slurry flow rate, 4 monitor oxide wafers were polished to confirm the experimental reproducibility. Before and after polishing, a reflectometer from SENTECH Instruments GmbH was used to measure oxide film thickness to calculate the removal rate.

5.4 Results and Discussion

At first, the SIS with only one injection point is compared with the standard slurry application method on both the concentrically grooved and the xy-groove pad. For the one injection point scheme, fresh slurry is introduced through the slurry line from the slurry tank where it flows into the inlet A, and then flows out through the outlet A (see Figure 5.2).

Figure 5.3 shows the removal rate comparison between the one injection point scheme and standard slurry application method on the concentrically grooved pad. Oxide removal rates are measured as a function of slurry flow rates ranging from 100 to 200 ml/min. The error bars in Figure 5.3 represent the standard deviation of removal rates. As evident from Figure 5.3, the one injection point scheme generates significantly higher removal rate than the standard slurry application method at all three slurry flow rates, ranging from 22 to 35 percent. This indicates that either a lower slurry flow rate or a shorter polishing time can be adopted for removing the same amount of material. Therefore, slurry usage can be reduced. Based on Figure 5.3, the one injection point scheme with a slurry flow rate of 100 ml/min generates higher removal rate than that of the standard slurry application method at 200 ml/min (i.e. 1,580 vs. 1,358 A/min). This implies that the slurry flow rate can be cut in half and throughput can still be enhanced by the one injection point scheme compared to the standard slurry application method at 200 ml/min.

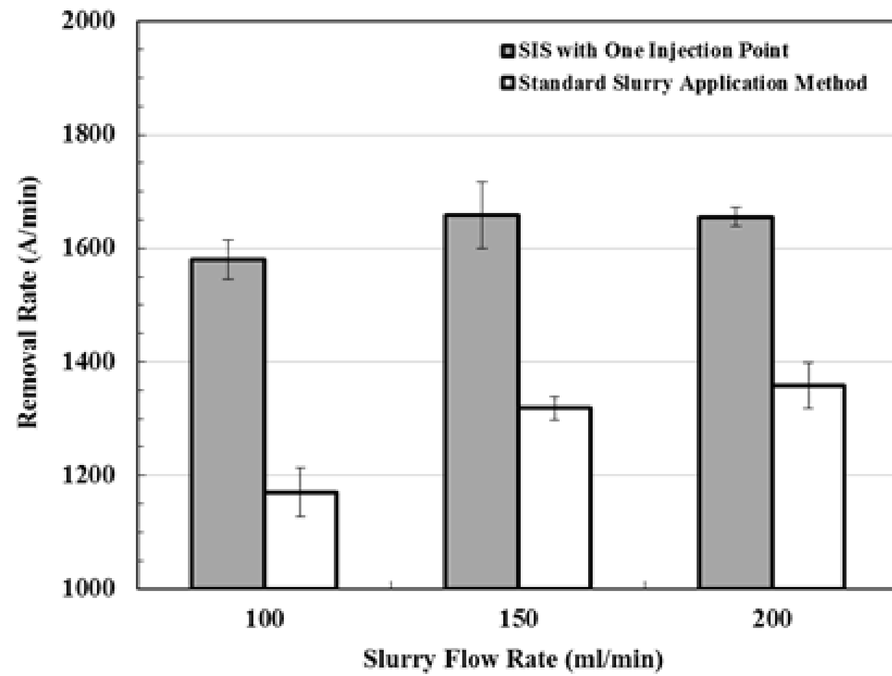

Figure 5.3: Removal rate comparison between the one injection point scheme and standard slurry application method on the concentrically grooved pad.

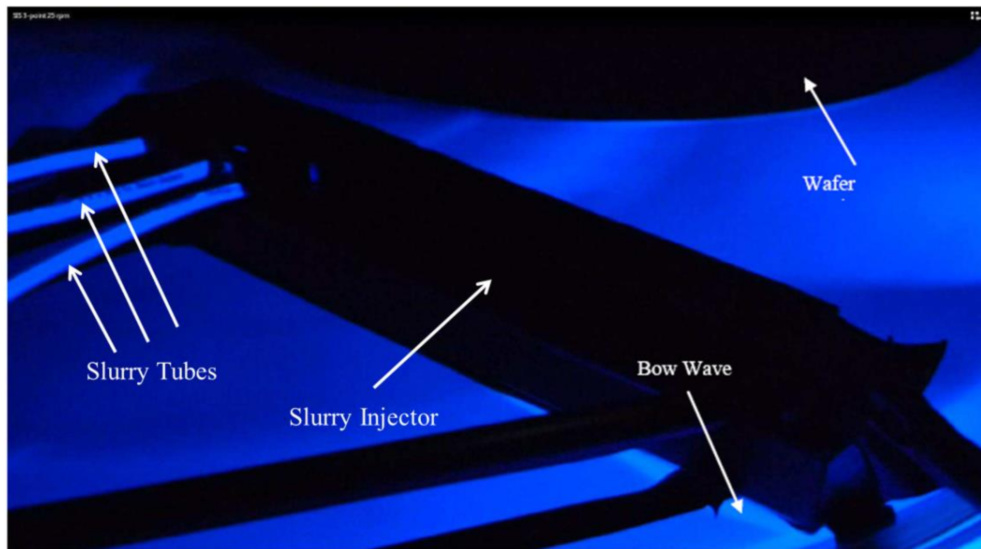

Figure 5.4: An example slurry distribution image with SIS collected via UVIZ-100 system (Zhuang *et al*. 2014).

Since the slurry injector is placed on the pad surface, its "body" is capable of effectively separating the used slurry and the residual DI water from the fresh slurry. This can be confirmed by the thick bow wave formed at the injector leading edge during the pad rinse step and wafer polishing (Meled *et al*. 2011; Zhuang *et al*. 2014). For example, Figure 5.4 shows a slurry distribution image collected via a UVIZ-100 system (Zhuang *et al*. 2014). The detailed description of this system can be found elsewhere (Liao *et al*. 2012). As evident from Figure 5.4, the bow wave was formed at the injector leading edge during wafer polishing. As a result, oxide removal rates are enhanced by the one injection point scheme. Meled *et al*. performed slurry mean residence time (MRT) test during wafer polishing and found that the SIS generated significantly lower slurry MRTs (ranging from around 27 to 50 percent depending on slurry flow rate) than the standard slurry application method (Meled *et al*. 2011). Assuming the pad-wafer interface acts as a closed reactor, the slurry MRT refers to the average time that the slurry spends in the pad-wafer interface. As such, lower slurry MRTs indicate the presence of a fresher slurry during wafer polishing and which can lead to higher removal rates (Meled *et al*. 2011).

Figure 5.5 shows the removal rate comparison between the one injection point scheme and standard slurry application method on the xy-groove pad. The error bars in Figure 5.5 represent the standard deviation of removal rates. The one injection point scheme as well generates higher removal rates than the standard slurry application method at all three different slurry flow rates (on average, by 3 to 9 percent). As discussed previously, the main reason is that the slurry injector effectively separates the used slurry and the rinse water from the fresh slurry.

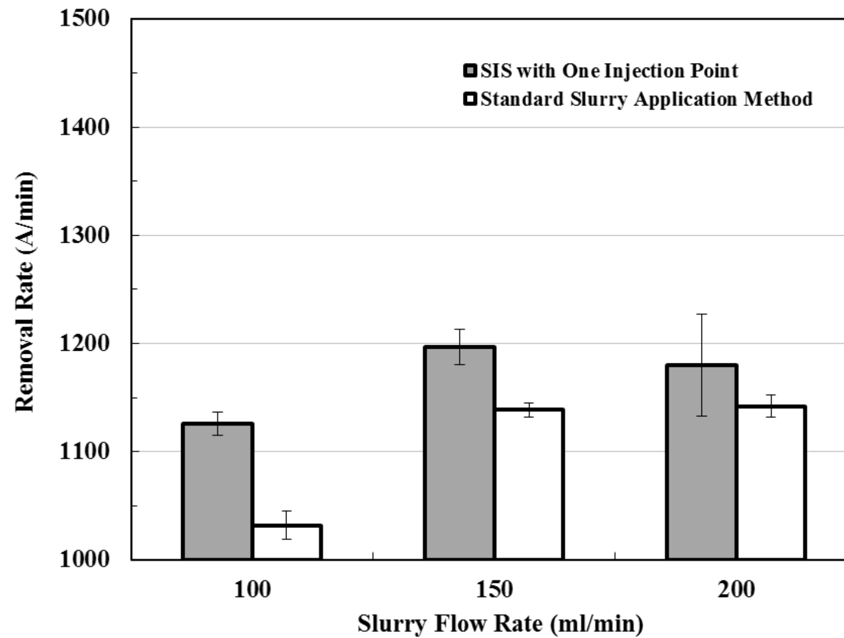

Figure 5.5: Removal rate comparison between the one injection point scheme and the standard slurry application method on the xy-groove pad.

Comparing Figures 5.3 and 5.5, the one injection point scheme generates significantly lower removal rate on the xy-groove pad than on the concentrically grooved pad. This is associated with the different slurry flow patterns on these two types of pads. Figures 5.6a and b schematically show the slurry flow patterns on the concentrically grooved pad and xy-groove pad, respectively. For the concentrically grooved pad, grooves are non-communicative and hence relatively higher flow resistance exists through the grooves (Philiposisan *et al*. 2003). As such, most of fresh slurry flows through the channel at the injector bottom and goes over from one pad land area to another, as shown in Figure 5.6a. Therefore, more fresh slurry is retained on the pad land

area, where polishing occurs, resulting in higher removal rates. In comparison, for the xy-groove pad, grooves are highly communicative and extend off to the edge of the pad (Philiposisan *et al*. 2003). This results in relatively lower flow resistance through the grooves. As such, when fresh slurry is injected through a single point, some of fresh slurry still flows through the channel while a large portion of fresh slurry flows directly into the grooves without participating in polishing (see Figure 5.6b). Therefore, on the xy-groove pad, the one injection point scheme retains relatively less fresh slurry on the pad land area, thereby resulting in lower removal rates.

Figures 5.3 and 5.5 also show that the removal rate enhancement by the one injection point scheme on the xy-groove pad (i.e. 3 to 9 percent) is not as high as the enhancement seen on the concentrically grooved pad (i.e. 22 to 35 percent). As stated previously, the xy-groove pad has relatively lower flow resistance through grooves. As such, the used slurry and rinse water can also easily flow off the pad without participating in wafer polishing, and hence they can have a relatively less negative impact on removal rate. This could explain the lower removal rate enhancement by the one injection point scheme observed on the xy-groove pad compared to the concentrically grooved pad.

Based on the above analysis, retaining more fresh slurry on the pad land areas will help further increase removal rates on the xy-groove pad. The SIS, this time with the multi-injection point scheme, is tested. As the pitch size of the xy-groove pad is 38 mm and the distance between two adjacent slurry outlets is 28 mm, the multi-injection point scheme should have a higher possibility to spread fresh slurry over a larger pad land area and therefore retain more fresh slurry on the pad (Borucki *et al*. 2013). In this study, the

scheme with four injection points is tested. Fresh slurry is introduced through the slurry line from the slurry tank where it flows into inlets A ~ D evenly via a slurry distribution manifold, and then flows out through the outlets A ~ D (see Figure 5.2).

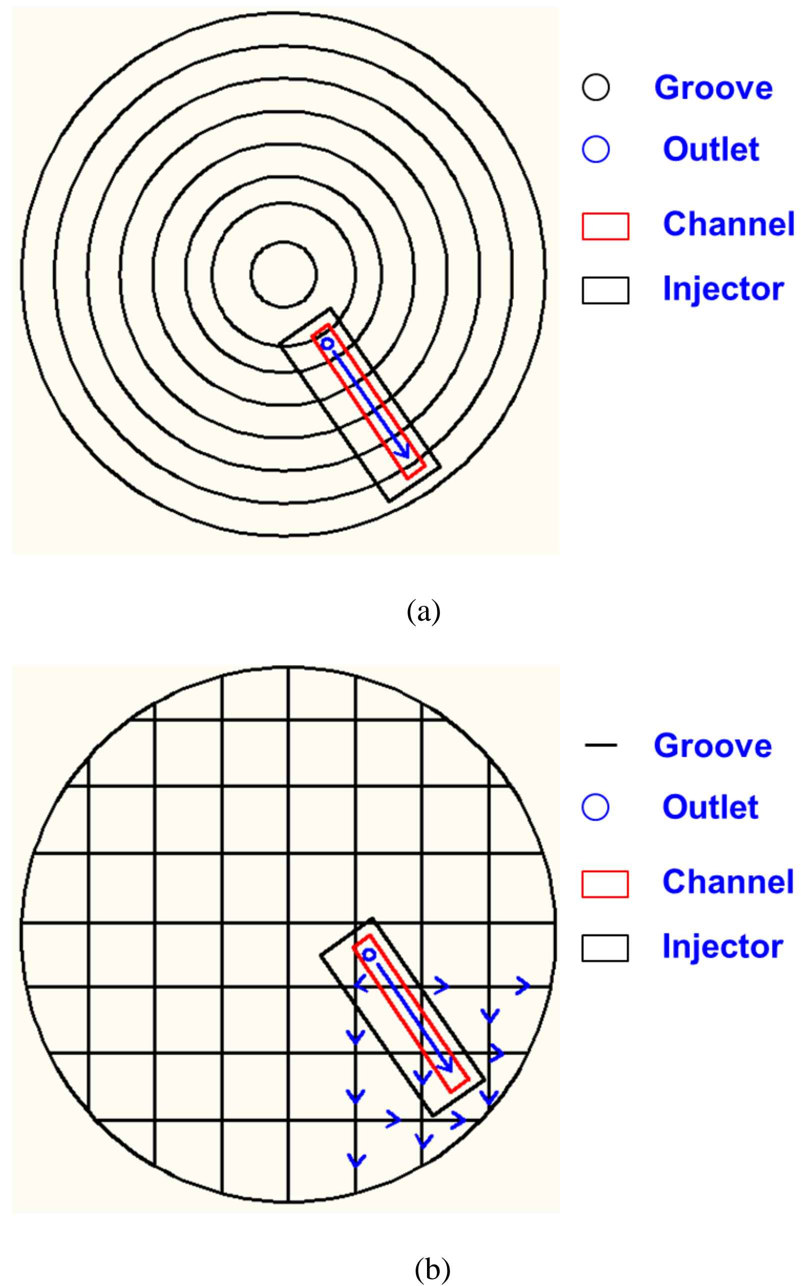

Figure 5.6: Schematic of slurry flow patterns on the (a) concentrically grooved pad and (b) xy-groove pad.

Figure 5.7 shows the removal rate comparison among these three slurry injection schemes on the xy-groove pad. As evident from Figure 5.7, the SIS with multi-injection point scheme enhances oxide removal rate further (ranging from 17 to 20 percent) compared to the standard slurry application method. Based on Figure 5.7, the slurry flow rate can be cut in half and throughput can still be enhanced by the multi-injection point scheme compared to the standard slurry application method at 200 ml/min. It is therefore important to optimize slurry injection schemes to accommodate particular pad groove designs.

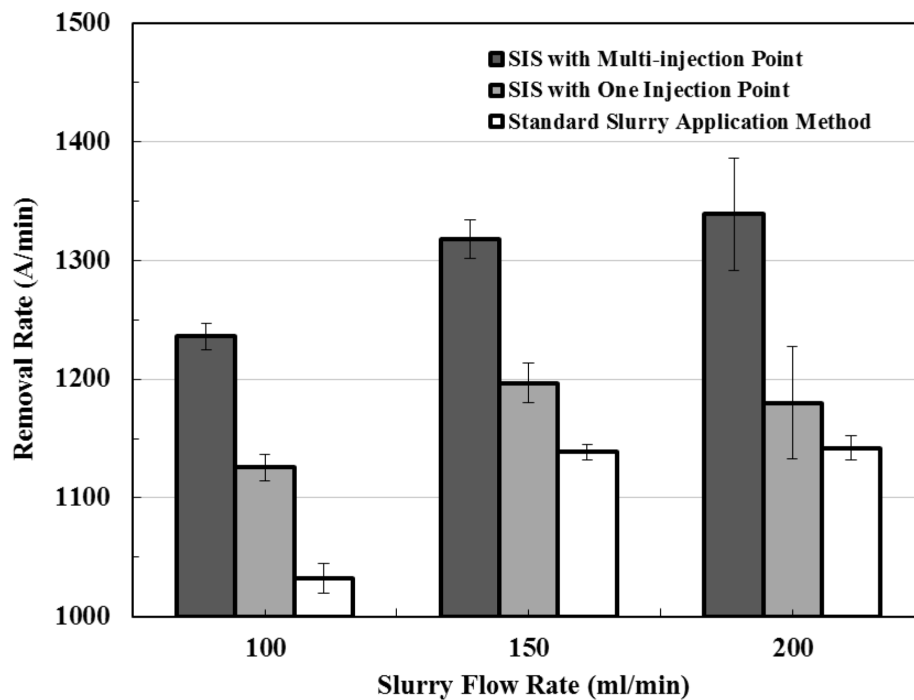

Figure 5.7: Removal rate comparison among different slurry injection schemes on the xy-groove pad.

5.5 Conclusions

In this study, the effect of pad groove design on slurry injection scheme during ILD CMP was investigated. A novel slurry injector was developed, which could provide optional slurry injection schemes, namely a one injection point scheme and a multi-injection point scheme. These injection schemes were tested on an IC1000 concentrically grooved and an IC1000 xy-groove pad. At first, the one injection point scheme was investigated on both pads. For the concentrically grooved pad, the one injection point scheme generated significantly higher removal rates (ranging from 22 to 35 percent) compared to the standard slurry application method. As such, slurry usage could be reduced by at least a factor of 2. This was due to the fact that the slurry injector could effectively separate the used slurry and the rinse water from the fresh slurry. On the xy-groove pad, the one injection point scheme still resulted in higher removal rates (ranging from 3 to 9 percent), however, its removal rate enhancement was not as high as that of the concentrically grooved pad (ranging from 22 to 35 percent). This was believed to be due to different slurry flow patterns on both pads. On the xy-groove pad, when one injection point scheme was used, a large portion of fresh slurry flowed directly to grooves without participating in polishing. Therefore, relatively less fresh slurry was retained on the pad land area which contributed to lower oxide removal rate. In order to further improve slurry availability on the xy-groove pad, the multi-injection point scheme was tested. Data showed that the multi-injection point scheme enhanced oxide removal rate further (ranging from 17 to 20 percent) compared to the standard slurry application

method. As the multi-injection point scheme could retain more fresh slurry on the pad land area, higher oxide removal rates were achieved.

CHAPTER 6

AGGRESSIVE DIAMOND CHARACTERIZATION AND WEAR ANALYSIS DURING CHEMICAL MECHANICAL PLANARIZATION

In this Chapter, a 3M A3700 diamond disk was used to condition a Cabot Microelectronics Corporation D100 pad for 30 hours. The extent of wear on its aggressive diamonds was then analyzed. The top 20 aggressive diamonds for two perpendicular disk orientations were identified before wafer polishing, as well as after 15-hour and 30-hour polishing. Results showed that the original top 20 aggressive diamonds identified before polishing were subjected to wear after the first 15-hour polishing as the furrow surface area that they generated decreased dramatically (by 47%). As these original aggressive diamonds were worn, seven new aggressive diamonds were "born" and joined the new top 20 list for both disk orientations. After the second 15-hour wafer polishing, the furrow surface area of these new top 20 aggressive diamonds did not change significantly. The furrow surface area created by all the active diamonds exhibited the same trend as the top 20 aggressive diamonds, confirming that most pad conditioning work was performed by these aggressive diamonds and that the disk lost its aggressiveness in the first 15 hours of polishing and then maintained its aggressiveness during the second 15 hours, albeit to a lesser extent.

6.1 Introduction

CMP has been widely employed in the integrated circuit manufacturing industry to achieve local and global surface planarity. It is well known that diamond disks are

commonly used for pad conditioning to prevent removal rate decay during CMP as the embedded diamonds cut across the pad surface under an applied load to regenerate pad asperities and remove used slurry and pad debris (Tsai *et al*. 2010; Tsai *et al*. 2011; Meled *et al*. 2010). During pad conditioning, pad asperities and slurry abrasives make mechanical contact with the diamonds causing the diamonds to wear (Meled *et al*. 2010), leading to the loss of disk effectiveness. A conventional diamond disk is typically replaced after dozens of hours of use (Borucki *et al*. 2007). Therefore, it is important to investigate diamond wear and loss of disk efficiency.

There have been a few studies on diamond wear during CMP. For example, Liao found that peripheral diamonds and the diamonds that originally protrude higher with crest lines oriented upward wear faster (Liao 2008). Borucki *et al.* demonstrated that for a conventional diamond disk, typically less than 1 percent of the embedded diamonds (called active diamonds) create cutting furrows on the pad surface during pad conditioning. Other diamonds (referred as inactive diamonds) are not involved in pad cutting. Among the active diamonds, typically only 10 to 20 diamonds (named as aggressive diamonds) do the majority of the cutting and are therefore most susceptible to fracture or pulled out (Borucki *et al*. 2007; Borucki *et al*. 2008). In a recent study, Meled *et al.* conducted 24-hour wear tests using three types of diamond disks (Meled *et al*. 2010). Results showed the presence of micro-wear on the aggressive diamonds but no appreciable wear on the inactive diamonds. While diamond wear has been characterized to some extent, several questions remain unanswered. For example, do new aggressive diamonds appear as the original aggressive diamonds wear? How do these new

aggressive diamonds impact disk efficiency (or aggressiveness)? And, how does the disk aggressiveness change throughout the life of the disk? This study aims to answer the above questions and to provide a better understanding of diamond wear and its impacts on the process. In this study, a 3M diamond disk is used to condition a Cabot Microelectronics Corporation (CMC) D100 pad for 30 hours. The top 20 aggressive diamonds for two perpendicular disk orientations were identified before the polishing, as well as after 15-hour and 30-hour polishing. The furrow surface area generated by these top 20 aggressive diamonds and its evolution was analyzed and compared.

6.2 Experimental

Aggressive diamond identification and furrow surface area analysis

The top 20 aggressive diamonds for two perpendicular disk orientations were identified by performing a dragging test prior to wafer polishing, as well as after 15-hour and 30-hour polishing. A brief description of the dragging test is summarized below while a more detailed description can be found elsewhere (Wei *et al*. 2010).

Figure 6.1 shows the experimental setup for the disk dragging test. Due to the fact that furrows on the polyurethane pad are hardly visible and recognizable, a pad substitute material (General Electric Plastics XL10 polycarbonate sheet) with similar mechanical properties but more favorable optical properties was used. The XL10 polycarbonate sheet has a slightly higher Shore D hardness (80 for the XL10 polycarbonate sheet and 52 - 70 for hard polyurethane pads). The transparent polycarbonate sheet was positioned on a precision optical mirror, which was fixed in the frame to provide a flat and rigid surface

for supporting the sheet. The disk holder was attached to the backside of the disk and 8 labels were then marked every 45 degrees on the disk sidewall according to the angle scale on the disk holder. The 8 labels represented 8 different disk orientations, which were used for exactly and reproducibly controlling disk orientation relative to the dragging direction. In this study, two perpendicular disk orientations (Orientation 1 and 7) were examined and one dragging test was performed for each disk orientation before wafer polishing, as well as after 15-hour and 30-hour polishing. During the dragging test, dead weights were applied on the disk assembly to provide the same conditioning force (13.3 N) used during wafer polishing. The disk was then slowly dragged over a distance that exceeded its diameter. After the dragging test, visible furrows were generated on the polycarbonate sheet by the active diamonds embedded in the disk. A surface profilometer (Veeco Dektak V200 SI) was used to scan across the furrows. For each furrow, its surface area (defined as the cross sectional area of the subsurface portion of the furrow), its surface area percentage (determined by dividing the individual furrow surface area by the total furrow surface area generated by all active diamonds), and furrow location were obtained from the scan (see Figure 6.2) via a customized software. Based on the measured furrow surface area, each furrow was then ranked. The top 20 aggressive diamonds that generated the 20 largest furrow surface areas were then identified for each disk orientation based on the locations of the furrows that they created. During our internal studies in which multiple dragging tests were performed for the same disk with the same disk orientation, the standard deviation of furrow surface area was within 15

percent of the measured average value, therefore confirming the repeatability of this technique.

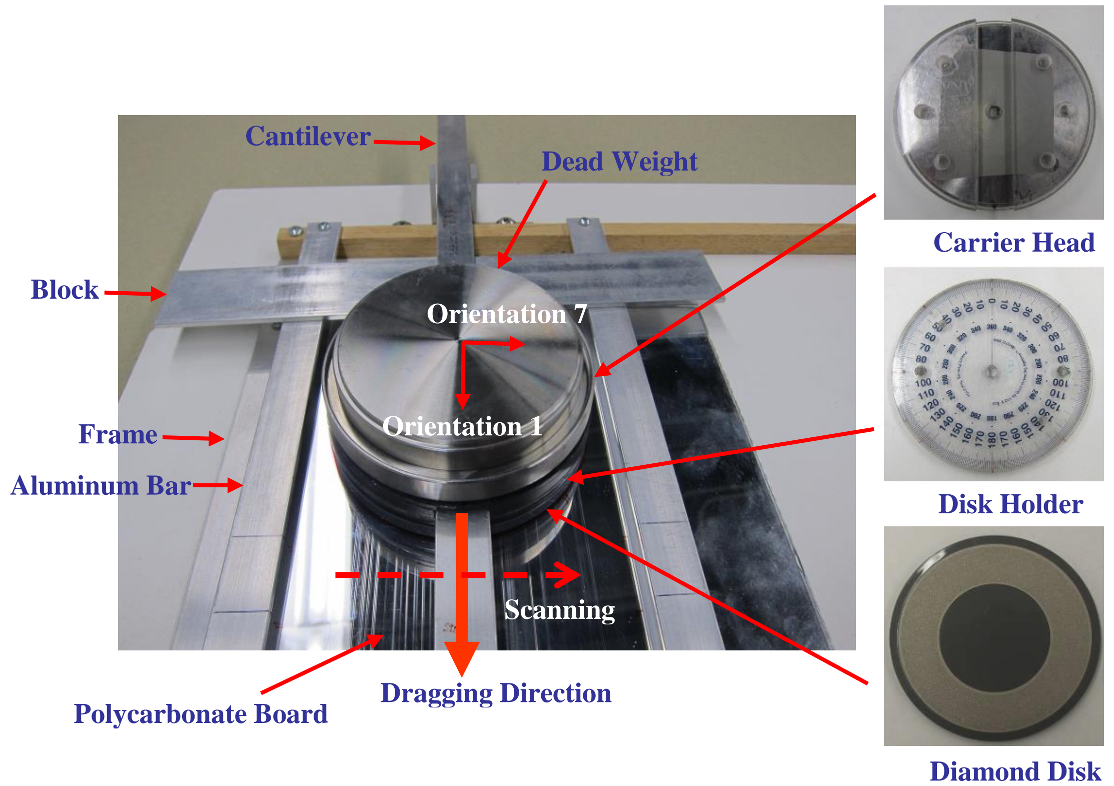

Figure 6.1: Experimental setup for disk dragging test.

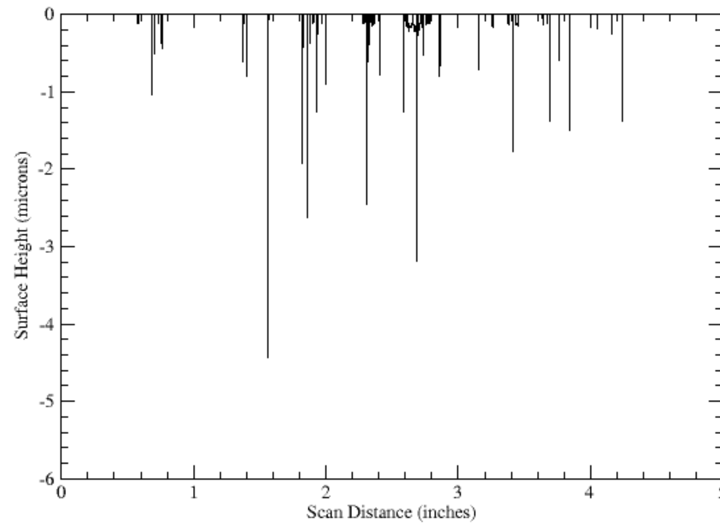

Figure 6.2: Profile scan of the surface of the polycarbonate sheet.

To verify that a flat XL10 polycarbonate sheet was suitable as a pad substitute material for identifying the active diamonds, a dragging test was performed on a polycarbonate sheet and a flat IC1000 pad and the results were compared (Wei 2010). The same disk was dragged under the same down force on the polycarbonate sheet and IC1000 pad. To make scratches detectable, a thin chromium film (about 50 nm thick) was deposited on the IC1000 pad surface. The origins of the scratches were carefully marked as shown in Figure 6.3. Results showed that the number of scratches (indicating the number of active diamonds) on the XL10 polycarbonate sheet was about 10 percent less than that on the IC1000 pad. In addition, Borucki *et al.* compared the surface height probability density function (PDF) distributions of a flat XL10 polycarbonate sheet with a grooved IC1000 pad after the same diamond disk was used to condition them under the same down force (Borucki *et al*. 2007). It was found that the two surfaces exhibited nearly identical height variations in the right-hand tail of the PDF. Furthermore, these two materials had comparable cut rates. Based on the above results, the XL10 polycarbonate sheet was validated as a pad substitute material for diamond disk characterization.

Wafer polishing and pad conditioning

An Araca APD-800 polisher (http://www.aracainc.com/products/apd-polishers) was used for all polishing experiments. Blanket 300-mm silicon wafers were polished on a 31-inch CMC D100 concentrically grooved pad with *in-situ* pad conditioning for 30 hours. A 3M A3700 diamond disk was used to condition the pad at the conditioning force

of 13.3 N. The disk rotated at 95 RPM and swept 10 times per minute across the pad surface. The wafer polishing pressure was 10.3 KPa and the sliding velocity was 2.2 m/s (the pad and wafer rotated at 93 RPM). Deionized water was applied at 300 ml/min during wafer polishing.

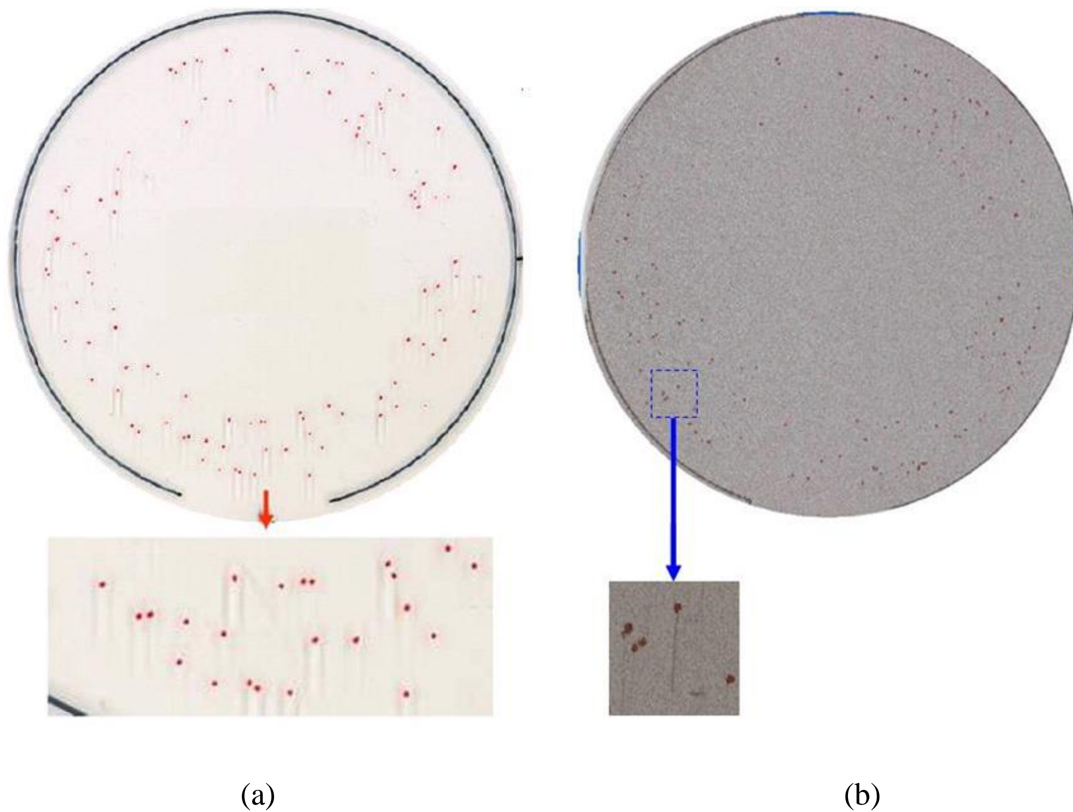

(a) (b)

Figure 6.3: Photograph of (a) the XL10 polycarbonate sheet and (b) chromium deposited IC1000 pad with scratches marked (Wei 2010).

6.3 Results and Discussion

Figure 6.4 shows the changes in the furrow surface area generated by the original top 20 aggressive diamonds identified before wafer polishing during the 30-hour tests.

Results indicate that furrow surface area decreases dramatically (45 percent for Orientation 1 and 48 percent for Orientation 7) after the first 15 hours of polishing and remains relatively stable following the second 15-hour polishing. As stated previously, during our internal studies, the standard deviation of furrow surface area was within 15 percent of the measured average value, therefore a 47% change in the furrow surface area is considered to be statistically significant. Also, for both orientations, the original top 20 aggressive diamonds are subjected to wear after the first 15-hour polishing and then experience minimum wear during the second 15-hour polishing. As an example, Figure 6.5 shows the SEM images of a diamond from the original top 20 aggressive diamonds. This particular diamond exhibits appreciable micro wear on its cutting point and becomes inactive after the 30-hour polishing test.

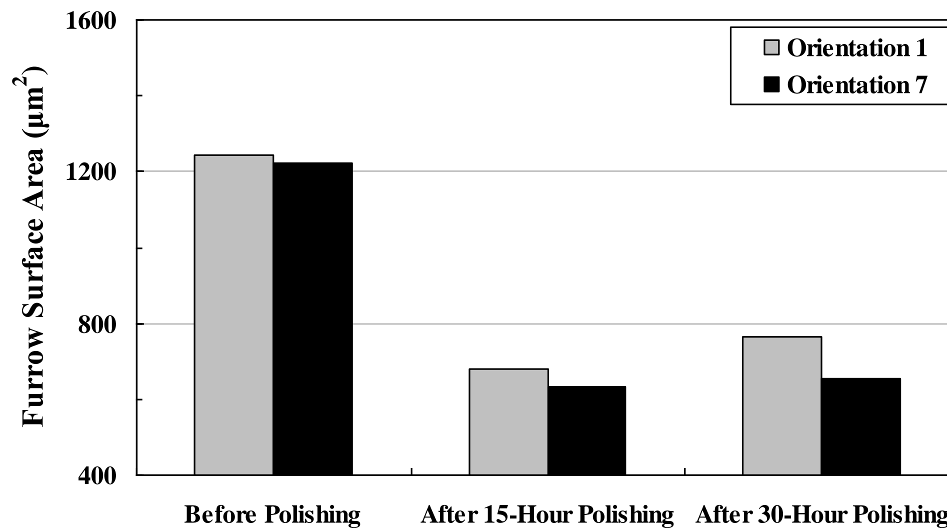

Figure 6.4: Changes in the furrow surface area for the original top 20 aggressive diamonds.

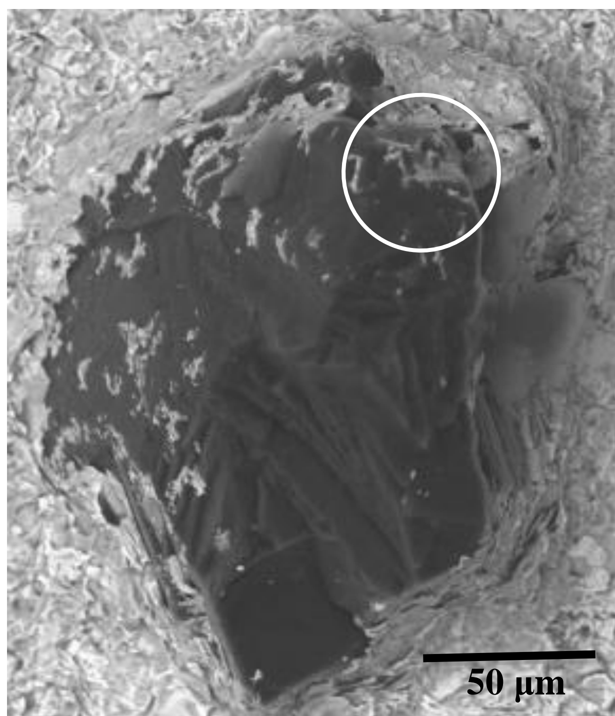

(a)

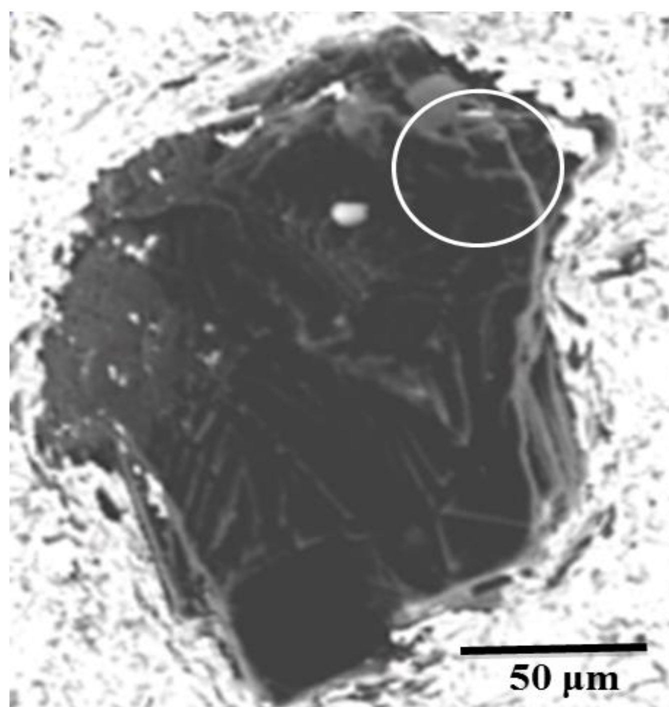

(b)

Figure 6.5: SEM images of an original aggressive diamond (a) before and (b) after 30-hour wafer polishing.

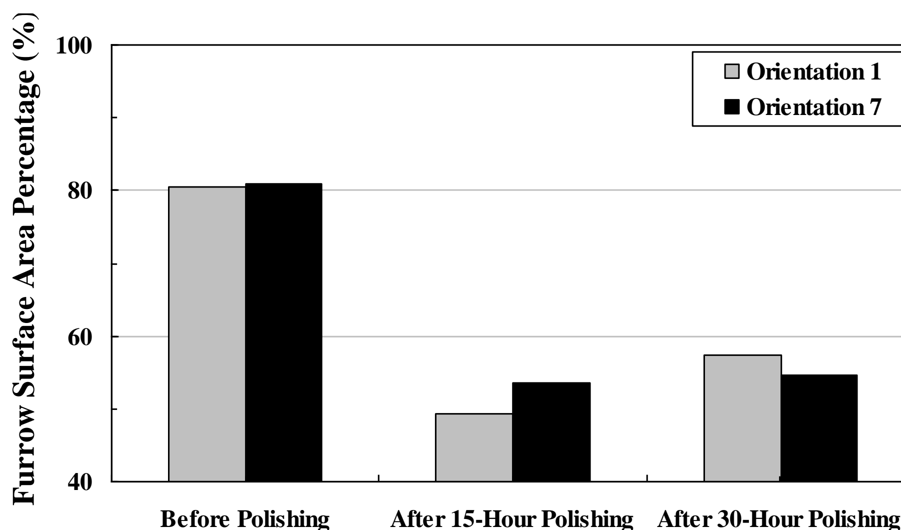

Figure 6.6: Changes in the furrow surface area percentage for the original top 20 aggressive diamonds.

Figure 6.6 summarizes the changes in the furrow surface area percentage for the original top 20 aggressive diamonds identified before wafer polishing during the 30-hour tests. Before polishing, the furrow surface area generated by these aggressive diamonds accounts for 81% of the total furrow surface area generated by all the active diamonds on the disk, confirming that these aggressive diamonds are the dominant working diamonds in pad conditioning. After the first 15-hour polishing, their furrow surface area percentage decreases significantly (from 81% to 49% for Orientation 1 and from 81% to 54% for Orientation 7), indicating that new aggressive diamonds are “born” as the original aggressive diamonds wear out. For both disk orientations, 7 new aggressive diamonds are “born” after the first 15-hour polishing and join the new top 20 aggressive diamond list. Table 6.1 summarizes the rank, furrow surface area and furrow surface area percentage for these 7 new “born” aggressive diamonds. Their furrow surface area accounts for 34% and 26% of the total furrow surface area for Orientation 1 and 7

respectively, indicating that these newly "born" aggressive diamonds make significant contributions to pad conditioning.

Table 6.1: Rank, furrow surface area and percentage for 7 new "born" aggressive diamonds after the first 15-hour polishing test.

Orientation	Rank	Furrow surface area (μm^2)	Furrow surface area percentage (%)
1	1	190	13.8
	4	84	6.1
	6	55	4.0
	7	54	3.9
	11	42	3.1
	17	24	1.7
	18	24	1.7
7	2	73	6.2
	3	68	5.8
	7	49	4.1
	11	33	2.8
	13	32	2.7
	18	24	2.0
	19	24	2.0

Figure 6.7 shows the changes in the furrow surface area for the new top 20 aggressive diamonds identified after the first 15 hours of polishing. The furrow surface area for the new top 20 aggressive diamonds is 1,088 and 899 μm^2 for Orientation 1 and 7, respectively. In comparison, the furrow surface area for the original top 20 aggressive diamonds is 1,242 and 1,223 μm^2 for Orientations 1 and 7, respectively before wafer polishing as shown in Figure 6.4. This indicates that although 7 new aggressive diamonds are "born", the furrow surface area for the new top 20 aggressive diamonds is significantly lower (by 12% for Orientation 1 and 27% for Orientation 7) than the

original top 20 aggressive diamonds. Similar to the original top 20 aggressive diamonds, the furrow surface area for the new top 20 aggressive diamonds identified after the first 15-hour polishing does not change significantly after the second 15-hour polishing, indicating that they experience minimum further wear.

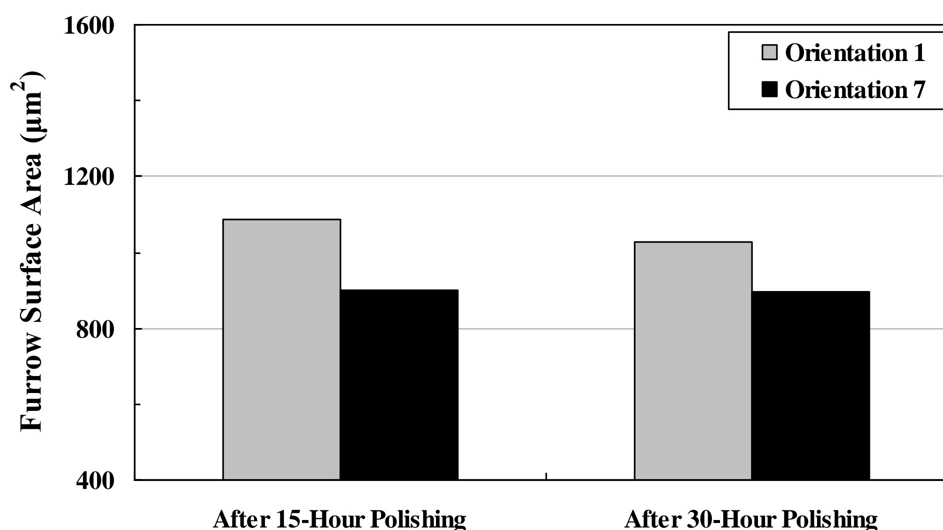

Figure 6.7: Changes in the furrow surface area for the new top 20 aggressive diamonds identified after the first 15-hour wafer polishing.

Figure 6.8 shows the changes in the furrow surface area percentage for the new top 20 aggressive diamonds identified after the first 15 hours of polishing. The furrow surface area percentage for these new top 20 aggressive diamonds accounts for more than 75% of the total furrow surface area for both orientations and does not change significantly after the second 15-hour polishing, indicating that they become, and then, remain as the dominant working diamonds for pad conditioning.

Table 6.2 summarizes the rank, furrow surface area and furrow surface area percentage for the new aggressive diamonds that are “born” after the second 15-hour

polishing. It shows that 5 and 7 new aggressive diamonds are “born” after the second 15-hour polishing and join the new top 20 aggressive diamonds list for Orientations 1 and 7, respectively. As an example, Figure 6.9 shows the SEM image of a newly “born” aggressive diamond. Their furrow surface area percentage (9% and 17% for Orientation 1 and 7, respectively) is significantly lower than the newly “born” aggressive diamonds after the first 15-hour polishing (34% and 26% for Orientations 1 and 7, respectively as shown in Table 6.1). In addition, their ranks are much lower; ranging between 8th and 20th. This indicates that these new “born” aggressive diamonds after the second 15-hour polishing make less contribution to pad conditioning than the 7 new aggressive diamonds that are “born” after the first 15-hour polishing.

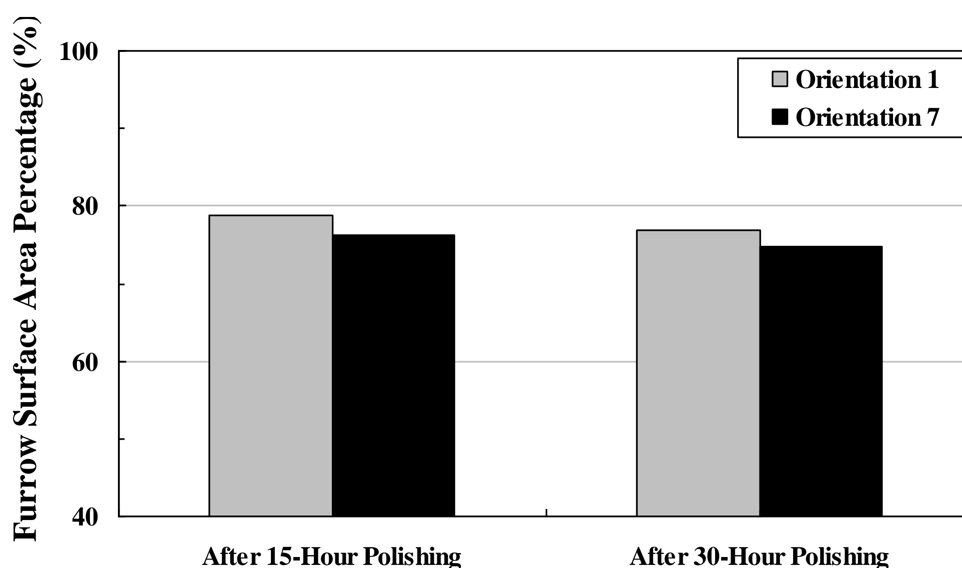

Figure 6.8: Changes in the surface area percentage for the newly identified top 20 aggressive diamonds after the first 15-hour wafer polishing.

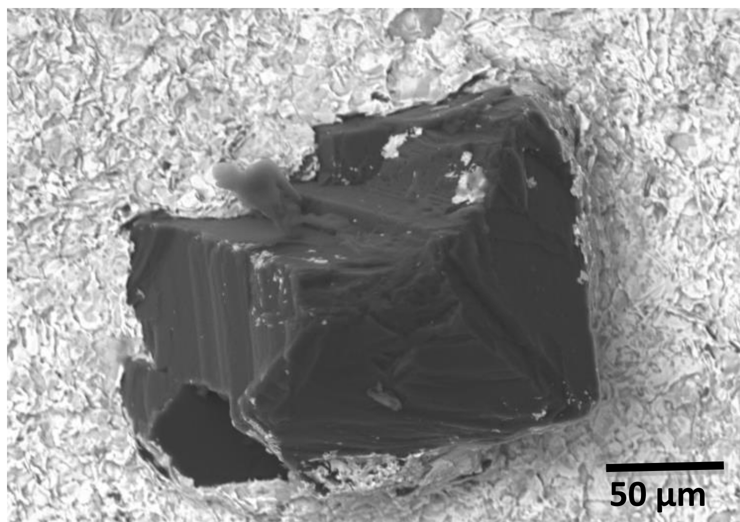

Figure 6.9: SEM image of a new “born” aggressive diamond after 30-hour wafer polishing

.

Table 6.2: Rank, furrow surface area and percentage for the newly "born" aggressive diamonds after the second 15-hour polishing test.

Orientation	Rank	Furrow surface area (μm^2)	Furrow surface area percentage (%)
1	14	33	2.5
	17	26	1.9
	18	24	1.8
	19	22	1.6
	20	21	1.6
7	8	42	3.5
	11	33	2.8
	14	29	2.5
	15	28	2.4
	16	27	2.3
	18	20	1.7
	19	17	1.4

Figure 6.10 shows the changes in the total furrow surface area generated by all the active diamonds during the 30 hours of polishing. For both disk orientations, the total furrow surface area decreases (10% and 22% for Orientations 1 and 7, respectively) after the first 15 hours, indicating that the disk loses its aggressiveness due to the wear of its original aggressive diamonds. The total furrow surface area decreases much less significantly than that of the original top 20 aggressive diamonds (45% for Orientation 1 and 48% percent for Orientation 7) as new aggressive diamonds are "born" and contribute to pad conditioning. The average total furrow surface area for Orientation 1 and 7 remains almost unchanged after the second 15-hour polishing, indicating that the disk maintains its aggressiveness. This trend is consistent with that of the new top 20 aggressive diamonds identified after the first 15-hour polishing (shown in Figure 6.7).

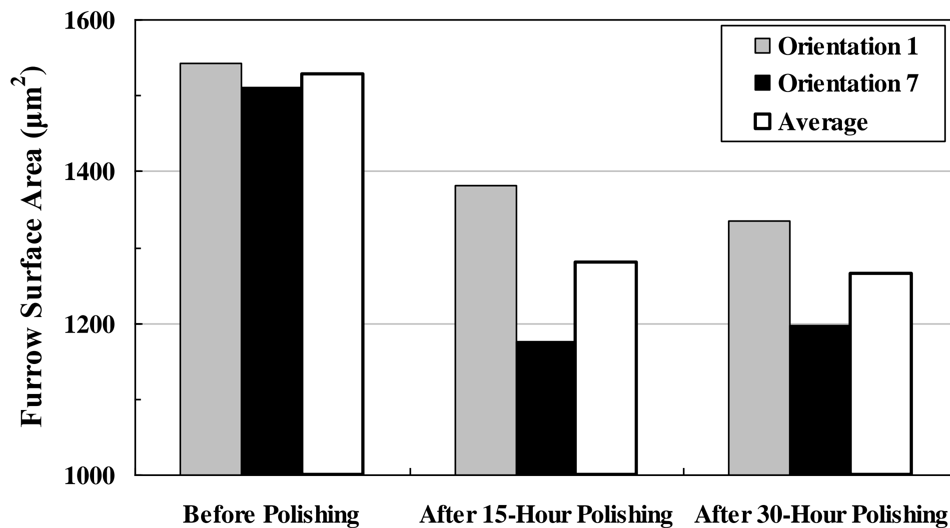

Figure 6.10: Changes in the total furrow subsurface area during 30-hour wafer polishing.

Disk aggressiveness has been shown to affect material removal rates. For example, Sun *et al*. analyzed the effect of disk aggressiveness on pad surface contact using laser confocal microscopy (Sun *et al*. 2010). They found that a more aggressive disk generated a rougher pad surface with fewer contacting summits and less contact area, resulting in a higher interlayer dielectric removal rate. Tsai *et al*. also found that oxide removal rate decreased as the diamond disk gradually became less aggressive during its life (Tsai *et al*. 2011). Therefore, although no material removal rate has been collected in this study, it is expected that the material removal rate decreases after the first 15-hour pad conditioning and then remains relatively stable after 30-hour polishing.

Disk aggressiveness also affects CMP-related defects. Yang *et al*. found that the less aggressive disk with 70 μm nominal diamond size generated significantly lower scratch counts than the more aggressive disk with 180 μm nominal diamond size (Yang *et al*. 2010). Elmufdi *et al*. and Muldowney *et al*. showed that pad surface with higher contact area could reduce CMP-related defects since higher contact area induces lower local pressure to the wafer (Elmufdi *et al*. 2007; Muldowney *et al*. 2007). As Sun *et al*. found that a more aggressive disk creates pad surface with less contact area (Sun *et al*. 2010), the more aggressive diamond disk is expected to generate more defects during CMP processes.

In this study, aggressive diamonds are identified for two perpendicular disk orientations. As such, some of the top 20 aggressive diamonds identified for Orientation 1 are not on the list of the top 20 aggressive diamonds for Orientation 7, and vice versa. Table 6.3 summarizes the number of common aggressive diamonds (diamonds that are on

the top 20 aggressive list for both orientations) during the 30-hour polishing. As these aggressive diamonds are irregular in shape and their cutting points are randomly aligned, the aggressive diamonds for one disk orientation may not necessarily be an aggressive diamond when the disk is rotated 90 degrees. As an example, Figure 6.11 shows the SEM image of an original, top 10, aggressive diamond. This diamond has an irregular shape and its cutting point is aligned with Orientation 1. While it is one of the top 20 aggressive diamonds for Orientation 1, it is not a top 20 aggressive diamond for Orientation 7. Although there are only 5 to 7 common aggressive diamonds for Orientations 1 and 7, the furrow surface area of the top 20 aggressive diamonds and the total furrow surface area of all the active diamonds exhibit the same general trend for these two orientations during the 30-hour polishing tests as shown in Figures 6.4 and 6.10. As the diamond disk rotates during pad conditioning, the active diamonds from different disk orientations all contribute to pad conditioning. On the other hand, the extent of wear on the active diamonds appears different for different disk orientations in this study. As shown in Figure 6.10, the total furrow surface area for disk Orientation 7 decreases more significantly than disk Orientation 1 after 15-hour polishing. This suggests that there is more wear on the active diamonds for disk Orientation 7 after 15-hour polishing.

Table 6.3: Number of common top 20 aggressive diamonds for Orientation 1 and 7.

Dragging test	Number of common diamonds
Before polishing	6
After 15-hour polishing	7
After 30-hour polishing	5

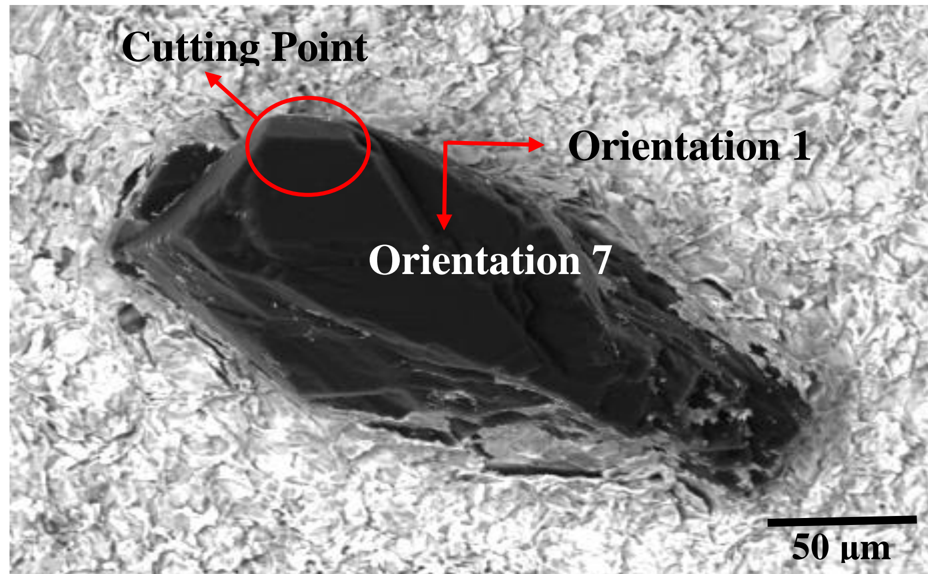

Figure 6.11: SEM image of a typical aggressive diamond.

6.4 Conclusions

In this Chapter, a 3M A3700 diamond disk was used to condition a CMC D100 pad for a total of 30 hours. Its aggressive diamonds and the furrow surface area evolution were analyzed on a pad substitute material (i.e. polycarbonate sheets). Results showed that the top 20 aggressive diamonds identified during the 30-hour polishing tests accounted for more than 75% of the total furrow surface area, confirming that they are the dominant working diamonds in pad conditioning. Results also showed that the original top 20 aggressive diamonds identified before wafer polishing experienced wear after the first 15 hours of polishing, indicated by the significant decrease (47%) in their furrow surface area. Seven new aggressive diamonds were "born" and they made a significant contribution (34% and 26% for Orientation 1 and 7, respectively) to the total furrow surface area. On the other hand, the furrow surface area generated by the new top 20 aggressive diamonds identified after the first 15-hour polishing was significantly

lower (by 20%) than the original top 20 aggressive diamonds, leading to the loss of disk aggressiveness. In comparison, the disk aggressiveness was maintained after the second 15-hour wafer polishing as the furrow surface area of these new top 20 aggressive diamonds did not change significantly. The above results showed a general trend for a conventional diamond disk during its early life: the disk initially loses its aggressiveness due to wear of its original aggressive diamonds; as the original aggressive diamonds wear out, new aggressive diamonds are "born", but these new aggressive diamonds are less aggressive than the original aggressive diamonds; the disk aggressiveness can be maintained if these new aggressive diamonds withstand further wear.

CHAPTER 7

CONCLUSIONS AND FUTURE PLANS

7.1 Conclusions

A series of studies were performed in this dissertation to grasp some of the fundamentals of the CMP processes, and to explore possible solutions to some of CMP's challenges. Major conclusions of each study are presented below.

- *Pad Surface Thermal Management during Copper Chemical Mechanical Planarization* (Chapter 4): This study presented the feasibility of using a novel pad surface thermal management (PTM) system to improve WIWRRNU by locally adjusting the pad surface temperature. The system successfully showed that "center-fast" removal rate profiles can be modulated and improved during copper CMP. At first, a system with a single thermal transfer module was tested. To help reduce local removal rates near the center of the wafer, a cold module was placed on the pad surface with its center corresponding to the center track of the wafer. Chilled water (2 ℃) was introduced to the module via an external chiller. Results showed that local removal rates decreased in both the central region of the wafer as well as the edge. Therefore, the uniformity could not be improved appreciably since edge region periodically contacted the pad surface region with the lower temperature due to wafer rotation during polishing. This resulted in the entire

wafer surface to be cooled and thus the local removal rates decreased across the whole wafer surface. In order to reduce the local removal rates in the wafer center region while maintaining the removal rates in the wafer edge region, two thermal transfer modules were then tested. The cold module, same as before, was placed on the wafer center track and cooled water (2 ℃) was introduced. A hot module aimed to heat the wafer edge region using hot water at 34 ℃ was introduced. Results showed that local removal rates in the wafer center region decreased significantly while maintaining the removal rates in the wafer edge region. Uniformity was improved significantly since the wafer center region contacted the lower temperature region during polishing thus lowering the removal rates locally. On the other hand, as the wafer edge region periodically contacted the pad surface region with the lower and higher temperatures, respectively, the local removal rates in the wafer edge region did not change significantly.

- *Effect of Pad Groove Design on Slurry Injection Scheme during Interlayer Dielectric Chemical Mechanical Planarization* (Chapter 5): In this study, the effect of pad groove design on slurry injection scheme during ILD CMP was investigated. A novel slurry injector was developed, which could provide optional slurry injection schemes (i.e. one injection point scheme and multi-injection point scheme). These injection schemes were tested on an IC1000 concentrically grooved and an IC1000 xy-groove pad. At first, the one

injection point scheme was investigated on both pads. For the concentrically grooved pad, the one injection point scheme generated significantly higher removal rates (ranging from 22 to 35 percent) compared to the standard slurry application method. As such, slurry usage could be reduced by at least a factor of 2. This was due to the fact that the slurry injector could effectively separate the used slurry and the rinse water from the fresh slurry. On the xy-groove pad, the one injection point scheme still resulted in higher removal rates (ranging from 3 to 9 percent), however, its removal rate enhancement was not as high as that of the concentrically grooved pad (ranging from 22 to 35 percent). This was believed to be due to different slurry flow patterns on both pads. On the xy-groove pad, when one injection point scheme was used, a large portion of fresh slurry flowed directly to the grooves without participating in polishing. Therefore, relatively less fresh slurry was retained on the pad land area which contributed to lower oxide removal rate. In order to further improve slurry availability on the xy-groove pad, the multi-injection point scheme was tested. Data showed that the multi-injection point scheme enhanced oxide removal rate further (ranging from 17 to 20 percent) compared to the standard slurry application method. As the multi-injection point scheme could retain more fresh slurry on the pad land area, higher oxide removal rates were achieved.

- *Aggressive Diamond Characterization and Wear Analysis during Chemical Mechanical Planarization* (Chapter 6): In this study, a 3M A3700 diamond disk was used to condition a CMC D100 pad for a total of 30 hours. Its aggressive diamonds and the furrow surface area evolution were analyzed on a pad substitute material (i.e. polycarbonate sheets). Results showed that the top 20 aggressive diamonds identified during the 30-hour polishing tests accounted for more than 75% of the total furrow surface area, confirming that they were the dominant working diamonds in pad conditioning. Results also showed that the original top 20 aggressive diamonds identified before wafer polishing experienced wear after the first 15 hours of polishing, indicated by the significant decrease (47%) in their furrow surface area. In the meantime, seven new aggressive diamonds were "born" and they made a significant contribution (34% and 26% for Orientation 1 and 7, respectively) to the total furrow surface area. On the other hand, the furrow surface area generated by the new top 20 aggressive diamonds identified after the first 15-hour polishing was significantly lower (by 20%) than the original top 20 aggressive diamonds, leading to the loss of disk aggressiveness. In comparison, the disk aggressiveness was maintained after the second 15-hour wafer polishing as the furrow surface area of these new top 20 aggressive diamonds did not change significantly. The above results showed a general trend for a conventional diamond disk during its early life as follows: the disk initially loses its aggressiveness due to wear of its original aggressive diamonds; as the original

aggressive diamonds wear out, new aggressive diamonds are "born", but these new aggressive diamonds seem to be less aggressive than the original ones; the disk aggressiveness can be maintained if these new aggressive diamonds withstand further wear.

7.2 Future Plans

Given the variety of work conducted in this dissertation, several future studies are proposed.

- *Pad Surface Thermal Management during Copper Chemical Mechanical Planarization* (Chapter 4): This study presented the feasibility of using a novel pad surface thermal management (PTM) system to improve WIWRRNU by locally adjusting the pad surface temperature. Results showed that, when two thermal transfer modules were employed, local removal rates in the wafer center region decreased significantly while maintaining the removal rates near the wafer edge thereby significantly improving WIWRRNU. However, in order to attain acceptable WIWRRNUs for high volume manufacturing applications, considerable optimization (e.g. the size, number, location, and temperature of thermal transfer modules) is needed. In addition, it is worthwhile to build a mathematical model to simulate the effect of the PTM system on WIWRRNUs, which can be used to guide the optimization of the PTM system for adjusting a particular copper removal rate

profile. Furthermore, the change in pad surface temperature may affect surface defects. It is necessary to check surface defects with temperature as a topic for future study.

- *Effect of Pad Groove Design on Slurry Injection Scheme during Interlayer Dielectric Chemical Mechanical Planarization* (Chapter 5): In this study, the effect of pad groove design on slurry injection scheme during ILD CMP was investigated. Different slurry injection schemes were compared, in terms of material removal rate, on a concentrically grooved pad and an xy-groove pad, respectively. Besides material removal rate, it is worthwhile to compare these injection schemes in terms of other performance parameters (e.g. WIWRRNU and wafer surface defects). Also, in the future, we should investigate the effect of pad groove design on slurry injection scheme during Cu, W, and STI CMP. In addition, it will be beneficial to investigate the effect of polishing pressure, pad/wafer rotational speed, slurry concentration and temperature on the slurry injector's polishing performance for pads with different groove designs in the future.

- *Aggressive Diamond Characterization and Wear Analysis during Chemical Mechanical Planarization* (Chapter 6): In this study, a 3M A3700 diamond disk was used to condition a CMC D100 pad for a total of 30 hours. The top 20 aggressive diamonds for two perpendicular disk orientations were identified before the polishing, as well as after 15-hour and 30-hour polishing.

The furrow surface area generated by these top 20 aggressive diamonds and its evolution were analyzed and compared. Results showed a general trend for a conventional diamond disk during its early life. In the future, conditioning marathon tests can be performed to investigate the trend for a conventional diamond disk during its whole life which can be more than 100 hours. Also, it is believed that the disk aggressiveness affects material removal rates and defects. In the future, we should collect removal rate and defect data in the conditioning marathon tests, and correlate these data with the disk aggressiveness.

REFERENCES

1. Aksu, S., L. Wang, and F. Doyle, *J. Electrochem. Soc.*, **150**, G718 (2003).
2. Amontons, G., De la résistance causée dans les machine, Mémories de l' Académie Royale, A, 257-282 (1699).
3. Banerjee, G. and R. Robert, *ECS Trans.*, **13**, 1 (2008).
4. Barthel, H, M. Heinemann, M. Stintz, and B. Wessely, *Chem. Eng. Tech.*, **21**, 745 (1998).
5. Becker, R., W. Tittes, A. Boenicke, S. Peters, M. Probst, D. Schulze, S. Cwikla, and S. Loesch, *2007 International Conference on Planarization/CMP Technology Proceeding*, Dresden VDE VERLAG GMBH, Berlin-Offenbach, October (2007).
6. Borucki, L., J. Sorooshian, Z. Li, A. Philipossian, D. Stein, D. Hetherington, and R. Timon, *Proceedings of the 9th Int. Symp. on Chemical-Mechanical Planarization*, Lake Placid, NY, August 2004.
7. Borucki, L., J. Sorooshian, Z. Li, Y. Sampurno, Y. Zhuang, and A. Philipossian, *Proceedings of the 10th CMP-MIC Conference*, Fremont, CA, February 2005.
8. Borucki, L., R. Zhuang, Y. Zhuang, A. Philipossian, and N. Rikita, *Mater. Res. Soc. Symp. Proc.*, **991**, C01.01 (2007).
9. Borucki, L., Y. Zhuang, R. Kikuma, N. Rikita, T. Yamashita, K. Nagawa, H. Lee, T. Sun, D. Rosales-Yeomans, A. Philipossian, and T. Stout, *Trans. Electr. Electron.Mater.*, **8**, 15 (2007).
10. Borucki, L. and N. Rikita, U. S. Pat. 7,410,411 (2008).

11. Borucki, L., Y. Sampurno, and A. Philipossian, U.S. Pat. 2011/61503517.

12. Borucki, L., A. Philipossian, Y. Sampurno, and S. Theng, U. S. Pat. 2012/8197306.

13. Borucki, L., Y. Zhuang, Y. Sampurno, A. Philipossian, and S. Kreutzer-Schneeweiss, *2012 International Conference on Planarization/CMP Technology Proceeding*, p. 35 (2012).

14. Borucki, L., Y. Zhuang, Y. Sampurno, A. Philipossian, and S. Kreutzer-Schneeweiss, *ECS Trans.*, **52**, 591 (2013).

15. Caprio, R., J. Farkas, R. Jairath, *Thin Solid Film*, **266**, 238 (1995).

16. Chamberlin, T., M. Miller, and E. Walton, U. S. Pat. 1999/5997392.

17. Chang, S., K. Tsao, M. Meneshian, and H. Waggener, *Proceedings of the Third International Symposium on Very Large Scale Integration Science and Technology*, 1985.

18. Chang, W., U. S. Pat. 2005/6929533.

19. Charns, L., M. S. Thesis, University of Arizona, Tucson, AZ (2003).

20. Chen, H., U.S. Pat. 2004/6764387.

21. Chen, K., H. Yeh, J. Yan, and Y. Chen, *Int. J. Adv*. Manuf. Technol., **42**, 1118 (2008).

22. Choi, J. and C. Korach, *J. Electrochem. Soc.*, **156**, H961 (2009).

23. Cook, L. M., *J. Non-Cryst. Solids*, **120**, 152 (1990).

24. Coulomb, C. A., *Mém. Math. Phys.*, **10**, 161 (1785).

25. DeNardis, D., Ph.D. Thesis, University of Arizona, Tucson, AZ (2006).

26. DeNardis, D., Y. Seike, M. Takaoka, K. Miyachi, and A. Philipossian, *Wear*, **260**, 1224 (2006).

27. Doering, R. and Y. Nishi, “Handbook of Semiconductor Manufacturing”, Marcel Dekker, 2000.

28. Elmufdi, C. L. and G. P. Muldowney, *Mater. Res. Soc. Symp. Proc.*, **991,** C01.02 (2007).

29. Fan, W., D. Boning, L. Charns, H. Miyauchi, H. Tano, and S. Tsuji, *J. Electrochem. Soc*., **157**, H526 (2010).

30. Fan, W., Ph. D. Thesis, Massachusetts Institute of Technology, Cambridge, MA (2012).

31. Fu, G. and A. Chandra, *J. Electron. Mater.*, **30**, 401 (2001).

32. Gupta, S., *Microelectron. Manuf. Test.*, **12**, 1(1989).

33. Guthrie, W., I. Ocanada, and N. Schendon, U. S. Pat. 1998/5709593.

34. Hegde, S. and S. Babu, *Solid-State Lett.*, **6**, G216 (2003).

35. Hennessy, J. and D. Patterson, “Computer Architecture: A Quantitative Approach”, Morgan Kaufmann, San Francisco, CA (2007).

36. Hernandez, J., P. Wrschka, and G. Oehrlein, *J. Electrochem. Soc*., **148**, G389 (2001).

37. Hocheng, H. and Y. Huang, *Int.J. Mater. Prod. Tec.*, **18**, 469 (2003).

38. Holland, L., “The Properties of Glass Surface”, Chapman & Hall, London (1964).

39. Holland, K., A. Hurst, and H. Pinder, *Micro,* **20**, 26 (2002).

40. Holloway, P. and McGurie G., “Handbook of Compound Semiconductors: Growth, Processing, Characterization, and Devices”, Noyes Publications, 1996.

41. http://aracainc.com/media/pubs/Polisher_and_Tribometer_300mm.pdf; last accessed April 28, 2015.

42. http://www.aracainc.com/products/apd-polishers.

43. http://www.itrs.net/.

44. http://www.kinik.com.tw/kinik/products/cmp_en.asp.

45. http://www.tribology-abc.com/abc/history.htm.

46. Jiao, Y., Y. Sampurno, Y. Zhuang, X. Wei, A. Meled, and A. Philipossian, *Jpn. J. Appl. Phys*., **50**, 05EC02-1 (2011).

47. Jiao, Y., Ph.D. Thesis, University of Arizona, Tucson, AZ (2012).

48. Jiao, Y., X. Liao, C. Wu, S. Theng, Y. Zhuang, Y. Sampurno, M. Goldstein, and A. Philipossian, *J. Electrochem. Soc.*, **159**, H255 (2012).

49. Jiao, Y., Y. Zhuang, X. Wei, Y. Sampurno, A. Meled, S. Theng, J. Cheng, D. Hooper, M. Moinpour, and A. Philipossian, *ECS J. Solid State Sci. Technol.*, **1**, N103 (2012).

50. Kajiwara, J., G. Moloney, D. Hansen, and A. Reyes, U.S. Pat. 2003/6506105.

51. Kajiwara, J., G. Moloney, H. Wang, D. Hansen, and A. Reyes, U.S. Pat. 2003/6623343.

52. Kang, S. and Y. Leblebici, “CMOS Digital Integrated Circuits Analysis & Design: Analysis and Design”, McGraw-Hill Professional, 2002.

53. Kaufman, F., D. Thompson, R. Broadie, M. Jaso, W. Guthrie, D. Pearson, and M. Small, *J. Electrochem. Soc.*, **138**, 3460 (1991).

54. Krishnaswamy, V., L. Shin, and S. Turullols, *9th IEEE Asian Solid-State Circuits Conference Proceedings of Technical Papers*, p.17 (2013).

55. Lawing, A., *Proc. 7th Int. Chemical-Mechanical Planarization for ULSI Multilevel Interconnection Conference (CMP-MIC)*, p. 1 (2002).

56. Lee, H., B. Park, and H. Jeong, *Microelectron. Eng.*, **85**, 692 (2008).

57. Lee, H., B. Park, and H. Jeong, *J. Mater. Process. Technol.*, **209**, 1732 (2009).

58. Lee, H., Y. Zhuang, L.Borucki, S. Joh, F. O Moore, and A. Philipossian, *Thin Solid Films*, **519**, 262 (2010).

59. Lee, H., Y. Zhuang, M. Sugiyama, Y. Seike, M. Takaoka, K. Miyachi, T. Nishiguchi, H. Kojima, and A. Philipossian, *Thin Solid Films*, **518**, 1994 (2010).

60. Levert, J. and D. Towery, U.S. Pat. 018723 (2001).

61. Li, Y., "Microelectronics Applications of Chemical Mechanical Planarization", John Wiley & Sons, New Jersey (2008).

62. Li, Z., Ph.D. Thesis, University of Arizona, Tucson, AZ (2005).

63. Li, Z., L. Borucki, I. Koshiyama, and A. Philipossian, *J. Electrochem. Soc.*, **151**, G482 (2005).

64. Liang, H., F. Kaufman, R. Sevilla, and S. Anjur, *Wear*, **211**, 271 (1997).

65. Liang, H. and G. Xu, *Scripta Materialia*, **46**, 343 (2002).

66. Liang, H. and D. Craven, "Tribology in Chemical-Mechanical Planarization", Taylor & Francis, Boca Raton, FL (2005).

67. Liao, X., Y. Zhuang, L. Borucki, S. Theng, X. Wei, T. Ashizawa, and A. Philipossian, *Electrochem. Solid-State Lett.*, **14**, H201 (2011).

68. Liao, X., Y. Sampurno, Y. Zhuang, and A. Philipossian, *Electrochem. Solid-State Lett.*, **15**, H118 (2012).

69. Liao, X., Y. Zhuang, L. Borucki, J. Cheng, S. Theng, T. Ashizawa, and A. Philipossian, *Jpn. J. Appl. Phys.*, **52**, 018001 (2013).

70. Liao, X., Ph.D. Thesis, University of Arizona, Tucson, AZ (2014).

71. Liao, X., Y. Zhuang, L. Borucki, J. Cheng, S. Theng, T. Ashizawa, and A. Philipossian, *Jpn. J. Appl. Phys.*, **53**, 086501 (2014).

72. Liao, Y., *2008 International Conference on Planarization/CMP Technology proceeding*, p. 11 (2008).

73. Lu, F., W. Chien, C. Chang, and Y. Lo, U. S. Pat. 2006/7052374.

74. Lu, J., J. Coppeta, C. Rogers, V. Manno, L. Racz, and A. Philipossian, *Mater. Res.Soc. Symp. Proc.*, **613**, E1.2.1 (2000).

75. Lu, J., J. Garland, C. Petti, S. Babu, and R. Roy, *J. Electrochem. Soc.*, **151**, G717 (2004).

76. Mau, C., Master of Science Thesis, Massachusetts Institue of Technology, Cambridge, MA (2008).

77. Matsumura, Y., T. Hirao, and M. Kinoshita, *Jpn. J. Appl. Phys.*, **47**, 2083 (2008).

78. May, G. and S. Simon, "Fundamentals of Semiconductor Fabrication", Wiley, 2004.

79. McGurie, G., "Semiconductor Materials and Processing Technology Hand Book", William Andrew Publishing, 1988.

80. Meled, A., Y. Sampurno, Y. Zhuang, and A. Philipossian, *Electrochem. Solid-State Lett.*, **13**, H52 (2010).

81. Meled, A., Y. Zhuang, X. Wei, J. Cheng, Y. A. Sampurno, L. Borucki, M. Moinpour, D. Hooper, and A. Philipossian, *J. Electrochem. Soc.,* **157**, H250 (2010).
82. Meled, A., Ph. D. Thesis, University of Arizona, Tucson, AZ (2011).
83. Meled, A., Y. Zhuang, Y. Sampurno, S. Theng, Y. Jiao, L. Borucki, and A.Philipossian, *Jpn. J. Appl. Phys.,* **50**, 05EC01-1 (2011).
84. Moore, E. G., *Electronics*, **38**, April 1965.
85. Moy, D., M. Schadt, C. Hu, F. Kaufman, A. Ray, N. Mazzeo, E. Baran, and D. Pearson, *Proceedings 1989 VMIC Conference*, 26, 1989.
86. Muldowney, G. P., *Mater. Res. Soc. Symp. Proc.*, **816**, K5.3.1 (2004).
87. Muldowney, G. P., C. H. Duong, M. R. VanHanehem, and C. C. Kuo, *Proceedings of ISTC Conference,* p.225 (2007).
88. Nguyen, V., H. Kranenburg and P. Woerlee, *Proceedings of Third International Workshop on Materials Science*, Hanoim, 1999.
89. Oliver, M., "Chemical Mechanical Planarization of Semiconductor Materials", Springer-Verlag, Germany (2004).
90. Park, K. and H. Jeong, *J. Electrochem. Soc.*, **155**, H595 (2008).
91. Paik, U. and J. Park, "Nanoparticle Engineering for Chemical-Mechanical Planarization", p. 16, CRC Press, Florida (2009).
92. Philipossian, A. and E. Mitchell, *Jpn. J. Appl. Phys.*, **42**, 7259 (2003).
93. Philipossian, A. and S. Olsen, *Jpn. J. Appl. Phys.,***42**, 6372 (2003).
94. Philipossian, A., L. Borucki, Y. Sampurno, and Y. Zhuang, *Solid State Phenom.*, **219**, 143 (2014).

95. Plummer, J., M. Deal, and P. Griffin, “Silicon VLSI Technology: Fundamentals, Practice and Modeling”, Prentice Hall, Upper Saddle River, NJ (2000).

96. Preston, F., *J. Soc. Glass Technol.*, **11**, 247 (1927).

97. Renteln, P. and T. Ninh, *Mater. Res. Soc. Symp. Proc.*, **566**, 155 (1999).

98. Rogers, C., J. Coppeta, and L. Racz, *J. Electron. Mater.,* **27**, 1082 (1998).

99. Sampurno, Y., L. Borucki, Y. Zhuang, D. Boning, and A. Philipossian, *J. Electrochem. Soc*., **152**, G537 (2005).

100. Sampurno, Y., Ph. D. Thesis, University of Arizona, Tucson, AZ (2008).

101. Sampurno, Y., A. Rice, Y. Sampurno, and A. Philipossian, *Electrochem. Solid-State Lett.*, **14**, H318-H321 (2011).

102. Shen, J., W. Costas and M. Cook, *J. Eletrochem. Soc.*, **145**, 4240 (1998).

103. Shendon, N., U. S. Pat. 2000/6019671.

104. Shockley, W., *IEEE Trans. Elec. Dev.,* **ED-31**, 1523 (1984).

105. Sivaram, S., H. Bath, R. Legget, A. Maury, K. M onning, and R. Tolles, *Solid State Technol.*, 87 (1992).

106. Sorooshian, J., D. Denardis, L. Charns, Z. Li, D. Boning, F. Shadman, and A. Philipossian, in *proceedings of 2003 CMP-MIC*, P.43-50 (2003).

107. Sorooshian, J., D. Denardis, L. Charns, Z. Li, F. Shadman, D. Boning, D. Hetherington, and A. Philipossian, *J. Electrochem. Soc.*, **151**, G85 (2004).

108. Sorooshian, J., L. Borucki, D. Stein, R. Timon, D. Hetherington, and A. Philipossian, *J. Tribol.*, **127**, 639 (2005).

109. Stavreva, Z., D. Zeidler, M. Plotner, and K. Drescher, *Appl. Surf. Sci*., **91**, 194 (1995).

110. Steigerwald, J., S. Murarka, and R. Gutmann, “Chemical Mechanical Planarization of Microelectronic Materials”, Wiley, NY (1997).

111. Stober, W. and A. Fink, *J. Coll. Interf. Sci.*, **26**, 62 (1968).

112. Stolarski, T. A., “Basic Principles in Tribology, in Tribology in Machine Design”, Industrial Press, Oxfoxd (1990).

113. Sun, T., Ph. D. Thesis, University of Arizona, Tucson, AZ (2009).

114. Sun, T. , L. Borucki, Y. Zhuang, Y. Sampurno, F. Sudargho, X. Wei, S. Anjur, and A. Philipossian, *Jpn. J. Appl. Phys.*, **49,** 026501 (2010).

115. Sun, T., Y. Zhuang, L.Borucki, and A. Philipossian, *Jpn. J. Appl. Phys.*, **49**, 046501-1 (2010).

116. Sun, T., Y. Zhuang, L.Borucki, and A. Philipossian, *Jpn. J. Appl. Phys*., **49**, 066501-1 (2010).

117. Thakurta, D., D. Schwendeman, R. Gutmann, S. Shankar, L. Jiang, and W. Gill, *Thin Solid Film*, **414**, 78 (2002).

118. Tomozawa, M., *Solid State Technol.*, **40**, 169 (1997).

119. Tsai, M. and J. Peng, *Mater. Manuf. Processes*, **25**, 1440 (2010).

120. Tsai, M. and W. Chen, *Int. J. Adv. Manuf. Technol.*, **55**, 253 (2011).

121. Tseng, W. and Y. Wang, *J. Electrochem. Soc.*, **144**, L15 (1997).

122. Tseng, W., E. Rill, B. Backes, M. Chace, Y. Yao, P. DeHaven, A. Ticknor, V. Devarapalli, M. Khojasteh, D. Steber, L. Economikos, C. Truong, and C. Majors, *ECS J. Solid State Sci. Technol.*, **3**, N3023 (2014).

123. Wang, T. and X. Lu, *Microeletron. Eng.*, **88**, 3329 (2011).

124. Wang, Y., Ph. D. Thesis, National Cheng Kung University, Tainan, Taiwan (2008).

125. Wei, X.: Ph.D. Thesis, University of Arizona, Tucson, AZ (2010).

126. Wolf, S., "Silicon Processing for the VLSI Era – Volume 4: Deep-Submicron Process Technology", Lattice Press, Sunset Beach, CA (2002).

127. Wolf, S., "Microchip Manufacturing", Lattice Press, Sunset Beach, CA (2004).

128. Wolters, P. Available at http://www.peterwolters.com/cmp/cmpmultilevle.htm; 2003.

129. Wu, C., Y. Zhuang, X. Liao, Y. Jiao, Y. Sampurno, S. Theng, F. Sun, A. Naman, and A. Philipossian, *ECS J. Solid State Sci. Technol.*, **2**, P36 (2013).

130. Wu, C., Y. Sampurno, X. Liao, Y. Jiao, S. Theng, Y. Zhuang, L. Borucki, and A. Philipossian, *ECS J. Solid State Sci. Technol.*, **4**, P206 (2015).

131. Wu, C., Y. Sampurno, X. Liao, Y. Zhuang, L. Borucki, S. Theng, and A. Philipossian, submitted to *ECS J. Solid State Sci. Technol.*, Manuscript Number JSS-15-0492R (2015).

132. Yang, J., J. Choi, T. Hwang, C. Lee, and T. Kim, *Int. J. Mach. Tool. Manu.*, **50,** 865 (2010).

133. Yoshida, M., H. Ono, M. Nishiyama, T. Ashizawa, and T. Doi, *Jpn. J. Appl. Phys.*, **45**, 733 (2006).

134. Yu, X. and P. Somasundaran, *P. Colloids. Surf. A.*, **89**, 277 (1994).

135. Zantye, P., A. Kumar, and A. Sikder, *Mater. Sci. Eng., R.,* **45**, 89 (2004).

136. Zhang, F. and A. Busnaina, *Electrochem. Solid-State Lett.*, **1**, 184 (1998).

137. Zhuang, Y., Y. Sampurno, C. Wu, B. Wu, Y. Mu, L. Borucki, A. Philipossian, and R. Yang, *ECS Trans.*, **60**, 625 (2014).